The Experimental Study of Micro-Surface Structures Effect on 2D and 3D Model at Low Reynolds Number

A thesis submitted to The University of Manchester for the degree of
MPhil of Aerospace Engineering
2019

Hanni Defianti

ID: 9250386

Project Supervisor: Professor Shan Zhong

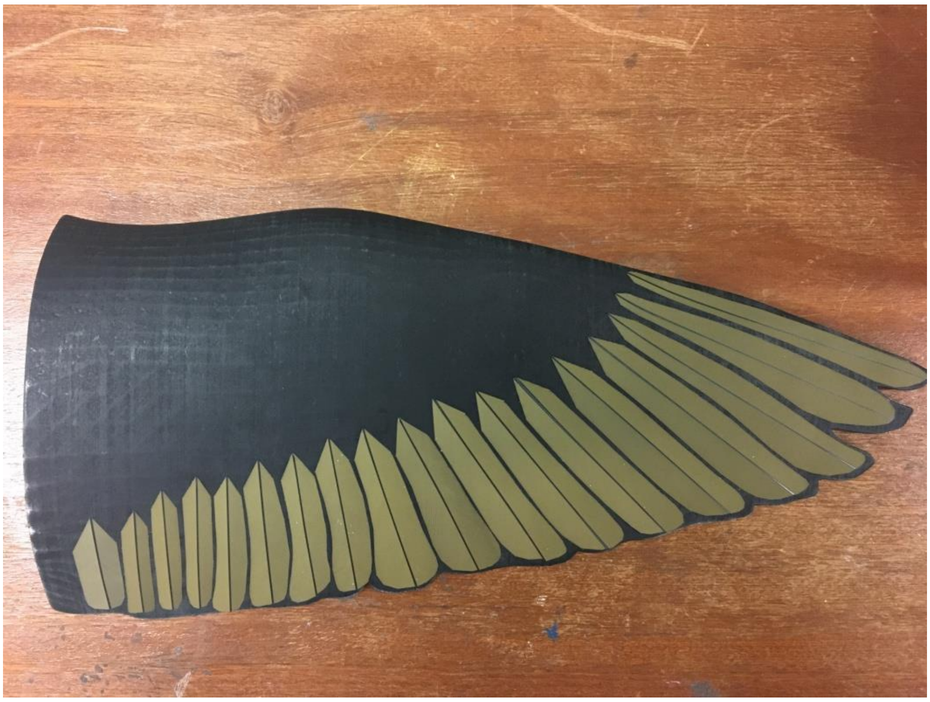

School of Mechanical, Aerospace and Civil Engineering

Contents

Word Count – 21,026

List of Figure

List of Table

Nomenclature

D – Total drag [N]

Df – Friction drag [N]

Ds – Pressure drag [N]

CD – Total drag coefficient []

Cf – Friction drag coefficient []

Cs – Pressure drag coefficient []

s – Riblet spacing [mm]

h – Riblet height [mm]

t – Riblet thickness [mm]

s^+ - Dimensionless riblet spacing []

h+ - Dimensionless riblet height []

t^+ - Dimensionless riblet thickness []

V_τ – Wall shear stress velocity [m/s]

F_d – Drag force [N]

A_w – Wetted area [m^2]

ν – Kinematic viscosity [m^2/s]

ρ – Density [kg/m^3]

α – Angle of sawtooth riblet [^{o}, degree]

θ – Yaw angle between the riblets [^{o}, degree]

Abstract

Nature inspires researchers to explore the surroundings with the aim to come up with novel ideas. Consequently, the passive drag reduction technique of introducing the riblets to the surface of the object in a fluid flow was also bio-inspired. Shark-skin infused longitudinal riblets effects on a fluid flow have been widely investigated since the discovery was made in 1970s. Even though the desired drag reducing performance was captured, due to complications in implementing the technology in real-world applications other options had to be investigated further. Inspired by graceful bird's flight, researchers found an alternative. Vaguely examined herringbone-type riblets covering the surface of a bird feather might be carrying a huge potential as a way of improving the flow performance over the objects in a fluid flow. By examining the convergent/divergent riblet foils fitted on a bio-inspired pigeon wing model in a wind tunnel, several observations were made. At Reynolds number below 100000 the riblets work as a fluctuations dampening mechanism especially shown at 2D aerofoil model. Furthermore, the increased lift coefficient and reduced drag coefficient was captured at almost all incidence angle for 3D wing model. It was observed that riblets tend to influence the inner structure of the near wake of 2D aerofoil model.

The observations made during the experiment notify about the positive effect on a flow introduced by the riblets, and the lessons learned should be a good background for further research within the field.

Declaration

I, Hanni Defianti, declare that the work presented in this report is all my original work. None of the work referred to in the thesis has been submitted in support of an application for another degree or qualification of this or any other university or other institutes of learning.

Acknowledgments

I would like to thank my individual project supervisor, Professor Shan Zhong, for providing help and guidance throughout this project. I would also like to thank Qiang Liu for all the support he provided me during the experimental phase of the project. Also, thanks to Dr Andrew Kennaugh for introducing me to wind tunnel equipment and testing procedure and David Golding, Mark, Brian also Natalie for the help to prepare for the experiment.

1 Introduction

1.1 Motivation

Even though the alternative green energy is being incorporated into commonness more extensively every year, it cannot solve the energy crisis or pollution problems just yet. Fossil fuels consumption is still increasing with economic growth leading to ever dilating environmental contamination as well as to exhausting the remaining extents of energy resources. However, at least to some degree, these issues can be tackled by minimizing the drag force acting on a surface of moving object in a fluid such as an aircraft or wind turbine blade. It was estimated that skin friction drag on civil aircraft under typical cruise conditions accounts for around 45 per cent of all the drag meaning that even a small reduction would lead to huge energy savings in terms of fuel consumption and hence the reduction in CO_2 emissions (Cousteix, 1992). There are two main methods of reducing skin friction drag: 1) delaying transition point on a surface to extend the laminar flow region around an object hence obtaining lower skin friction coefficient, C_f; 2) modifying turbulent structures within the boundary layer to achieve the reduction in skin friction coefficient, C_f. Passive techniques for turbulent drag reduction involve Large eddy break up devices (LEBU) and a presence of riblets (Viswanath, 2002).

Over the millions of years, living nature around the globe developed the skills and anatomy essential to survive in the ever-changing environment. Consequently, researchers try to investigate the Earth’s flora and fauna with the purpose of understanding its ability to adapt, and then to employ these principles in developing innovations. Drag reduction techniques is a good reflection of this type of process. Longitudinal riblets ability to reduce the drag, so-called shark skin effect, was disclosed for the first time around 40 years ago. Since then the phenomena was extensively investigated by a multitude of researchers. Walsh (1983) concluded that shark-skin inspired longitudinal riblets can reduce drag to 8 per cent compared to the smooth surface with riblets spacing $s^+ = 15$ and height $h^+ = 10$ (the nomenclature explained in Theory section of the report). Choi et al. (1997) examined the near-wall flow over smooth and riblets wall surfaces. They determined that this micro-structures have different turbulent transfers mechanism of heat over the riblet surface than from momentum. Bechert et al. (1997) built and tested the adjustable surface replica of the shark skin using blade type riblets and achieved a maximum skin-friction drag reduction of 9.9 per cent. Finally, the innovation was implemented in real life applications when Airbus and Boeing covered around 70% of aircraft with the plastic film with riblets and managed to capture 3 per cent savings in fuel cost (Dean and Bhushan, 2010). However, certain limitations like a vast amount of waste and complicated applicability restricted longitudinal riblets potential and other options had to be considered.

Consequently, the unhampered flight of the bird was started being investigated to understand the secret behind its ability to move in the air with such ease and gracefulness. Tucker and Parrot (1970) found that in free gliding regime Harris' hawk's tip feathers enable it to fly with only around 80 per cent of the drag that is exerted after clipping its tip feathers emphasizing the important role of streamlining. Nachtigall (1998) created a smooth surface starling model and after testing it in wind tunnel found a 14 per cent drag increase compared to the feather-covered body. Finally, the morphology of the bird feather was investigated for the first time by Chen et al. (2013) as they examined bird feather inspired herringbone-type riblets' ability to reduce the drag. The unique microstructure had shown promising results – the plane-3D herringbone riblets in water tunnel experiment managed to reduce the drag up to 17 per cent compared to the smooth surface. Furthermore, the spatial-3D herringbone riblets improved the remarkable achievement even further by reducing the drag up to 21 per cent. This result exceeds Bechert et al. (1997) achievement (9.9 per cent) more than twice, thus emphasizing the huge potential of herringbone- type riblets which was barely further investigated since Chen et al. (2013) and left an interesting and innovative field that shall be exploited by other researchers.

1.2 Aim and Objectives

The purpose of this work is to understand the flow characteristics around the smooth surface wing first following by the examination of nature-inspired riblets and testing if the herringbone-type riblets can improve the flow around the wing, i.e. reduce the profile drag.

1.3 Report Outline

The theory behind the turbulent flow reduction techniques employing micro-scale surface structures is explained in section 2. Section 3 outlines the existing background research on the topic. Section 4 explains the preparatory process for the experiment. Sections 5 and 6 describe the experimental apparatus and the procedure, respectively. The experimental results and following discussion are based in section 7. The conclusive remarks and suggestions for further work are displayed in section 8 and 9, respectively.

2 Literature Review

2.1 Profile Drag

All the drag around any conventional aerofoil can be divided into three main components - profile, induced and wave drag, as illustrated in the diagram shown in Figure 1. Induced drag can be explained by the creation of vortices from the wing tips so that this is a 3d flow and wave drag due to the generation of shock waves when travelling at supersonic speeds. However, in this report, we are only concerned about the aerofoil profile drag. It consists of two components: friction drag, D_f, due to tangential forces generated by surface shear stresses and pressure (or form) drag, Dp, due to normal forces caused by static pressure.

It can be written as:

$$D = D_f + D_p = D_f\left(1 + \frac{D_p}{D_f}\right)$$

Equation 1

Or in coefficient form:

$$C_D = C_f\left(1 + \frac{C_{dp}}{C_f}\right)$$

Equation 2

Pressure drag is related to flow separation whereas friction drag is concerned with attached flows (Schlichting, 1975).

2.1.1 Skin Friction Drag

Skin friction drag is caused due to the viscosity of the fluid within the boundary layer resulting in a friction on the surface of the object moving in this fluid. It is directly proportional to the surface area and square of the velocity. As the fluid molecules travel by the surface within the boundary layer, they slow down due to limping to the surface and then grasps to further from the surface flowing molecules thus creating a retarding force. This cumulative process is called skin friction drag.

2.1.2 Pressure Drag

Pressure drag is caused by the eddying motion set up behind the object in a form of a wake while moving within the fluid. The fluid is pushing the object harder at the front compared to the back and, hence, the difference between pressures is called a pressure force pushing the object into the backwards direction. Again pressure drag like the friction drag is directly proportional to the square velocity of the object relative to the fluid, but it is related to the cross-sectional area rather than surface area.

2.1.3 Induced Drag

Induced drag is a component of drag that exists for three-dimensional wings. The air pressure on the top of a lifting wing is lower than the air pressure below the wing. The air near the tips of the wing is free to pass from a high-pressure zone to a low-pressure zone. A pair of counter-rotating vortices form at the wing tips as the wing shifts to the lower outward. The wing tip vortices generate a swirling flow of air behind the wing that is strongest near the wing tips and weakens as it approaches the wing base. The induced flow of the vortices reduces the effective angle of attack of the wing, which differs from wing tip to wing base. The induced flow generates a downstream-facing portion of the wing's aerodynamic power. Since it faces downstream and was "induced" by the motion of the tip vortices, this additional force is known as induced drag. Since it only happens on finite, lifting wings and the magnitude of the drag is dependent on the wing's lift, it's also known as "drag due to lift."

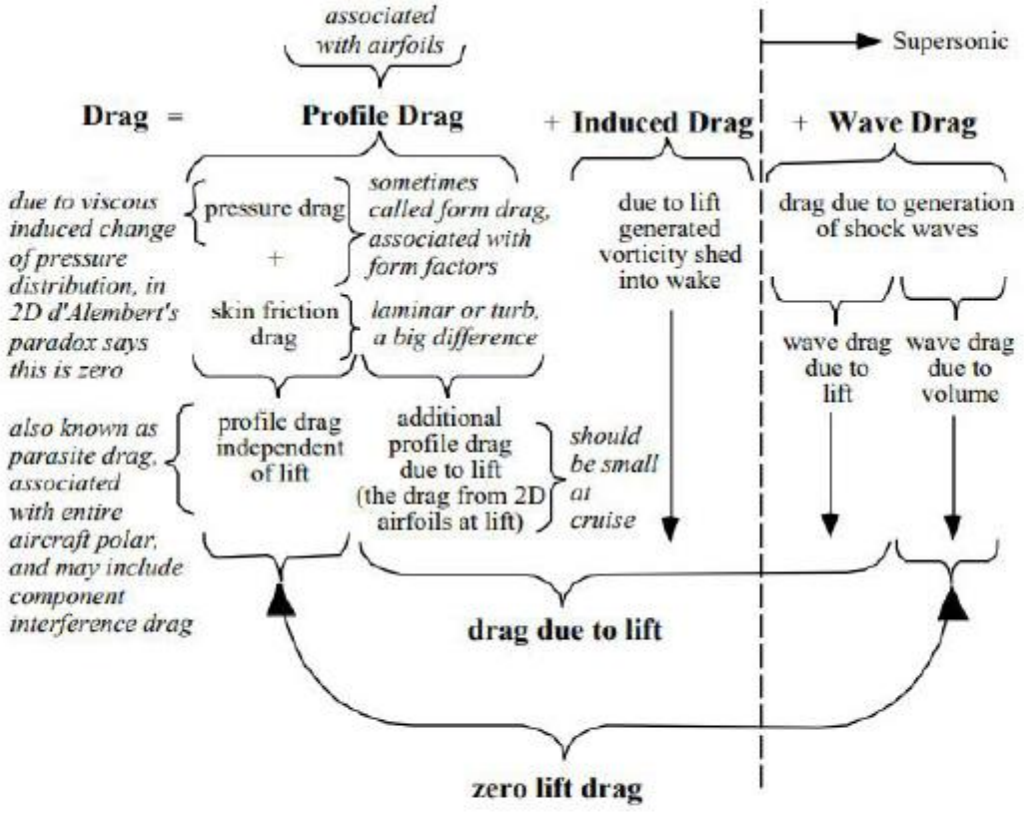

Figure 1. Drag Composition on 3D Wing (Schlichting, 1975)

2.2 Laminar and Turbulent Flows

To minimize the drag on the surface laminar flow is desirable. However, it is often impossible to obtain laminar flow due to high velocity or relatively large surface area of the object moving within the fluid. Unlike in the laminar flow where the streamlines go parallel to each other without disrupting the flow, streamlines within the turbulent flow interact one to another. This mechanism shows in Figure 2. Regions of impinging flow ("sweeps") mostly occur in regions of elevated pressure (yellow to red) while "ejections," i.e., where the flow moves away from the surface, correspond mostly to regions of lower pressure (blue to white). This exchange of fluid normal to the surface generates the enhanced shear stress of a turbulent flow because the high-speed flow is decelerated efficiently when it is swept towards the surface.

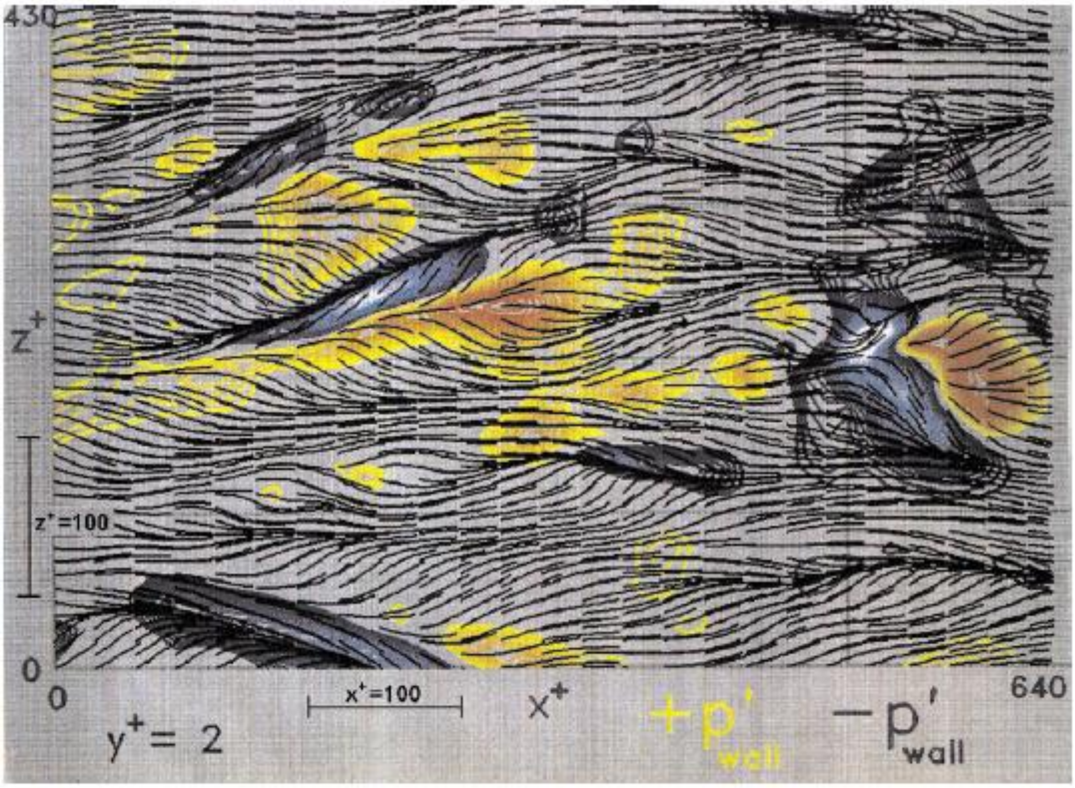

Figure 2. Instantaneous streamline pattern near a smooth wall (Bechert et al., 2000). Yellow to red zones represents the injection of faster moving streamlines to the slower region, whereas blue to white regions represent slower streamlines disrupting the faster flow.

2.3 Longitudinal Riblets

Most of the aquatic animals move with exclusive ease and agility can instantly reach relatively high speeds and perform sharp maneuvers. A good example is a shark. The skin is one of the main features letting them move through the water efficiently and maintain buoyancy. Figure 3 shows continuously distributed tooth-like looking dermal dentils covering shark's skin. This pattern covers the absolute majority of shark's skin. The grooves, illustrated in Figure 4, with regular spacing between protrusions (s) of 100-300 μm and typical height (h) of 180-500 μm are arranged in a way that the flow goes along them efficiently (Bhushan, 2009; Lang et al., 2012).

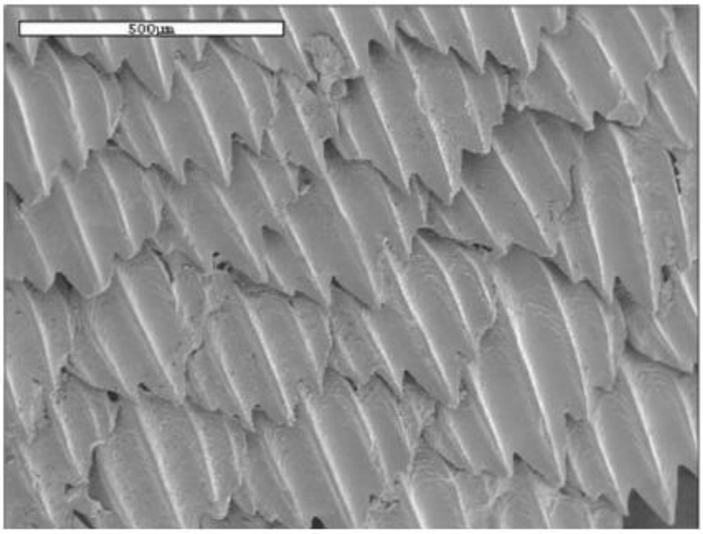

Figure 3 Scale structure of a Galapagos shark skin (Bechert et al., 2000)

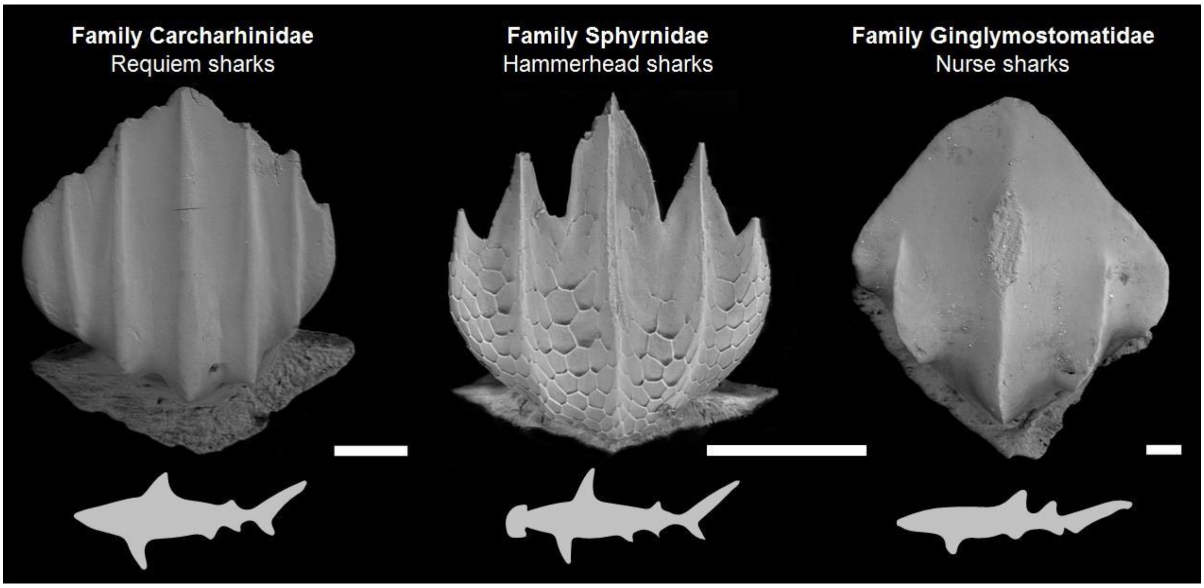

Figure 4. Scanning electron microscope (SEM) images of shark dermal denticles from the three main shark families. All the denticles were isolated from pieces of skin exoised from preserved museum specimens. Scale bar = 100µm. ©2015, Save Our Seas Foundation. Photo by Jorge Ceballos and Erin Dillon.

2.3.1 Functional Principles

A shark swims with relatively high velocity meaning the Reynolds number is high, and the flow is turbulent. Longitudinal scales on shark skin result in a reduction of wall shear stresses compared to the smooth surface. The problem with the smooth surface is that it significantly slows the closest layer of the flow around the body which in turn grasps even further layer causing it to slow down and leading to the creation of turbulent vortices. Shark skin reduces the creation of turbulent flow vortices in numerous ways: (i) the grooves adjust the flow direction by channeling it, (ii) the closest layer of the flow is accelerated as it goes by the narrower channel thus velocity difference within the boundary layer is lower, (iii) grooves pull faster moving water towards the surface and helps to mix it up with the slower current by the surface, (iv) dermal denticles spread the water sheet into smaller currents so that induced vortices are smaller (Bhushan, 2009). Longitudinal scales also execute the function of borders preventing the flow in transverse directions. They act like walls blocking the flow in transverse directions thus the wall shear stresses are reduced.

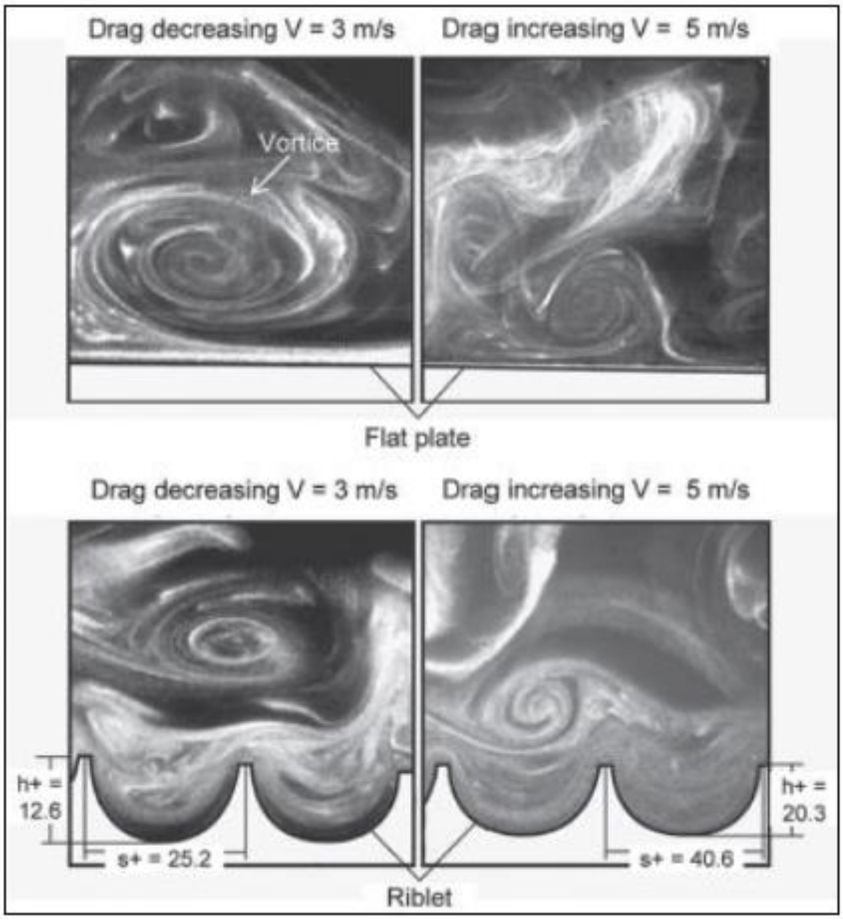

Figure 5. Flow visualization of vortices interacting with the flat and riblets surfaces using the smoke machines (Lee, 2001)

The working principle of longitudinal riblets is illustrated in Figure 5. It can be seen that the riblets lifts the vortex further away from the surface thus leaving only the tip in contact meaning reduced total shear stress compared to the whole surface area of the flat plate in contact with the vortex. Another benefit comes from pinning the vortex to the tip of the rib preventing the cross-flow movement whereas on a flat surface there are no such boundaries (Bhushan and Bixler, 2013). The riblets limit the spanwise migration of the vortices and produce secondary vortices in the case of drag reduction (Lee & Lee, 2001). As a result, the velocity fluctuations were found to be at a lower level. The gap is larger than the diameter of the quasi-streamwise vortices in the drag increasing situation at higher Reynolds numbers. The vortices can be seen closer to the wall and tend to stay there.

To make a positive impact riblets have to lift the vortices up. However, having protrusions increases surface area leading to increased drag. Hence it is essential to optimize riblets' geometry to achieve peak efficiency. Shark inspired geometries and configurations can be seen in Figure 6.

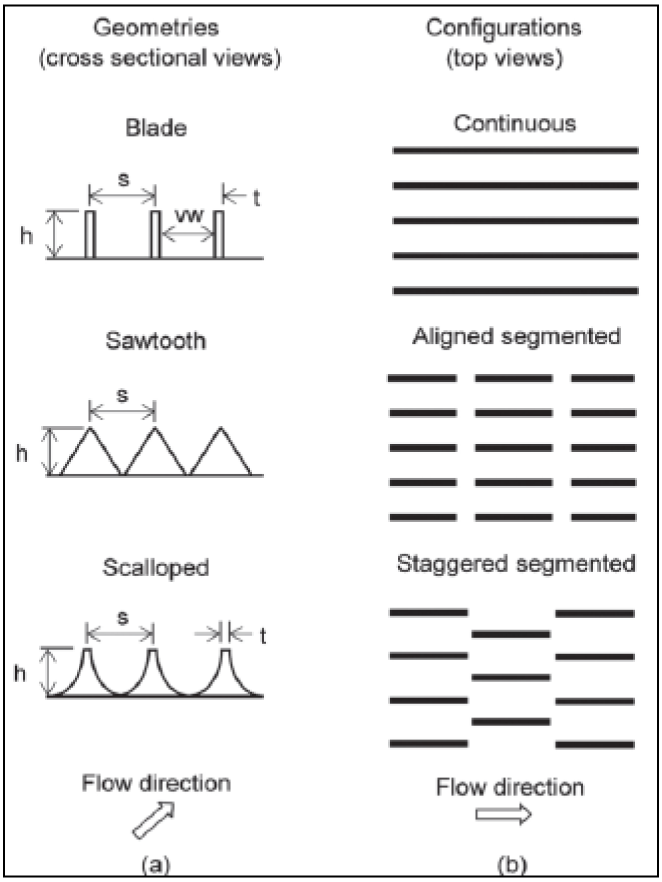

Figure 6. (a) Shark inspired geometries and (b) corresponding configurations (Bhushan and Bixler, 2013)

The parameters describing riblet's geometry are as follow:

Spacing $$s^+ = \frac{sV_\tau}{\nu}$$ **Equation 3**

Height $$h^+ = \frac{hV_\tau}{\nu}$$ **Equation 4**

Thickness $$t^+ = \frac{tV_\tau}{\nu}$$ **Equation 5**

Where V_τ is the wall shear stress velocity and can be expressed by

$$V_\tau = \left(\frac{\tau_0}{\rho}\right)^{1/2}$$

Equation 6

Where τ_0 is the wall shear stress, ρ is the fluid density and v is the kinematic viscosity (Bhushan and Bixier, 2013).

2.4 Herringbone Riblets

Bird's flight in the air is a more complex process compared to fish's movement in the water. Taking off, landing, immediate turning, gliding – all these different flight phases require a more sophisticated system to keep the bird airborne. Consequently, over the millions of years of evolution birds have formed flying mechanisms which distinguish them from the rest of the animal planet. The most crucial part of this mechanism is a wing. Different bird species introduce a wide variety of interesting wing shapes, but the majority of them can be collated with the existing aircraft wing models at least to some extent. However, there is one feature present on bird wings that cannot be found on any type of aircraft – flight feathers.

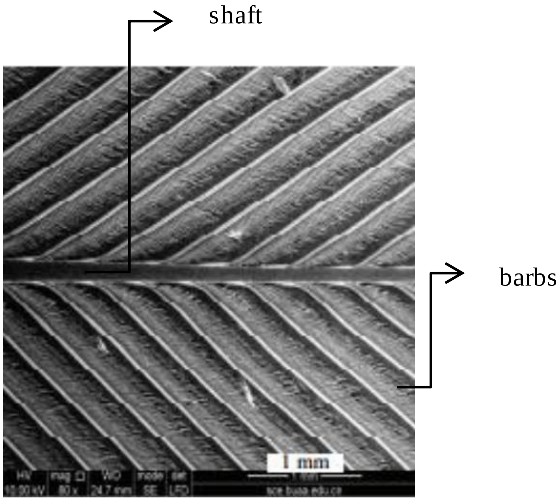

Figure 7. Bird feather structure

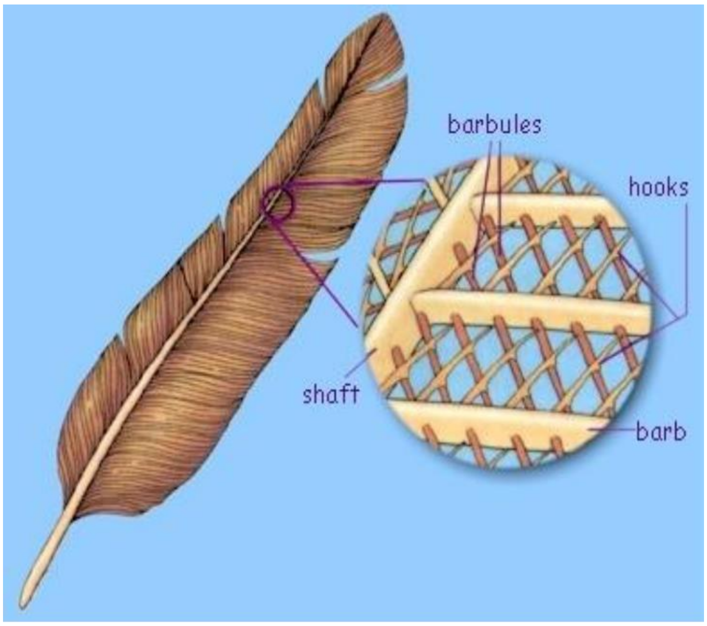

Figure 8 Micro-scale structure of bird feather on upper wing surface (Chen et al., 2013)

Generally, there are two types of flight feathers – primaries and secondaries. Primary feathers are the biggest which propel bird during flapping. However, the secondary feathers are the ones covering the most of the wing and accountable for the aerodynamics of the wing, especially in gliding phase.

Each feather consists of the supporting hollow shaft and numerous barbs distributed in two opposite directions along the shaft as shown in Figure 7. The barbs are interlinked with each other via barbules which consist of hooks pinning the barbules together. Furthermore, the feather is unsymmetrical along its shaft as the anterior vane is narrower compared to the width of the posterior vane. These two-part will be mimicked as the riblets.

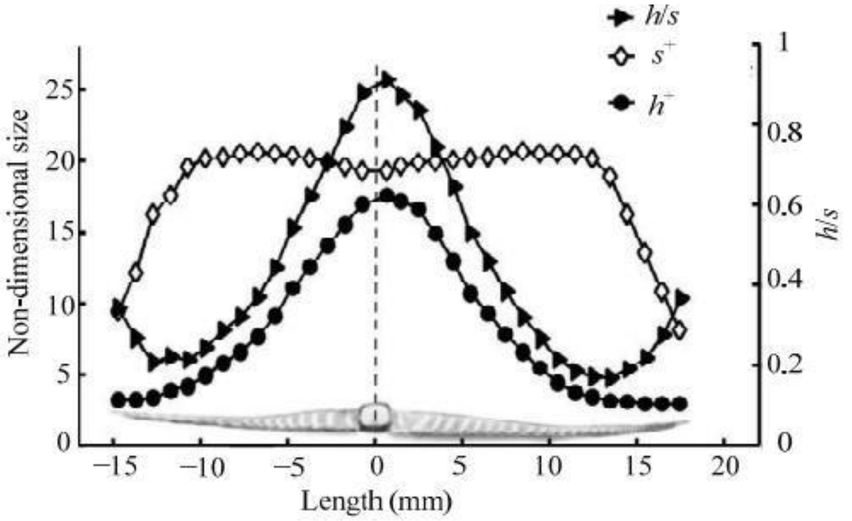

Figure 9. Parameters of secondary flight feather riblet structure (Chen et al., 2013).

The micro-scale surface structure of the bird feather is represented in Figure 8. It can be seen that barbs on both sides of the shaft are distributed parallel to each other. The two sides also form a yaw angle between them. Depending on species of birds, typical riblet width, s, at the centre of feather varies between 280 and 420 μm whereas typical height, h, is between 60 and 140 μm for the upper surface of the feather. Average yaw angle, θ, between two barbs on the opposite sides of the shaft is around 60° (Chen et al., 2014). However, spacing and especially height varies from the shaft to the outer fringe for each feather. The variation of herringbone riblet parameters is represented in Figure 9, where the kinematic viscosity is 1.502 x 10^{-5} m^2s^{-1}, freestream velocity 22 ms^{-1} and C_f = 4.59 x 10^{-3} (Chen et al., 2013; Yaws and Braker, 2001). Several details can be seen from the graph: the posterior vane is wider than the anterior vane; riblet spacing is nearly constant along the width of the feather except for a little fraction by the edge where the spacing decreases; riblet depth gradually decreases from the shaft to the fringe with the total reduction of 6-7 times.

2.4.1 Functional Principles

Unlike in the case of longitudinal riblets, the working principles behind the herringbone-type riblets are yet to be elucidated. The main existing explanation on functional principles so far belongs to Nugroho et al. (2013). An undertaken study disclosed that convergent/divergent riblet surface generates counter-rotating vortex arrays near the surface region, as shown in Figure 10. It is thought that this mechanism soothes the turbulence in the near-wall region by moderating the boundary layer and leads to a reduction in surface friction drag. Over the diverging region, the local mean velocity increases while the local turbulence intensity falls, resulting in a thinner boundary layer thickness. The opposite happens in the converging zone, with lower local mean velocity and higher local turbulence intensity, resulting in a thicker turbulent boundary layer locally. The thickness of the boundary layer varies by a factor of two across the pattern's repeated spanwise wavelength. The highly directed surface roughnesses are hypothesized to be forming large-scale counter-rotating roll-modes within the turbulent boundary layer, with common-flow-up (vertical flow away from the surface) occurring at the converging region and common-flow-down occurring at the diverging zone.

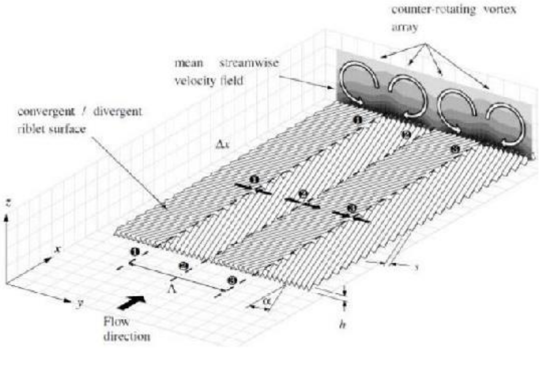

Figure 10. Counter-rotating vortex array present over convergent/divergent riblet surface (Nugroho et al., 2013)

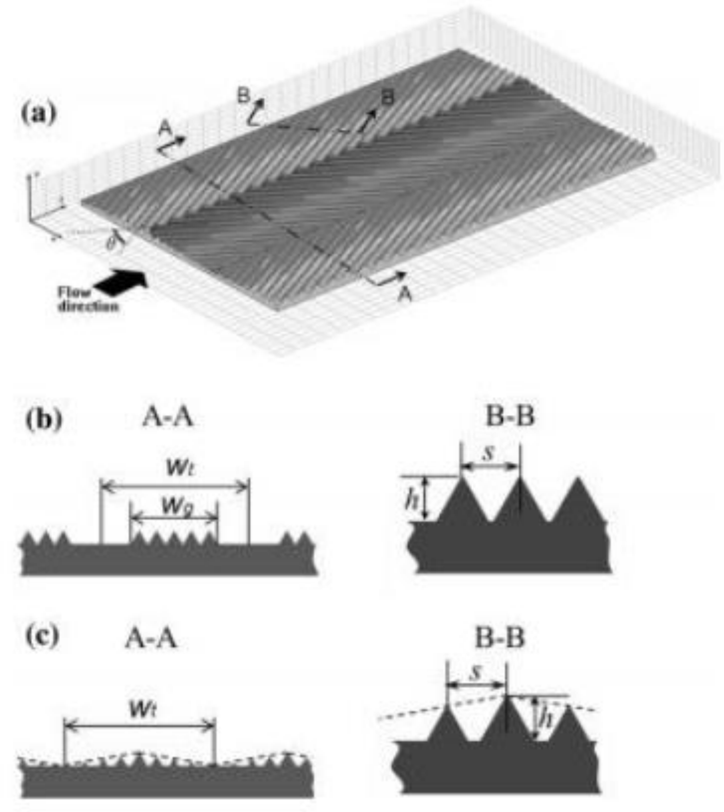

Figure 11

(a) Schematic of fluid flow upon the divergent/convergent riblet surface.

(b) The plane-3D herringbone riblet.

(c) The spatial-3D herringbone riblet. By Chen et al., (2014)

There are two types of herringbone riblets exploited so far: plane-3D and spatial-3D convergent/divergent riblets. If the conventional plane-3D riblets are characterized having a constant height, h, and a smooth fringe, the spatial-3D riblets distinguish having a constantly reducing height from the shaft to the edge, as explained in Figure 11.

The parameters describing riblet geometry i.e. spacing and height, in dimensionless wall units s^+ and h^+, respectively, are the same as for longitudinal riblets (Eq. 3 and 4).

2.5 Background Research

2.5.1 Experimental Methods

Open and closed channel experiments are employed to quantify the benefit in drag reduction provided by the presence of riblets. Two most conventional open channel methods are water/oil channel and wind tunnel testing. In both cases, the object, e.g., aerofoil, flat plate, is placed inside testing section within the facility but different approaches to measuring the drag are used.

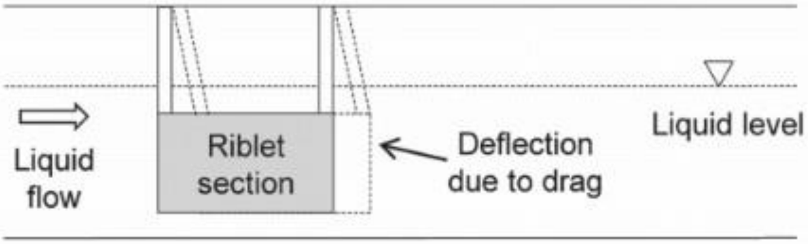

Figure 12. Water/Oil channel force balance method (Bhushan and Bixler, 2013)

In water/oil channel experiment the specimen with fitted riblets is mounted on a force balance and lowered into the constant current liquid flow to measure the drag resistance force exerted on the specimen as shown in Figure 12. The percentage drag reduction $\Delta\tau/\tau_0$ (%) can be calculated, where $\Delta\tau$ is the difference of shear stresses between riblet sample (τ) and the smooth surface (τ_0) (Bhushan and Bixler, 2013).

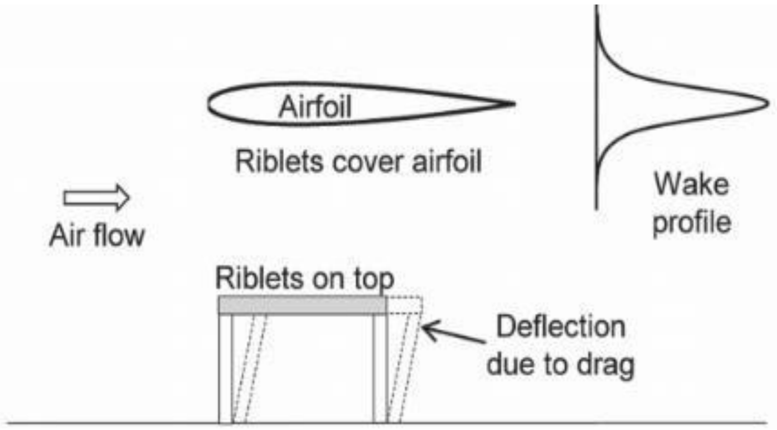

Figure 13. Wind tunnel wake profile and force balance methods (Bhushan and Bixler, 2013).

On the other hand, wake traverse method can be used in wind tunnel testing as shown in Figure 13. The pressure of a traversed downwind from the aerofoil is measured using wake probe in order to determine the drag exerted on the aerofoil. Hence, measured pressure in the aerofoil wake can be compared to that of a smooth aerofoil to calculate the drag reduction. The drag coefficient (C_D) is then calculated using the data from the wake pressure profile (Bhushan and Bixler, 2013). Again, drag reduction percentage expressed as a drag coefficient difference ΔC_D (%) between smooth and riblet surfaces can be calculated using following formula:

$$C_D = \frac{F_d}{0.5\rho V^2 A_w}$$ **Equation 7**

where V is the velocity calculated from the wake pressure profile, F_d is the drag force, and A_W is the total surface area in touch with the flow (White, 1991). Wake survey method adopted in this study will be describe in Appendix B. Earlier described force balance method is also available using the wind tunnel.

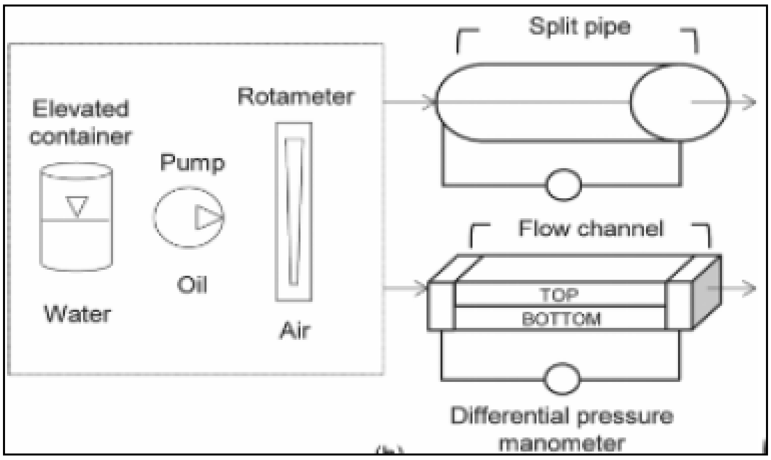

Figure 14. Closed channel drag measurement method (Bhushan and Bixler, 2013).

The closed channel experiments are also suitable for testing surface structures. Structures, like riblets, are applied to the interior surface of the pipe, and the water, oil or air flow is run through the pipe. The pressure manometers are applied at different locations within the pipe to capture the pressure change, as illustrated in Figure 14. The drag reduction can then be measured either as the difference in shear stress $\Delta\tau/\tau_0$ (%) or pressure $\Delta P/P_0$ (%) (Bhushan and Bixler, 2013).

2.5.2 Experimental Results from Literature

2.5.2.1 Longitudinal Riblets

A bulk of experimental data has been compiled from the experiments testing riblet surface ability to reduce the drag. As reported by Bhushan and Bixler (2013) flat plate with fitted riblets testing in an open channel in majority cases showed results of maximum turbulent drag reduction between 4.9 and 9.9 per cent.

Bechert et al. (1997) using oil channel experiments determined optimal rib height of h = 0.5s. They also concluded that the optimal shape for each rib is thin blade rather than sawtooth (Bechert et al., 2000). Figure 15 shows significant shear stress reduction of 9.9

per cent compared to the smooth surface using thin blade ribs of thickness t = 0.02s (Bechert et al., 1997). The graph also shows that peak performance in drag reduction for all given rib geometries tends to happen within a certain s+ range between 10 and 20.

The riblets geometry scale small enough since this reduction mechanisms take place inside the boundary layer. By keeping the vortices above the riblet tips, the cross-stream velocity fluctuations inside the riblet valleys are much lower than the cross-stream velocity fluctuations abovea flat plate. The shear stresses in the valleys are much lower than that of the tops. This difference in cross-streamvelocity fluctuations is the evidence of a reduction in shear stress and momentum transfer near the surface, which minimizes the effect of the increased surface area.

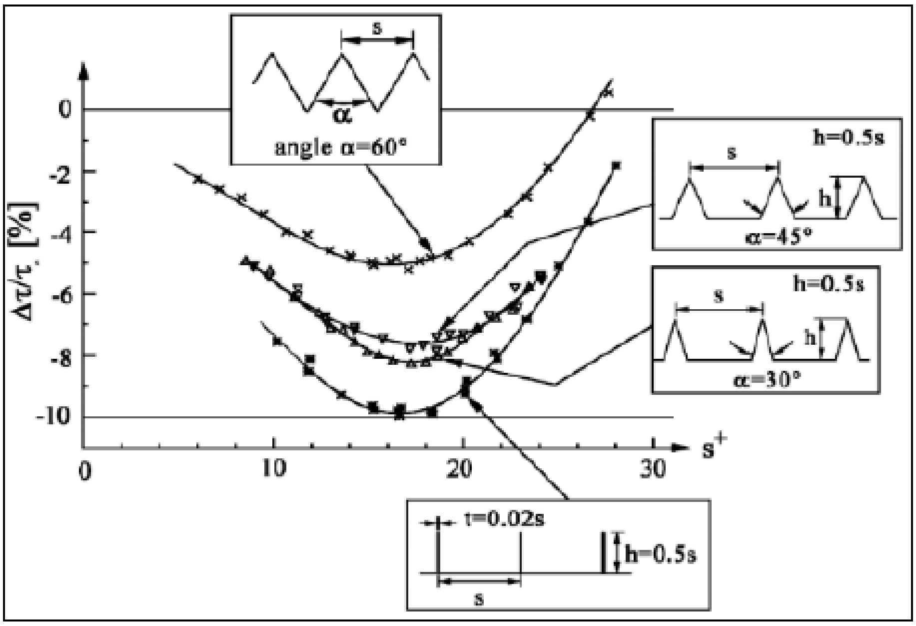

Figure 15. Closed Channel Drag Measurement Method (Bhushan and Bixler, 2013)

However, a rather significant result was captured 8 years before Bechert et al. achieved impressive 9.9 per cent reduction when in 1989 Neumann and Dinkelacker achieved 13 per cent reduction of the turbulent drag. Furthermore, the result was achieved using sawtooth rib geometry that was 8 years later settled as less effective compared to the blade type riblets. The results of experiments can be seen in Figure 16. Using riblet film of s = 0.152 mm the resulting curve on drag reduction graph does not follow the usual ‘dipping’ tendency within s^+ range between 10 and 20 as it can clearly be seen in corresponding Bechert et al. (1997) results as well as other similar experiment results by others. Even in their own results, this tendency can be clearly captured for riblet films of s = 0.075 mm and s = 0.051 mm. However, this exceptional case, or in other words, an anomaly, was explained in their report. According to the post-experiment report, it was a case when the transition from laminar to turbulent flow occurred within s^+ range of 10^{-5}, and the turbulent structures were delayed thus a larger drag reduction was possible (Neumann and Dinkelacker, 1991). Generally results achieved in oil tunnel were better compared to water tunnel with drag reduction of up to 10 and 6 per cent, respectively. Hence, following results presented in Figure 17 are obtained using oil channel. Figure 17 shows results of experiments carried out using four different size of riblets saw tooth shaped. It can be highlighted that the best result of 9 per cent drag reduction was achieved using blade type riblets with h/s = 0.5 and t/s = 0.04 at s^+ of around 15 (Bechert et al., 1997). As it was revealed earlier, the result was further improved to 9.9 per cent by reducing blade thickness to t/s = 0.2 (Bechert et al., 1997). However, sawtooth and scalloped geometries reached their peaks at around only 6 and 7 per cent of drag reduction, respectively. Another trend worth noticing is that the performance of sawtooth riblets was increasing with decreasing angle, peaking at α=54°. Bechert also conduct the experiment in the wind tunnel with very small size compare to those applied in the oil channel. Viscousity have some affect in the effective size of the riblets.

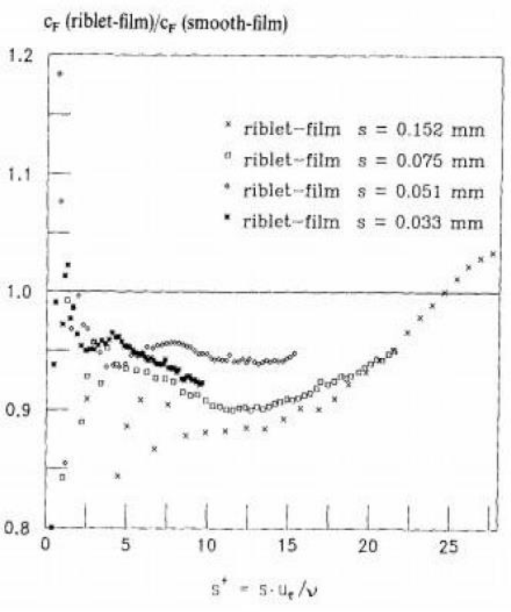

Figure 16. Drag reduction performance using different riblet geometries. Results of Bechert et al. (1997). Copyright 1997, Cambridge University Press

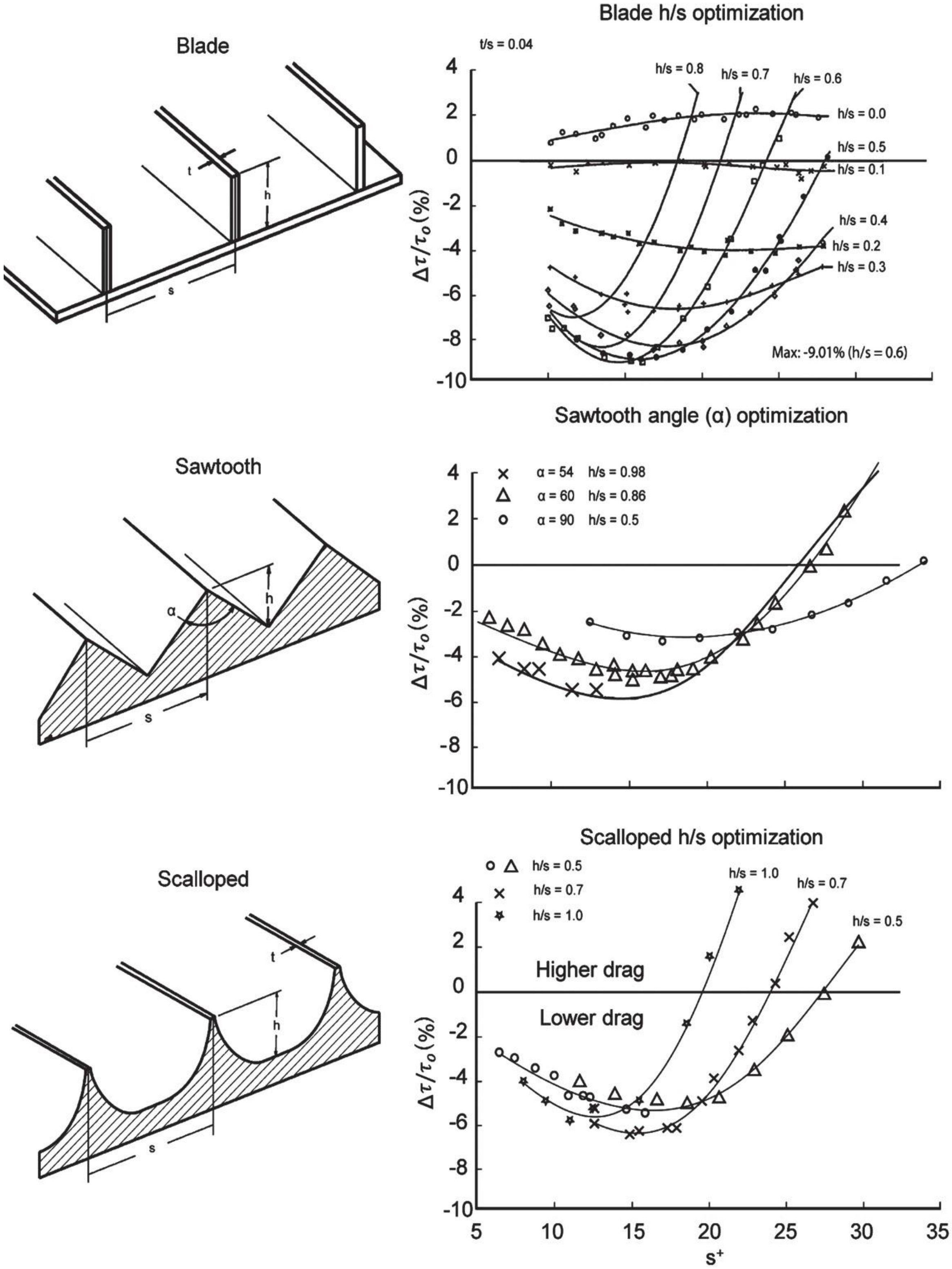

Figure 17. Turbulent drag reduction using different size of s=h film compared to smooth surface (D.W. Bechert, M. Bruse,W. Hage, J. G. T. Van der Hoeven, and G. Hoppe., 1997).

Figure 18 explains the difference between results achieved by staggered segmented and continuous blade riblet configurations. The latter provides notably higher drag reduction performance at the peak, however, at the price of shorter 'effective' s^+ range compared to staggered segmented blade riblets configuration.

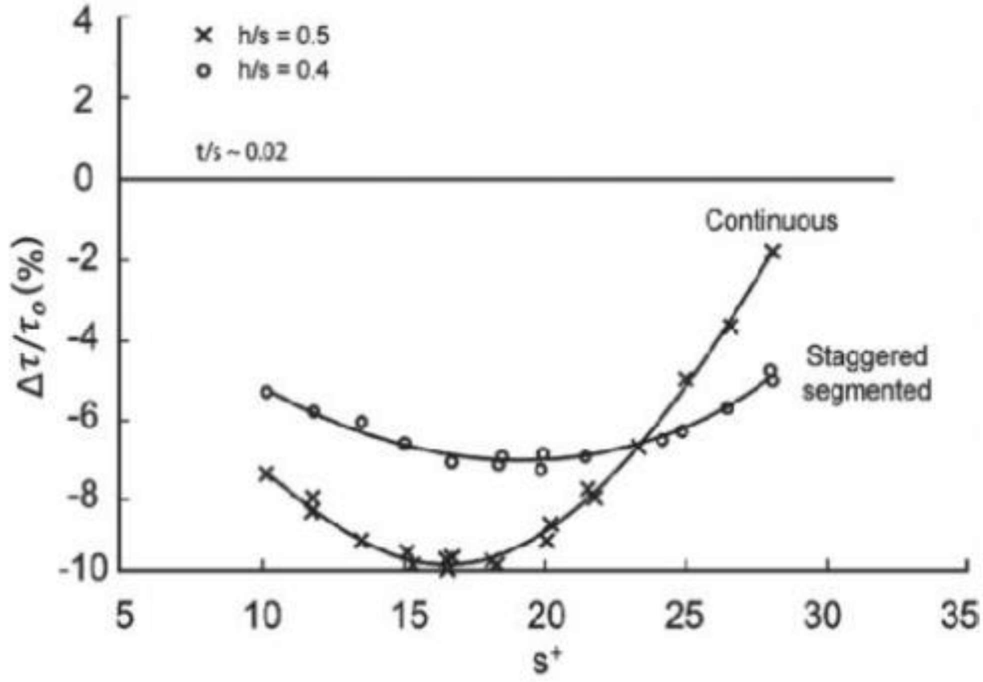

Figure 18. Turbulent drag reduction using s=h film compared to smooth surface (Neumann and Dinkelacker, 1991).

Similar trends could be seen in Figure 17 presented earlier. For blade type riblets of the same configuration but different h/s ratio, either high peak drag reduction value or reduction of drag over a wider s^+ range can be achieved. For instance, at h/s range of 0.2-0.3 drag reduction does not vary much and does not achieve significant peak, however, reduces drag almost constantly over the range of s^+ from 10 to nearly 30. On the other hand, h/s ratios between 0.4 and 0.8 can achieve significant peak drag reduction at certain s^+ value but then further away from the peak value performance suddenly drops to almost drag increasing zone. Thus it can be deduced that for certain types of missions different geometries and configurations might be used in order to achieve the best performance, e.g., when the operating velocity isconstant higher h/s ratio might be beneficial whereas when operating over the range of velocities lower h/s ratio would give an advantage.

Wind tunnel experiments are conducted using aerofoils with the riblet ‘skin’ stuck to the surface in order to determine how advantageous it can be compared to the smooth surface. 3M vinyl riblet sheets seem to be the most convenient option thus the results are based on this sort of ‘skin’. Figure 20 shows the effect of riblet film stuck on wind turbine DU 96-W-180 blade put into subsonic wind tunnel whereas Figure 19 shows results of symmetrical wing profile NACA 0012 with the same film but put into transonic speed flow.

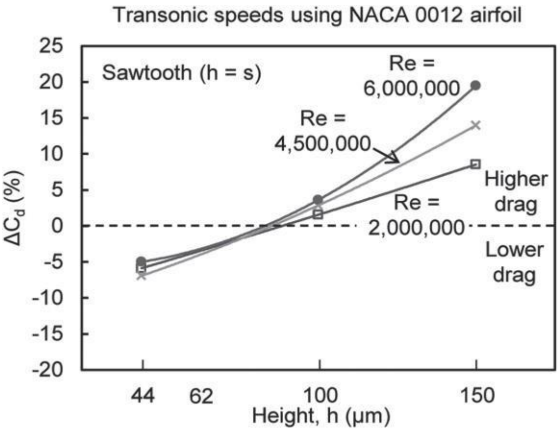

Figure 19. Drag reduction around symmetrical wing profile NACA 0012 (Bhushan and Bixler, 2013).

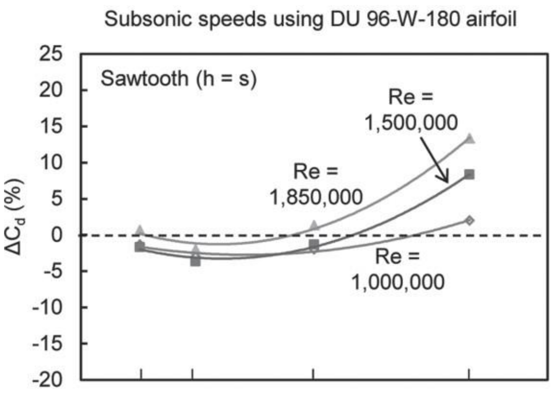

Figure 20. Drag reduction around wind turbine blade DU 96-W-180 (Sareen et al., 2011).

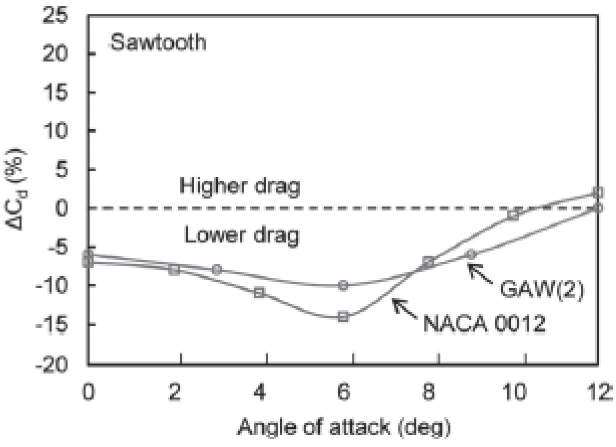

Figure 21. Drag reduction on NACA 0012 and GAW(2) aerofoils with 'skin' under different angles of attack (Subaschandar et al., 1999).

Results from the graph shown in Figure 20 state the peak reduction of nearly 5 per cent occurring with sawtooth riblet of size h = s = 62 μm. Figure 19, however, shows almost linearly increasing drag with increasing sawtooth riblet size. Highest drag reduction of around 7 per cent is achieved using finest riblet sheet with a size of h = s = 44 μm at the Re 4,500,000. The results from this experiment also suggest the idea that for increasing flow Mach number (hence increasing Reynolds number) the corresponding boundary layer thickness around an aerofoil decreases thus higher riblets may start protruding turbulent viscous sublayer. Hence, turbulent flow vortices are not lifted and pinned to the tip of the riblets.

Figure 21 shows another interesting relationship between drag reduction and the angle of attack using 3M vinyl riblet sheets on NACA 0012 and GAW-2 aerofoils. Interestingly, even though NACA 0012 is symmetrical aerofoil and GAW-2 is asymmetrical they both have a peak of drag reduction achieved at the same angle of attack of 6 degrees. However, symmetrical NACA 0012 achieves notable 15 per cent drag reduction whereas GAW-2 only around 10 per cent at the peak.

2.5.2.2 Herringbone Riblets

Only a tiny fraction of the amount of data involving experiments on longitudinal riblets is available assessing herringbone-type riblets. Consequently, lack of knowledge within the field stimulates the need and desire to explore this innovative approach of drag reducing technique further. Chen et al. (2013) were the first ones to investigate bird feather microstructure and propose herringbone-type wall riblets as a drag reducing novelty.

The selected approach to assess the herringbone riblets was a water tunnel test. The inner surface of the pipe was covered by the skin replicating herringbone riblets and was fabricated using moulding technique. The drag reduction rate (DR) was defined as the pressure difference between the smooth and bird feather inspired skin.

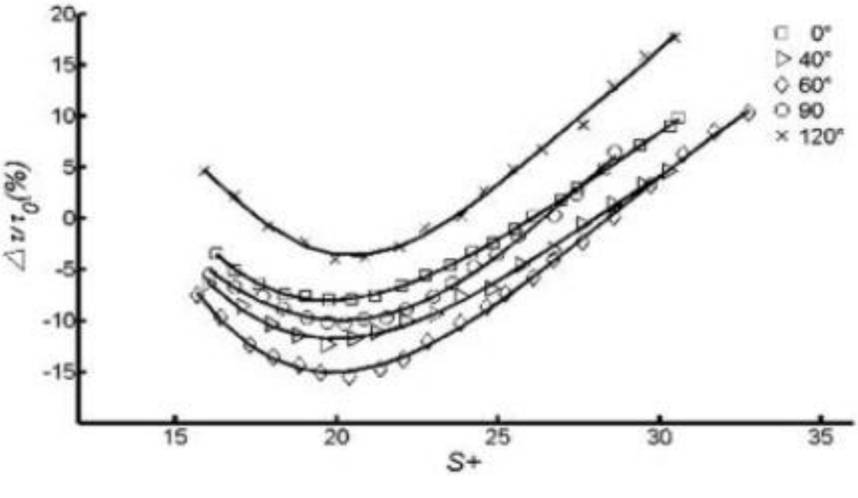

Figure 22. Effect of yaw angle between planar-3D herringbone riblets on drag reduction (Chen et al.,2014).

Firstly, using planar-3D herringbone riblets the effect of yaw angle between the riblets was assessed. The results, shown in Figure 22, suggest that the most efficient yaw angle between the riblets is around 60° with the total drag reduction of around 17% compared to the smooth surface. Furthermore, 0° angle representing longitudinal riblets showed 7% drag reduction which closely collates with the previously carried out experiments affirming the validity of the test.

Moreover, once the optimal yaw angle was determined the second test was executed to assess the difference between the planar and spatial 3D herringbone riblets. The results showed that more closely to nature related spatial riblets showed an increased drag reduction compared to the planar ones, as shown in Figure 23. The graph testifies significant 21% reduction which is more than twice improved drag reduction compared to the longitudinal riblets (9.9% by Bechert et al., 1997).

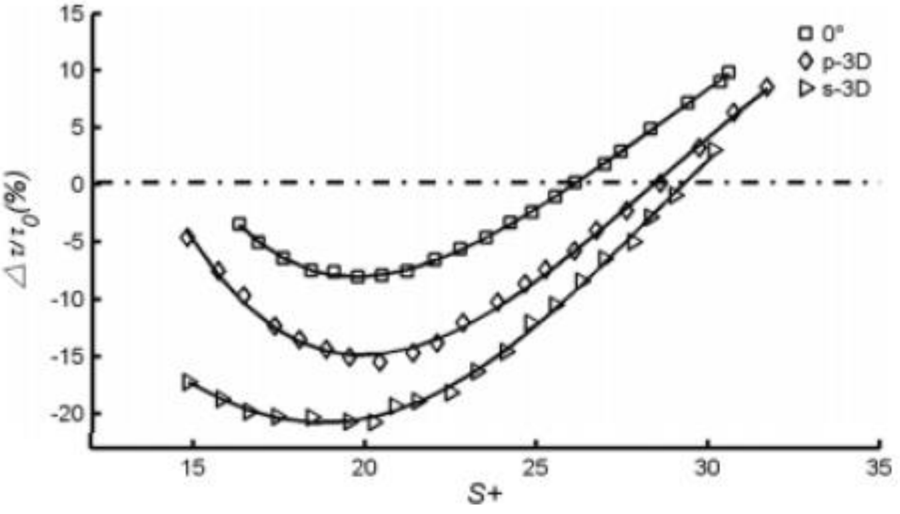

Figure 23. . Comparison of drag reduction between longitudinal and herringbone planar and spatial riblets (Chen et al., 2014).

However, since the significant result in drag reduction was achieved by Chen et al. (2013) nobody else managed to get similar to those results. Furthermore, Benschop and Breugem (2017) recently published a research article on drag reduction by herringbone riblets in direct numerical simulations. Astonishingly, after completing a variety of simulations they declared that employment of herringbone riblets in most cases is detrimental to turbulent drag reduction. At the same time, they confirmed the beneficial effect of longitudinal riblets by achieving very similar to Bechert et al. (1997) result of

9.3% drag reduction (compared to 9.9% DR). Hence, the opposing results leave a gap in the theory of herringbone riblet's ability to reduce the drag and should be researched further

.

3 Experiment Preparation

To have a better understanding of the flow mechanism near the herringbone-type riblets effect, it was anticipated to run a wind tunnel experiment. The experiments overviewed in literature gave an insight into how the testing should be conducted and what preparation needs to understand before it takes place. Hence, to make it as closely related to nature as possible it was decided to attempt in creating a replica of a bird wing as well as a re-creation of its feathers' surface structures, i.e. micro-scale herringbone riblets.

3.1 The Bird Wing Model

It was chosen to build a pigeon wing model, as seen in Figure 24, to serve for this experiment. The decision of building a pigeon wing model was made considering its suitable size for wind tunnel testing as well as relatively less complicated shape for manufacturing purpose compared to other bird wings.

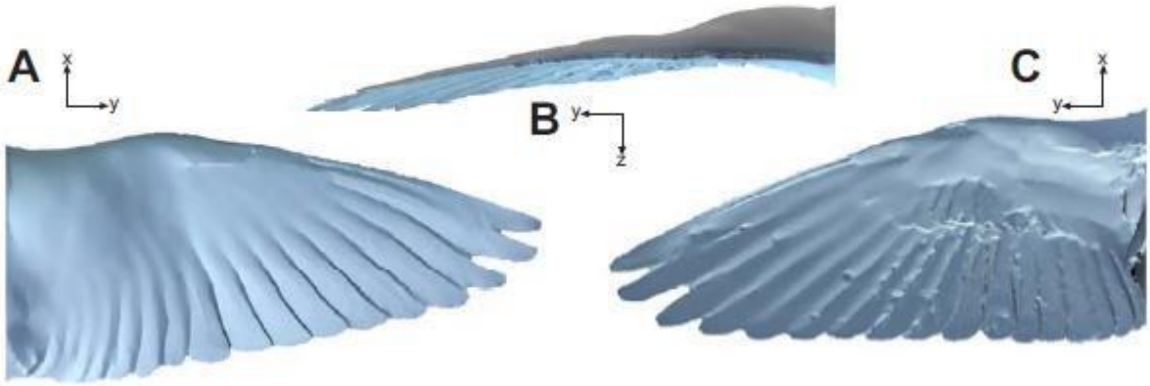

Figure 24 Surface view of a digitised pigeon wing - (A) dorsal, (B) frontal, (C) ventral (Bachmann, 2010).

For re-creation of the pigeon wing, it was necessary to find information about the geometrical parameters of the wing. Lack of numerical data describing the exact features made it challenging to reproduce the exact shape of a pigeon-inspired wing. Fortunately, an essential piece of information was acquired from the dissertation written by biologist Thomas Willem Bachmann (2010). He provided the table, shown in Appendix A, of maximum thicknesses and camber values at several locations along the span of a pigeon wing and their exact locations at the corresponding chords. Besides, the sketch of a pigeon wing shown in Appendix A was used as a base to construct a 3D pigeon wing model on the CAD design software SOLIDWORKS in order to manufacture it using a 3D printer.

The pigeon wing model, shown in Figure 25, was manufactured by the 1 x 1 x 0.5 m FDM printer using PLA filament. However, the surface finish was not of the suitable standard for testing micro-scale structures as the plastic finish was not smooth; the filament layers were visible and could be sensed when touching. Hence it was essential to smoothen the surface as it is a principal requirement for covering process as well as it could interfere with the flow an effect on drag reduction. Consequently, the surface needs sanding and spray-painting technique. After five iterations the desired surface smoothness was achieved for the testing model.

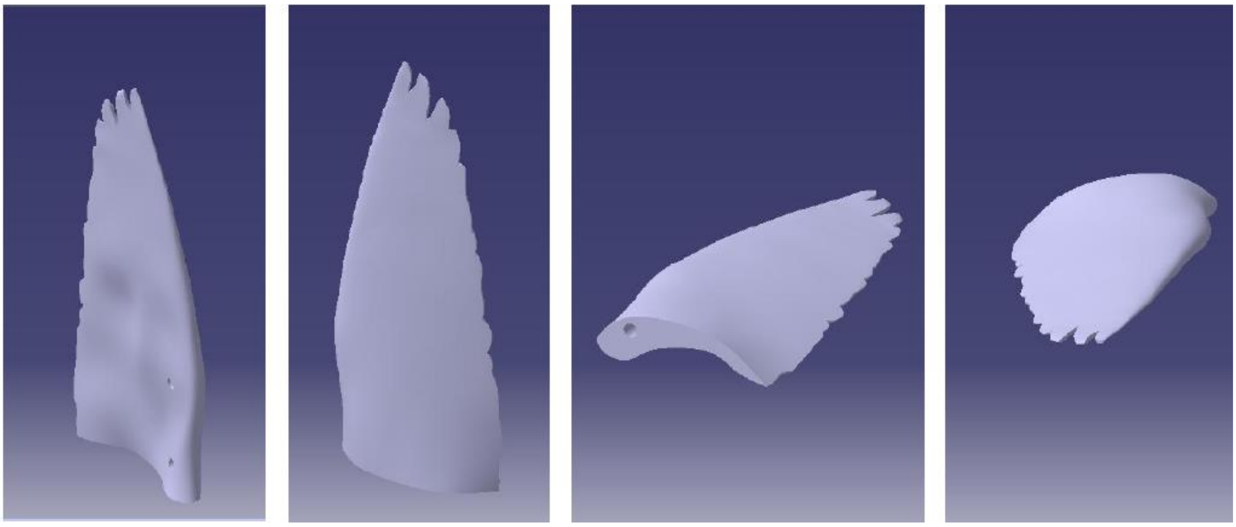

Figure 25 3D printed pigeon wing model.

4.2 2D Model

In order to study how this herringbone riblets will influence the flow around the model especially near the surface, a 2D model had also design and manufacture. This two-dimensional model has simple rectangular planform with S1223 as the aerofoil section. The shape of this aerofoil closed to some bird wing section. Some experiment result from other research shows that this aerofoil produces a good performance in low Reynolds number.

The size of the test section will limit the size of the wing model. The interference of the wall to the flow around the model gives a direct impact on the quality and accuracy of the data since the boundary layer also developed on the tunnel wall. The solid blockage should be between 0.01 – 0.1 or generally accepted 0.05. For 2D flow model, the span of the wing should be between 40% - 60% of the tunnel width.

The aspect ratio of the model will also influence the aerodynamic characteristic of the wing. Some experimental result shows that on the low-speed regime the mushroom-shaped stall model occurs on the wing (Pope, 1965). The aspect ratio beyond three will give a better result and need no data correction. The manufacturing process also define the size of the model since sometime some tools has also its limitation. For this case, the tools could not cut the raw material perfectly while the thickness of the trailing edge lower than 0.5 mm.

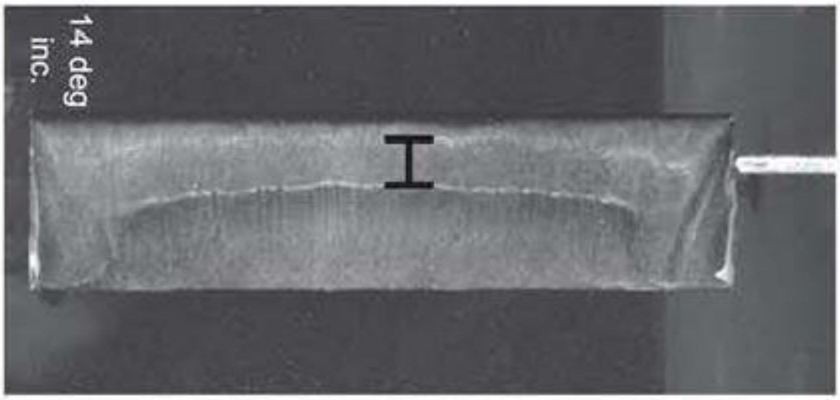

Figure 26. Mushroom Pattern occur on the upper surface of FX63-137 wing with AR = 4 at angle of attack 14 degree

Table 1. Geometry of 2D Model Airfoil S1223

Section Profile	:	S1223	
Span	:	450	mm
Chord	:	150	mm
Maximum Thickness	:	24	mm
TE Thickness	:	0.56	mm

Wing model made of metal material and manufactured using a CNC machine. The drawing of the model can be seen in Figure 27.

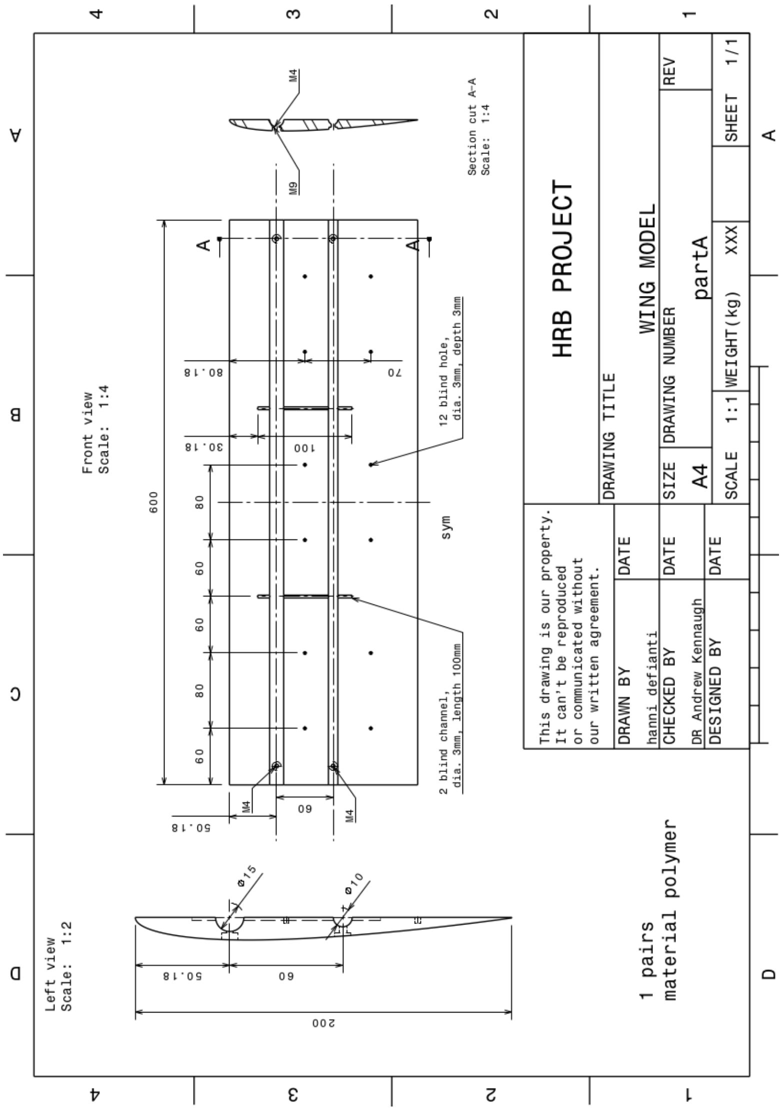

Figure 27. Detail Drawing 2D Model

4.3 Manufacturing Riblets

The riblets were modeled in a way so they would represent the actual feathers on the upper surface of a pigeon wing, as shown in Figure 28.

The riblets made by non-metal material and marked by the laser machine. The machine-controlled through computer software. First of all, we draw the pattern with this software. The strength of the power, the frequency of the laser and cutting speed were defined through this software. Those variables could affect the quality of the pattern on the material.

This laser marker machine produces low wavelength, only 1064 nm. With this machine, the maximum depth of the gutter could be made without damage is only 75 µm. The limitation size of the working table causes the maximum length of the riblet film can be made using this machine only 142 mm.

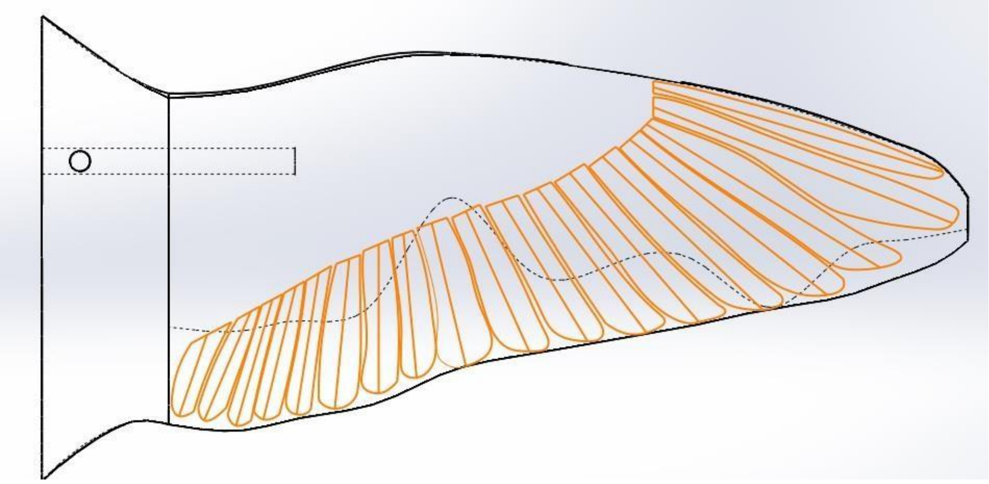

Figure 28. Herringbone riblet foils representing pigeon wing feathers.

The riblets are produced on a foil with a thickness of 120 µm. The foil is then glued onto the upper surface of the wing model as shown in Figure 29. A total of 18 foils of varying lengths, widths and shapes were stuck across the span of the wing in a certain formation to represent the feathers.

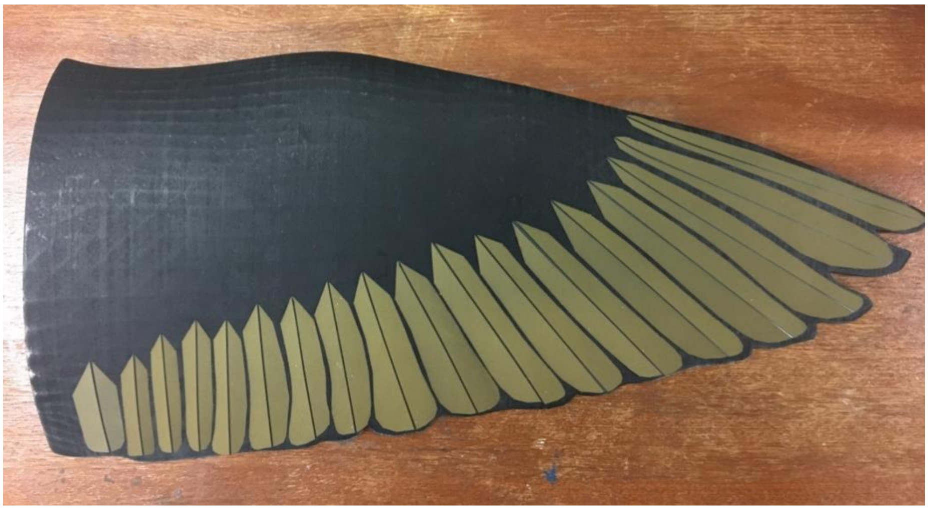

Figure 29. . Riblet foils on the pigeon wing model.

For 2d model made 11 similar size riblets. The depth of the microstructure completely the same as the one made for the 3d model. However, the width and the length defined from the previous experimental result. The length of the riblets decided from the first bubble separation occurs on the model at Reynolds number 80000. The width determined from the previous experiment which showed that the best performance could be achieved while the width only a third of the length.

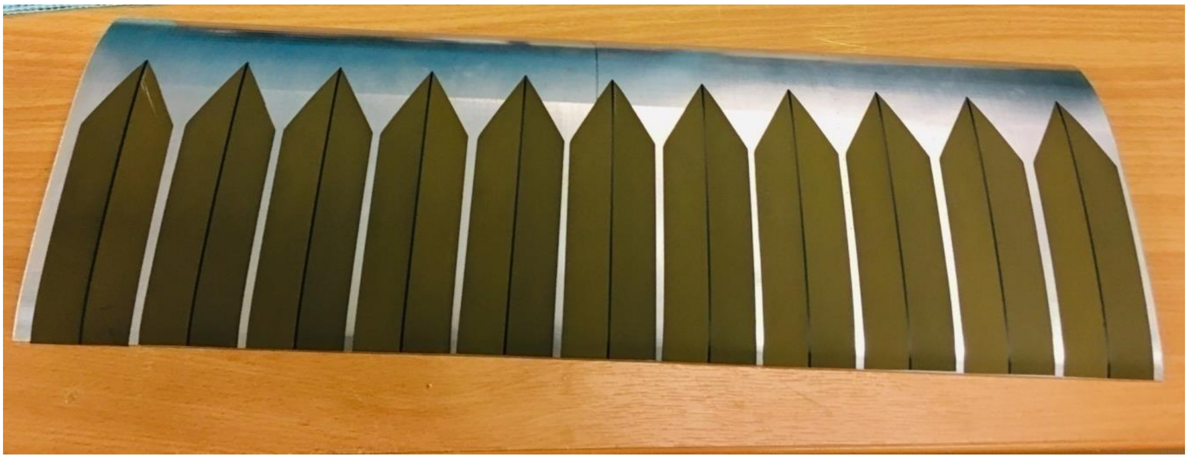

Figure 30. Riblet foils on the S1223 wing model

Even though length and width for each of the foils are varying, the divergent angle of the grooves stays constant at θ = 60°, with 30° on each side of the centre line. The groove depth and width are 80 µm and 300 µm, respectively, as it was measured to be on an actual pigeon feather in the upper wing (Chen et al., 2014). Pictures made by scanning electron microscope (SEM), shown in Figures 31, 32 and 33, give an insight into the microstructure.

Table 2. Geometry of Riblets of 2D Model

	Value	Units
depth	**80**	**µm**
width	**300**	**µm**
angle	**60**	**degree**
Film width	**40**	**mm**
Film length	**120**	**mm**
Space between film	**2**	**mm**

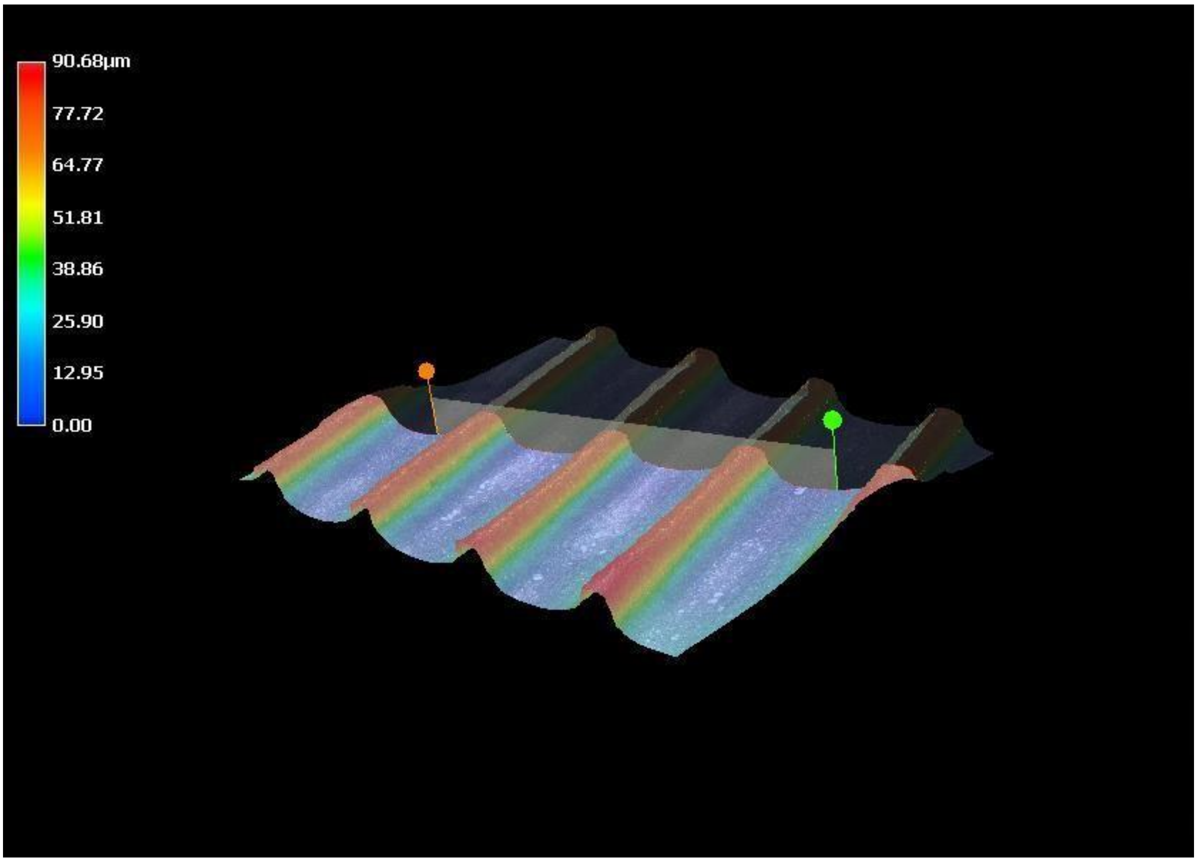

Figure 31. 3D view of herringbone riblets by SEM

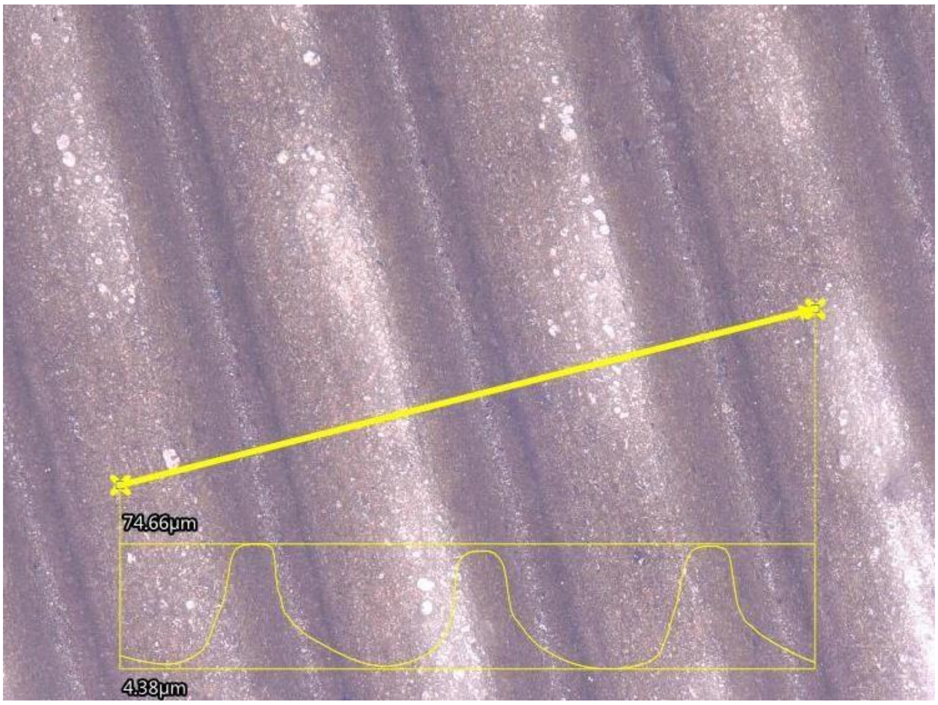

Figure 32. Picture of herringbone riblets by SEM

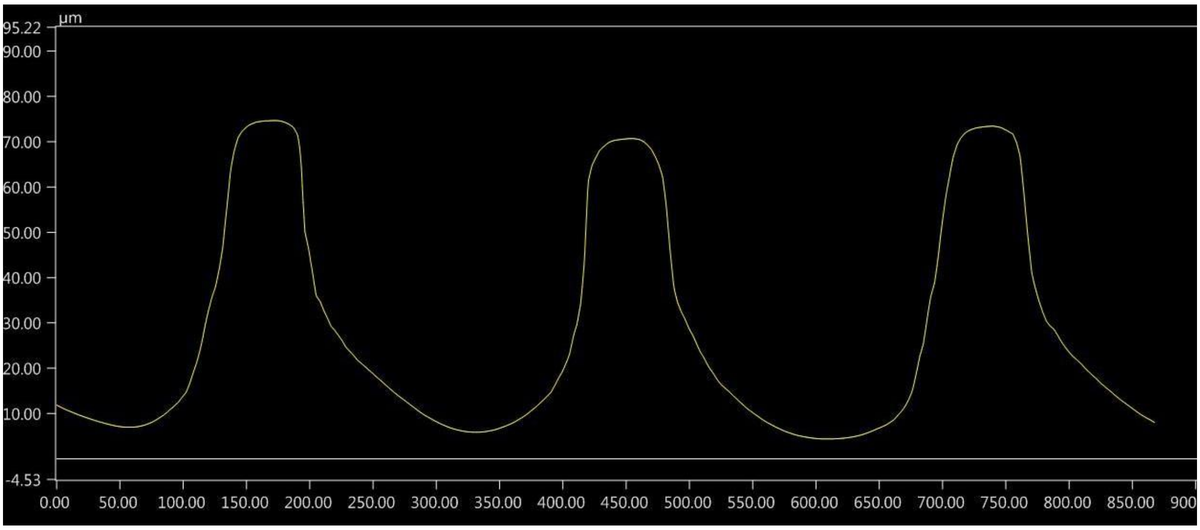

Figure 33. Cross-sectional view of herringbone riblets by SEM

4.4 Attachment Mechanism

The attachment mechanism had to be designed to be able to attach the pigeon wing model to the force balance beam so the flow parameters could be captured. Furthermore, it had to be modelled in a way so it would be possible to change the incidence angle from the outside of the wind tunnel and it also would not affect the flow. Consequently, the model shown in Figure 34 was submitted to the workshop for manufacturing.

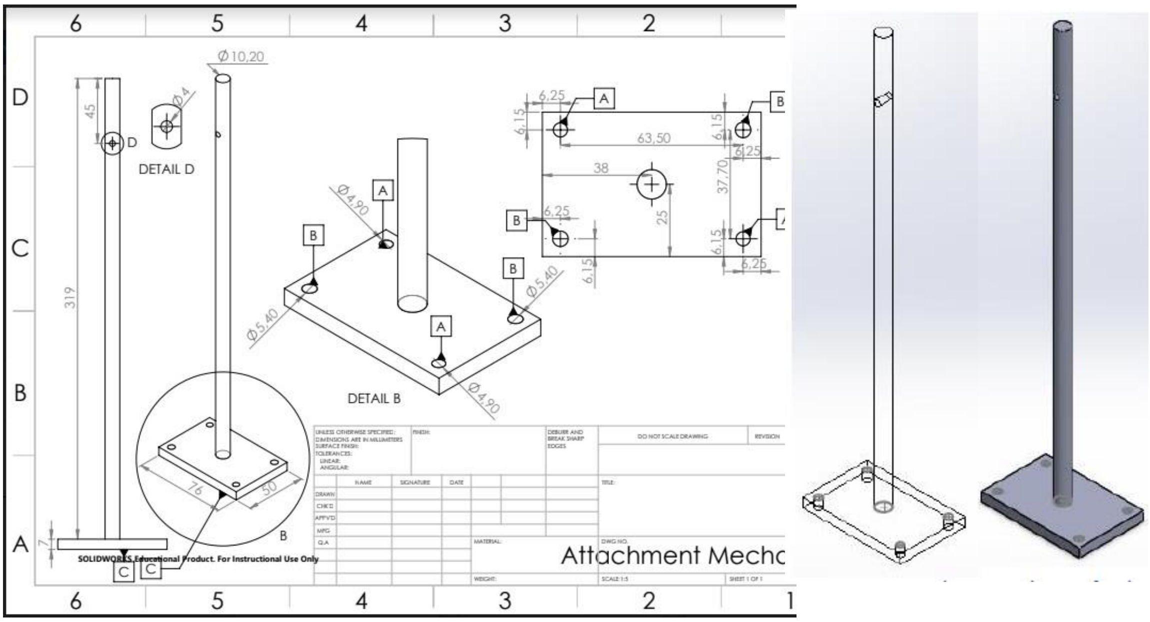

Figure 34. Detail Drawing of the attachment mechanism for the wind tunnel testing of a pigeon wing model

5 Experimental Apparatus

This section presents a detailed description of the project tunnel subsonic wind tunnel facility, test section flow quality, lift and drag measurement technique, data acquisition equipment, and data reduction procedures that have been documented.

5.1. Wind Tunnel Facility

The low Reynolds number airfoil performance measurements described here were conducted in the Project Tunnel shown in Fig. 35. The wind tunnel is an open-return type. The rectangular test section is nominally 1000 mm x 1000 mm in cross-section and 3 m long. The test section speeds are variable up to 30 m/s via 75 kW AC motor connected to a fan.

Figure 35. Bob Tunnel of University of Manchester situate at ground floor George Begg Building

Since low Reynolds number airfoil performance is highly dependent on the behaviour of the laminar boundary layer, low turbulence levels within the wind tunnel test section are necessary to ensure that laminar flow does not prematurely transition to turbulent flow. The wind tunnel settling chamber contains a thick honeycomb in addition to 4 anti-turbulence screens. These parts will provide good flow quality in the test section and can remove partially for cleaning. The turbulence intensity was measured and previously reported to be 1.04 m/s at 15 m/s.

The Reynold model number is calculated based on the length of the chord with the following equation,

$$\Re e = \frac{\rho U_\infty c}{\mu}$$

Equation 8

U_∞ for free stream velocity in test section, c for airfoil chord, ρ for density and μ for dynamic viscosity.

Pressure different between inlet settling section and the test-section inlet ($Pss - Pts$) record as free stream velocity. Assuming the fluid have constant pressure difference relative to time, inviscid and incompressible when passing through a wind tunnel, the speed in the test section can be calculated using a mass conservation's law,

$$A_{ss} U_{ss} = A_{ts} U_{ts}$$

Equation 9

The fluid movement inside the wind tunnel govern with equation 8 and Bernoulli equation

$$\frac{1}{2}\rho U^2{}_{ts} + P_{ts} = \frac{1}{2}\rho U^2{}_{ss} + P_{ss}$$

Equation 10

The dynamic pressure of the freestream flow ($q\infty$) was calculated using,

$$q_\infty = \frac{P_{ss} - P_{ts}}{1 - \left(\frac{A_{ts}}{A_{ss}}\right)^2}$$

Equation 11

Velocity in the test section become,

$$U_{ts} = \sqrt{\frac{2(P_{ss} - P_{ts})}{\rho_{amb}\left(1 - \left(\frac{A_{ts}}{A_{ss}}\right)^2\right)}}$$

Equation 12

The fluid density input manually on Labview panel. This value calculated from,

$$\rho = \rho_0 \frac{T_0}{T}\frac{p}{p_0}$$

Equation 13

ρ_0 = 1.293 kg/m^3

T_0 = 273.15 K

p_0 = 101325 Pa

ρ for density, T for room temperature and p for barometric pressure.

Dynamic and kinematic viscousity input into LabView panel and the values corrected by temperature by employee Shutterland Correction.

5.2 Experimental Technique

Accurate measurements of low Reynolds number airfoil performance is the key to understand and improve the efficiency of small Reynolds number systems. Most aerodynamic performance measurement techniques for airfoils rely on using balance systems or pressure systems, or a combination of both.

The difficulties with low Reynolds aerofoil experiments are mainly attributed to the sensitivity of laminar boundary layer to external factors such as free stream turbulence level, acoustic excitation, and surface finish. For most experiments, the dominant environmental factors are free to stream turbulence level. Post-stall behaviour are affected by free stream turbulence level as well.

Airfoil surface finishing has historically been a significant source of experimental uncertainty. With modern computer-guided manufacturing techniques, however, these defects are becoming negligible. Concerning surface roughness, Traub (Traub, 2013) concluded that a finish equivalent to 400 grit sandpaper or higher could be considered aerodynamically smooth.

On close examination of the wind tunnel test data below the 1000000 range of Reynolds number using models with the same aerofoil sections, it is possible to observe that there are some inconsistencies among the test results. This evidence can be attributed to a variety of causes including inaccurate measurement techniques, or due to solid and wake blockage effects, and differences between test environments (Mueller, 1982).

Figure 36. Setting Model in the Test Section

Pressure, velocity, incidence angle and force measurements are accurate to 1 per cent. Wind tunnel blockage ratio does not exceed 1 per cent.

5.2.1 Model Set Up

For the current test, the wing model mount vertically in the test section. Wing model connects to the external balance as the forces measurement system on the ceiling of the wind tunnel through the stainless steel rod that passed through the wing-rod fixture and were anchored 4 set bolts. At this side, the airfoil model was free to rotate about the centre of the steel rod. The geometrical angle of attack of the model measured using precision potensio meter.

Plexiglass (3/8 in) will be used as splitter plates to isolate the ends of the model from the tunnel side-wall boundary layers and the support hardware. The gap between the model and the splitter plates lower than 2 mm (0.005 model span) so that the model can move freely about its turnion point. The width of the splitter plates will be one chord upstream the model section and two chords downstream the model. The front face of the splitter plates has a leading edge shaped, and the trailing edge shaped glued on the back face of the splitter plates to maintain the flow around the model remain uniform. This plates will screw to the tunnel walls. A small plate used to assure the position of the plates in the test section were correct (Figure 36). For the 2d model, the splitter plate fix at both ends of the model since the flow pass through the entire span should be kept homogenous while for 3d model the splitter plate only fixes in one side.

Figure 37. Setting 2d model in the test section

There is a gap between the wing rod sting and the splitter plate to assure that the splitter plate will not touch wing rod steel during the measurement since oscillates might happen on the wing model, especially near stall and post stall.

5.2.2 Data Acquisition and Data Processing

During the experiment, the incidence angle at which the model was facing the air flow will vary. This parameter could have been adjusted from the control unit. To control the airspeed within the testing section, the adjustment of the generator’s rotational speed

(RPM) takes place in the control unit, and then the signal is sent to the generator. The air flow velocity is measured inside the testing section sends the value to the data acquisition unit which converts the signal to the digital one and passes on to the computer where the person experimenting can see the numerical value. Similarly, the incidence angle can be adjusted on a control unit, and the actual angle will appear on the computer screen. A pressure sensor measures air pressure upstream the testing section and, seen as the dynamic pressure. Varying incidence angle and the air flow velocity alters the force exerted on the specimen. The force is transferred to the overhead force balance beam via the attaching rod. The force is then split up into two components as the axial and the normal forces, and corresponding values are then sent to the DAQ system and the computer. The LabView software then writes all the measured parameters to the excel sheet once the data writing button is activated.

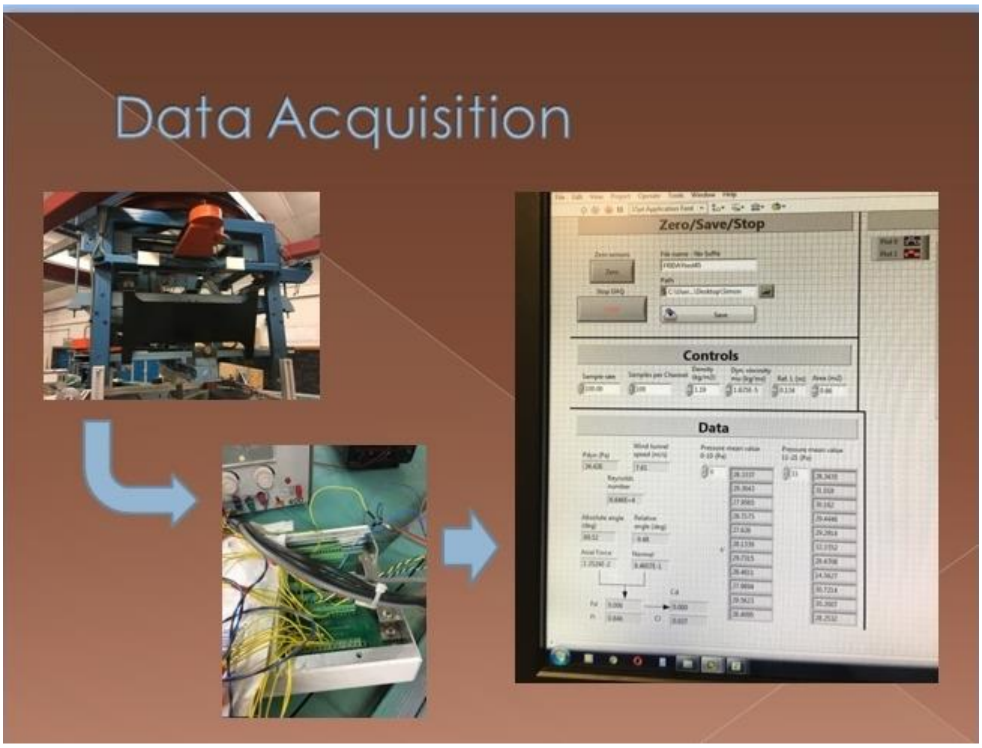

Figure 38. Data acquisition and data analyzing display

5.3 Force Measurement

In the current experiment, the force measurement uses the six components balance which placed on the top wall of the test section.

Before rundown the experiment, some load check is done to find out the reaction vector of the load measurement and the accuracy of the balance reading. The weights employee to the balance system for this step based on the predicted load will be experienced by the model in the main experiment. Lift and drag coefficient for each Reynolds number calculated by using XFOIL software based on the viscosity of the fluid is 1.789 x 10^{-5} gave maximum lift load 3.59 N and minimum drag 0.055 N.

The sting will be used to transfer the load from the balances to the external balance on the top of the test section. One end of the sting anchored to external balances system with four bolt and nut. A string will be attached to the hook at the other end of the sting. This string will be support by the pulley so that the scales can be hung on the other end of the string freely. A simple rigid frame built up to place the pulley. The loading processed were done gradually from the smallest scale. The process repeats for three times to define data quality from this load check. Especially for the fourth measurement, loading process was done gradually from the most substantial and reduced until zero. The result present in the form of a curve between load and balance reading.

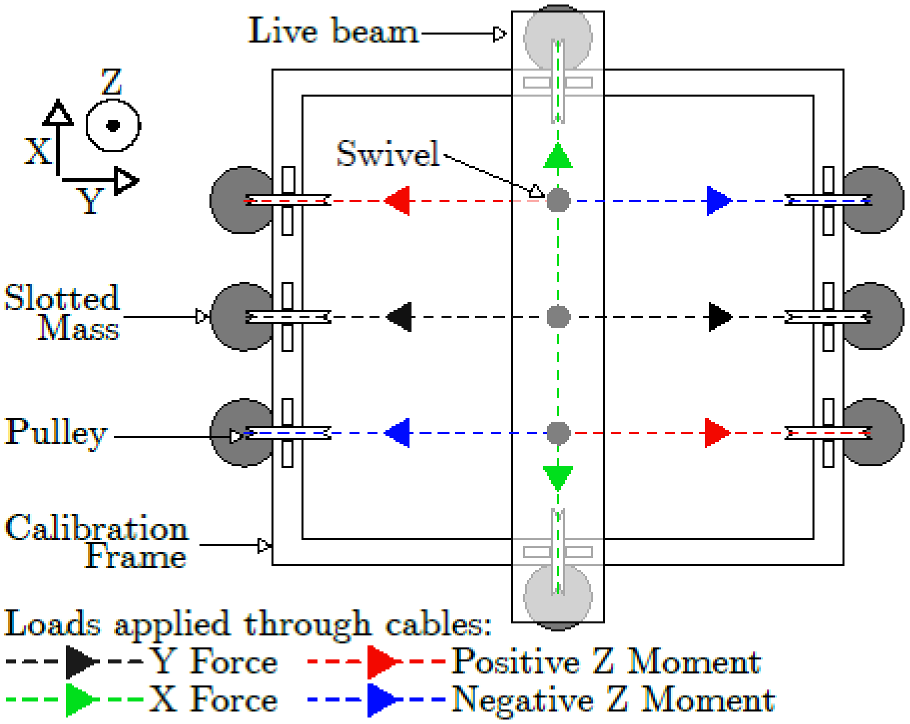

Figure 39. A Diagramatic Representation of The force of Balance Check Load Frame

The result shows that the value of the tangential force will be positive during the direction of the load opposite the wind stream. Meanwhile, the normal force amount will be positive when the direction of the load to the port side of the test section.

The results show good repeatability in most loading values except for a small region near zero. While the process changed from raising the load to reduce the weight, the result still shows the same trends. However, the reading values are not quite the same as the load itself, yet we can apply this data as the reading correction.

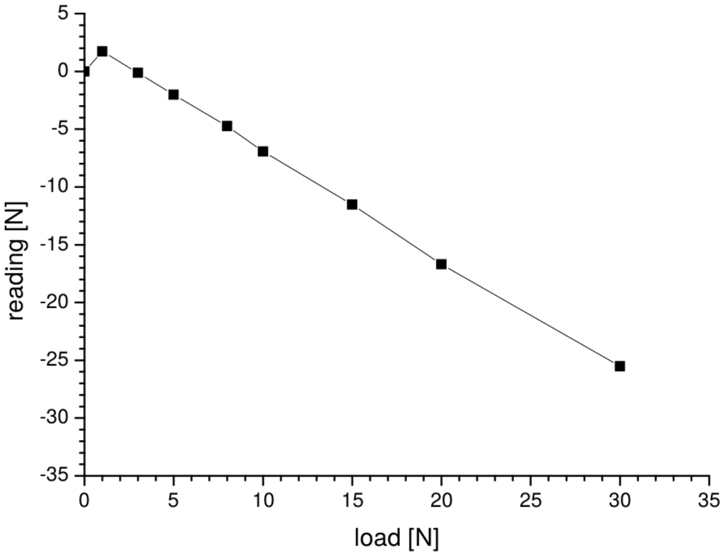

Figure 40. Normal Force (Fy) Check Load Results

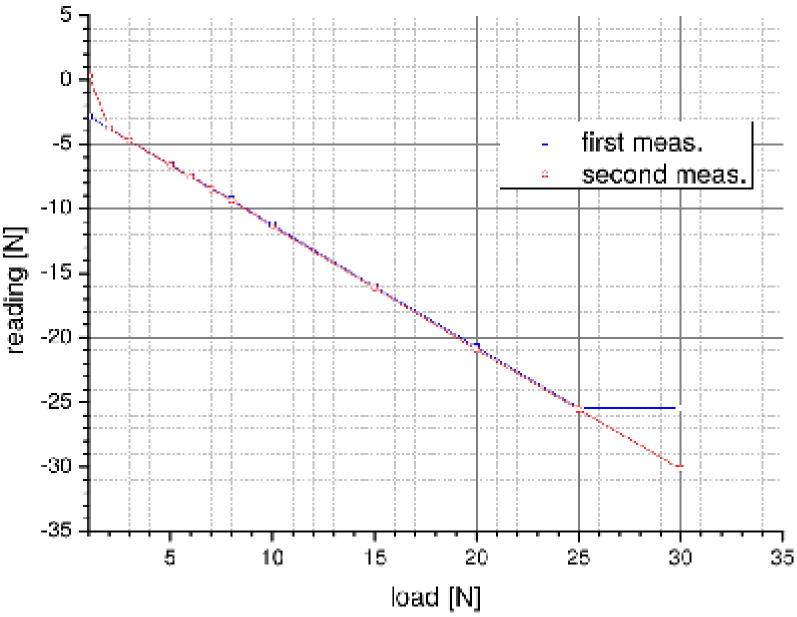

Figure 41. Tangential Force (Fx) Check Load Results

Series of measurements in the project tunnel test section has been planned to gain complete data for study the flow mechanism around both models with and without riblet.

Table 3. Force Measurement Test Matrices

Run	Model	Reynolds num.	Incicence [deg]	2D/3D	SR	Comment
FORCE MEASUREMENT						
001	Smooth	80000	-10 (2) 12	2D	10	
002		80000	-10 (2) 12	2D	10	Repeatability
003		80000	-10 (2) 12	2D	10	
004		80000	12 (2) -10	2D	10	Find histerysis
005		100000	-10 (2) 12	2D	10	Compare to ref.
006		80000	-10 (2) 12	3D	10	
007		80000	-10 (2) 12	3D	10	
008		80000	-10 (2) 12	3D	10	
009		80000	12 (2) -10	3D	10	
010	Riblet On	80000	-10 (2) 14	2D	10	
011		80000	-10 (2) 14	2D	10	Repeatability
012		80000	-10 (2) 14	2D	10	Repeatability
013		80000	-10 (2) 60	3D	10	
014		80000	-10 (2) 60	3D	10	Repeatability
015		80000	-10 (2) 60	3D	10	Repeatability

Since the external balance reading only normal and streamwise force reaction from the model, coefficient lift and drag derived using these formulas :

$$L = F_y cos\alpha - F_x sin\alpha$$ **Equation 14**

$$D = F_y sin\alpha + F_x cos\alpha$$ **Equation 15**

$$C_L = \frac{L}{qS}$$ **Equation 16**

$$C_D = \frac{D}{qS}$$ **Equation 17**

$$q = 0.5\rho U_\infty^2$$ **Equation 18**

L for lift, D for drag, Fy for normal force, Fx for tangential force, α for incidence angle between the model chord and wind direction, S for a surface area of the model, q for dynamic pressure, ρ for free stream density, U_∞ for free stream velocity in the test section.

5.4 Flow Visualization

Fluorescent oil surface-flow visualization was also used in order to identify separation bubbles and other flow features of interest. When performing this qualitative experimental method, the shear forces experienced at the surface of the wing model during tunnel operation cause oil on the surface of the model to move and create a time averaged pattern of the surface flow.

For this experiment, some clay powder dissolves in a paraffin solvent and then pour onto the surface of the wing. The wing model was rotated to the desired angle of attack and the wind tunnel was run at the desired Reynolds number for approximately three minutes. Black lights were used to excite the fluorescent dye in the oil, and all other sources of light were eliminated. The resulting flow patterns were documented using a Nikon D3100 digital camera with long exposure settings. Flow visualization was conducted for each wing at the design lift coefficient. Force measurement result will be used as a basis for determining the model position in this flow visualisation test.

The separation line will be shown clearly, mechanism of the stall and the bubble separation which might will occur on the experiment. The result from the flow visualisation test matrices in table 4 will be used to analyse the force measurement result of the model.

Table 4. Flow Visualization Test Matrices

Run	Model	Reynolds number	Incicence [deg]	2D/3D	SR	Comment
Flow Visualization						
f001	Baseline	80000	0	2D	10	
f002		80000	3	2D	10	
f003		80000	9	2D	10	Post stall
f004		80000	0	3D	10	
f005		80000	3	3D	10	
f006		80000	beyond α_{stall}	3D	10	Post stall

5.5. Wake Measurement

5.5.1 Wake Rake Design and Calibration

The geometry of the ideal rake configuration is such that its pressure coefficient will be zero at all Mach numbers and disturb the airflow as little as possible (that is, minimum frontal area). Because such a design is impossible in practice, a configuration with a minimum pressure coefficient is desired, and the rake geometry should be such that the rate of change of pressure coefficient with Mach number is small. To design rakes having a minimum error and also to predict the magnitude of errors to be expected, there are five parameters to be considered according to Krause's proposal (Krause, 1951). Those parameter are; (1) the distance from the static orifices to the leading edge of the static pressure tube (2) the distance from the static orifices to the support, (3) the distance between adjacent and static pressure tubes, (4) the distance from the static orifices to the leading edge of the adjacent tubes, and (5) the ratio of support diameter to jet diameter.

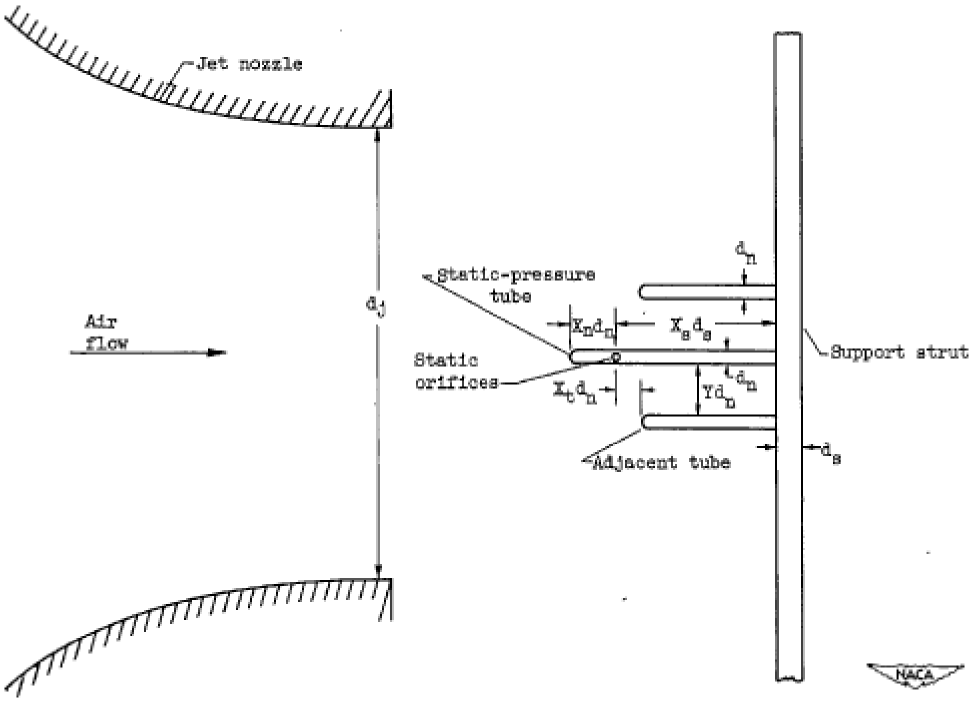

Figure 42. Diameter rule for pressure arrangement

The detailed geometry of the wake rake will be limited by test section area, the maximum thickness of the model, the width of trailing edge of model and Reynolds number of the orifice according to its inner diameter.

The objective of the design of the wake rake is to capture the inner structure of the boundary layer and to measure the width of the wake behind the model accurately. For this reason, the inner diameter of the orifice should not be bigger than the thickness of the trailing edge, and the length of the rake should be bigger than the maximum thickness of the model but isolated from the wall interference effect.

The detailed design of the wake rake use in this experiment shown in figure 42.

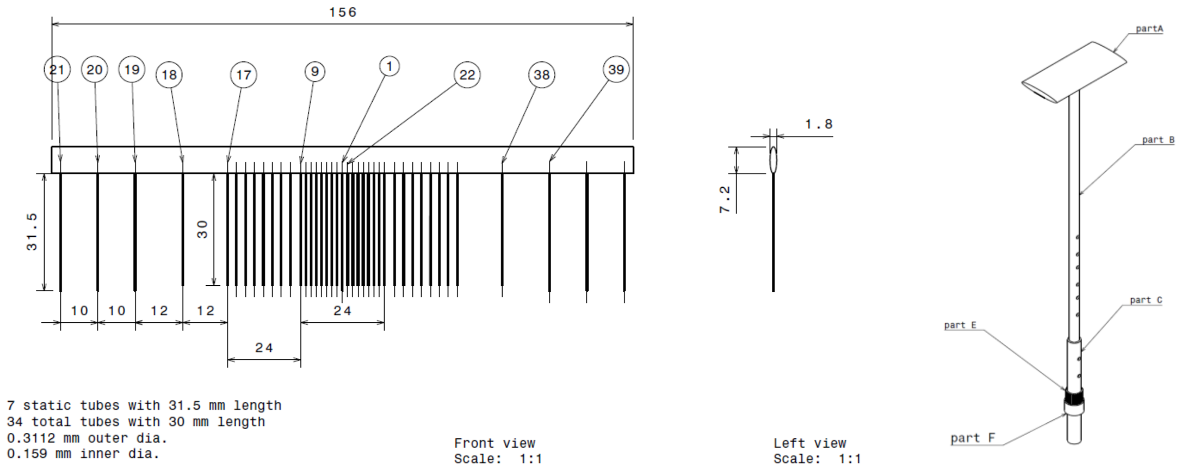

Figure 43. Wake rake detail design

The calibration process of this wake rake held in the empty test section. Since the measurement will be done for some incidence angle to the free stream velocity, this condition also accommodates in calibration process instead of varying the speed. The result of this measurement kept for correcting the data from the main experimental with the model.

For all pressure measurement, we have to define how long should we wait before the fluid fully develop and ready to save. The position of the instrument related to the model also has to be a parallelogram. To have statistically ergodic measurements and to account for the time lags due to the tubing system, recording of the total and static pressures were made when the pressures indicated by the digital manometer approached an asymptotic value. From the measurement result the statistical ergodicity of the flow is obtained by acquiring data for a minimum time of 10 seconds.

Since the pressure rake only measured total pressures, a seven-hole probe described in the next section was used to measure the static pressure at a location in the boundary layer under the assumption that the static pressure stayed constant in the boundary layer.

5.5.2 Seven Hole Probe Calibration and Measurement Technique

Previous experiments have shown that the azimuthal velocity occurs in the wake downstream of yawed riblets also reduction in turbulence intensity. The seven-hole probe uses to capture these phenomena since it is susceptible to angular velocity.

In-situ calibration of the seven hole probe was performed in accordance with the process outlined by Zilliac (1989). Here, a non-nulling technique was used to calibrate the probe about the tunnel axis to establish a correlation between the directional pressure coefficients and the flow angles and total and dynamic pressure coefficients. This was done by placing the probe in a known, axial flow, and moving the probe to a number of known angles. The independent variables (directional pressure coefficients) could then be related to the dependent variables (flow angles and total and dynamic pressure coefficients).

Figure 44. Seven hole coned probe

Multi-variable polynomial curve fit employed to relate the independent and dependent variables collected from the calibration. However, the number of points that are used to calibrate a sector is a very important factor in determining the appropriate order to fit. The calibration grids were uniform in cone and roll. The grids were a function of two parameters – grid spacing and maximum cone angle. Grids were generated by moving through cone angles from 0° to the defined maximum, stepping in the specified increment. At each cone angle, the roll angle was varied from 0° to 360°, again stepping in the specified increment. Each pair of cone and roll angles were converted to a pitch and yaw angle. Resolution error due to the traverse's limited resolution was mitigated by converting the desired pitch and yaw angles to a number of steps, rounding that number of steps to the nearest whole number, and finally outputting the resulting pitch and yaw angle, which was necessarily an exact multiple of the traverse's smallest step size. All the government equations used to analyze data were describe in Appendix B.

.Silicon tubing was used to connect the stainless pressure tubes on the probe side to the pressure transducers. The tubing was connected to the probe, and compressed air was then used to blow any condensation out of the lines. An eighth pressure line was connected to the static pressure ports on the pitot static tube so that reference static pressure data could be collected. Once the probe and the static tube were connected to the pressure transducers, the pressure transducers were read, and the reported pressures were taken to be zero offsets for the transducers. All subsequent measurements were corrected by that amount.

Instrumentation was connected to the PC using Data Translation Inc DT3003-PGL DAQ boards and DT730-T terminal blocks. These DAQ cards were capable of accepting 32 differential analog inputs, each with 12 bit resolution. Unused channels were grounded when they were not in use to reduce noise and cross-talk.

The wind tunnel was run for at least 10 minutes before data was collected. This ensured that transient startup effects, including the mild aerodynamic heating of internal components, did not affect the flow. The probe was held in position for 1.5 seconds to allow the damping of transient pressure effects as well as mechanical vibration caused by the motion of the traverse. The 7 pressure ports and reference static pressure measurement were then measured simultaneously at 900 Hz for a period of 1 second. The pitch and yaw angles, and the 8 pressures were then written to a text file. The traverse then moved to the next calibration point, and the process was repeated.

The appropriate sampling period was determined by taking transient pressure data at 900 Hz, the maximum sampling rate of the data acquisition system, and measuring the response of the seven pressures to a significant change in flow angle. The seven transient pressure profiles plot and a settling time were determined qualitatively. The settling time is the length of time that is allowed after the probe moves, but before sampling is started. The sampling period determines by plotting the change in the moving average of the seven pressures. This plot shows in Figure 45.

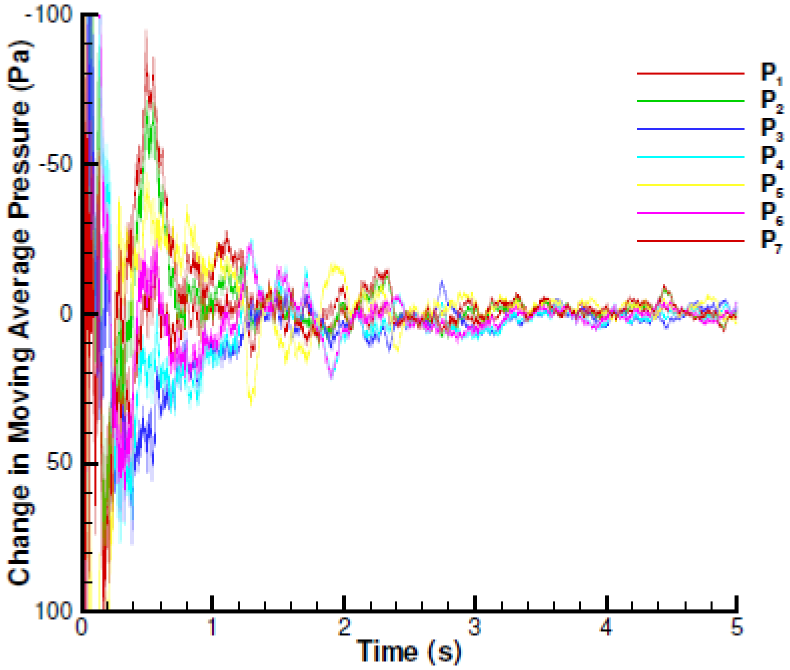

Figure 45. Transient Pressure Response to a 30 degree Change in Flow Angle

The plot shows that the most significant peaks and fluctuations have ended by 1.5 seconds. A sampling period of 1 second was chosen because the change in moving average has decreased to less than 0.005% per additional sample by this time.

The calibration coefficient, post processing of measurement data, and error analysis presented in Appendix B.

5.5.3 Wake Survey Method

This measurement aims to find out the effect of herringbone riblets in the wake downstream the 2d model S1223 at low Reynolds number. Wake rake and seven-hole probe installed to define the local parameter of the flow. There are three different positions on the spanwise direction of the riblets will be measured as shown in Figure 45. P_1 is the divergent riblet shaft, and P_2 is the gap between riblets. The wake parameter between P_1 and P_2 measured to define the condition between both patterns.

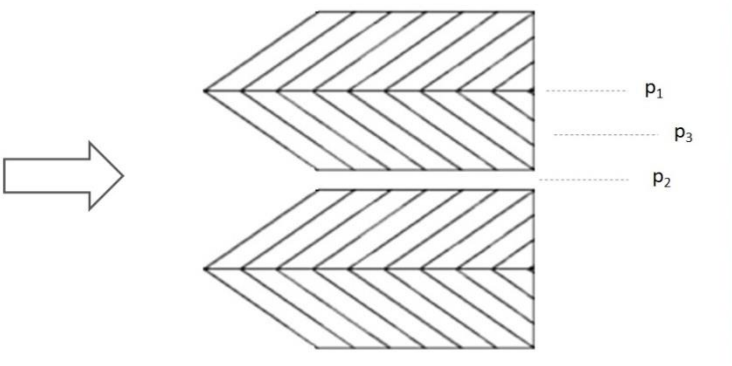

Figure 46. Measurement points downstream of the model. Arrow show flow direction. P_1 - divergent riblet shaft. P_2 – gap between riblet. P_3 – middle area between P_1 and P_2

Table 5. Wake Measurement Test Matrices

Run	Model	Reynolds num.	Incidence [deg]	2D/3D	SR	Comment
WAKE RAKE MEASUREMENT						
w001	Smooth and Riblet on	80000	0, 3, 9	2D		Each of this condition apply for 3 point shows in Figure 44
w002		80000	0, 3, 9	2D		
w003		8000	0, 3, 9	2D		

The wake survey system consisted of a wake rake and a seven hole probe. A total of 34 total pressure probes and 7 static pressure probes, each having an outer diameter of 0.3112-mm, were aligned horizontally along the rake. The wake rake was suspended from the ceiling of the test section using a support structure in order to acquire the total pressure profile of the airfoil wake downstream of the vertically-oriented airfoil. The wake rake was traversed across a plane approximately 1.2 chord lengths downstream of the trailing edge of the airfoil model in the horizontal (chord-normal) direction until the tails of the wake profile were sufficiently captured. This process was measured to determine the position of the wake tails by comparing the gradient of the total pressure deficit at multiple locations along the span of the wake profile.

The total pressure probes in the wake rake were connected to pressure transducers ±0.35 psid (±10.0 in. WC). Each of pressure transducer has 2 legs that one leg connected to tubes of wake rake and the other one connected to static pressure reference tunnel. They measured the difference between the pressure of tube's rake and the test section static pressure ($Ps,i - Pts$). As a result, the pressure coefficient (Cp,i) of a given location on the tube's rake could be calculated by dividing the measured differential pressure (Ps,i – Pts) by the dynamic pressure (q∞), Eq 11.

$$C_{p,i} = \frac{P_{s,i} - P_{ts}}{q_{\infty}}$$

Equation 19

The standard momentum deficit method described by Jones and Schlichting was used to calculate the drag of the airfoil. The method involves a control volume analysis around the body, assumes steady, two-dimensional flow and uniform freestream. The outflow plane of the control surface is placed sufficiently far downstream from the airfoil where the static pressure in the wake (Pw) is equal to the freestream static pressure (P∞). Due to viscous effects however, the total pressure in the wake is expected to be lower than the freestream total pressure and this pressure loss can be attributed to the wake velocity deficit. Using the equation of conservation of momentum in the integral form, the drag at a given spanwise section of the airfoil model can be calculated using,

$$D' = \rho \int u_w (U_{\infty} - u_w) dy$$

Equation 20

Since the flow is incompressible (i.e. $M\infty \leq 0.3$), the total pressure across the freestream plane and the w-plane can be expressed using Eq. 21 and Eq. 22 respectively.

$$P_{\infty} + \frac{1}{2}\rho U_{\infty}{}^{2} = P_{0,\infty}$$

Equation 21

$$P_w = P_{\infty} + \frac{1}{2}\rho u_w{}^{2} = P_{0,w}$$

Equation 22

$$D' = 2\int \sqrt{P_{0,w} - P_{\infty}} \left(\sqrt{P_{0,\infty} - P_{\infty}} - \sqrt{P_{0,w} - P_{\infty}}\right) dy$$

Equation 23

Equations 21 and 22 can be combined to express the dynamic pressure at the wake plane in terms of the wake total pressure, freestream total pressure and the freestream dynamic pressure:

$$q_w = q_\infty - \left(P_{0,\infty} - P_{0,w}\right)$$

Equation 24

An expression for the sectional drag of the airfoil in terms of the wake total pressure deficit can be obtained using Eq. 23 and Eq. 24.

$$D' = 2\int \sqrt{q_\infty - \left(P_{0,\infty} - P_{0,w}\right)}\left(\sqrt{q_\infty} - \sqrt{q_\infty - \left(P_{0,\infty} - P_{0,w}\right)}\right) dy$$

Equation 25

The expression in Eq. 25 allows an accurate estimate of the sectional drag to be obtained in the wake surveys by directly measuring the difference between the freestream total pressure and the wake total pressure. This method was used since it did not require the freestream total pressure to be directly measured. These pressure transducers used for acquiring the wake pressures were referenced to a stable atmospheric pressure reference in the control room in order to achieve greater repeatability of the drag measurements. As a result, instead of directly measuring ($P_{0,\infty}$ – $P_{0,w}$), it was calculated by,

$$P_{0,\infty} - P_{0,w} = \left(P_{0,\infty} - P_{atm}\right) - \left(P_{0,w} - P_{atm}\right)$$

Equation 26

where the gauge pressure measurements of the wake total pressure, ($P0,w$ – $Patm$), were obtained in the wake of the airfoil and the gauge pressure measurements of the freestream total pressure, ($P0,\infty$ – $Patm$), were obtained outside the wake of the airfoil.

Substituting the pressure difference ($P0,\infty$ – $P0,w$) given by Eq. 26, along with $q\infty$, in Eq. 25 yielded an expression for the sectional drag of the airfoil. A numerical integration using the trapezoid method was used to solve Eq. 25. Thus, the sectional drag of the airfoil could be calculated using,

$$D' = \sum_{i=1}^{n_{rake}-1} \left[\sqrt{q_{\infty} - \left(P_{0,\infty} - P_{0,w_i}\right)} \left(\sqrt{q_{\infty}} - \sqrt{q_{\infty} - \left(P_{0,\infty} - P_{0,w_i}\right)} \right) + \sqrt{q_{\infty} - \left(P_{0,\infty} - P_{0,w_{i+1}}\right)} \left(\sqrt{q_{\infty}} - \sqrt{q_{\infty} - \left(P_{0,\infty} - P_{0,w_{i+1}}\right)} \right) \right] \left(y_i - y_{i+1}\right)$$

Equation 27

where $nrake$ represents the total number of probes that were used to measure the wake. As a result of spanwise variations of the flow due to imperfections in the model, the sectional drag of the airfoil was averaged over multiple spanwise stations to provide a spanwise invariant estimate of the sectional drag that would be characteristic of a true airfoil model of infinite span. The drag coefficient of the airfoil model was calculated from the sectional drag using,

$$C_D = \frac{D'}{q_{\infty} c}$$

Equation 28

5.6. Data Correction

In a closed test section, the presence of walls influences the flow around the model. The magnitude of wall effects on experimental data scales with blockage ratio (Pope, 1966). Model blockage ratio (B) is defined as the ratio of the model projected area to the cross-sectional area of the test section. Understanding the effects of blockage and methods to avoid them or correct the experimental data is of extreme importance in experimental fluid mechanics. The three most common types of blockage are solid blockage, wake blockage, and longitudinal (or horizontal) buoyancy (Tavoularis, 2005).

The presence of a model effectively reduces the cross-sectional area of the test section and thus causes solid blockage effects. This reduction leads to, via continuity, in a local flow acceleration around the airfoil that are functions of model thickness and angle of attack. A simpler form for the solid-blockage correction for 2D tunnels has been given by Thom (Pope, 1965). Thom's solid blockage correction is

$$\varepsilon_s = \frac{\mathrm{K}_1 \tau_1 (model\ volume)}{(wH)^{\frac{3}{2}}}$$

Equation 29

is used to correct for these velocity increases. In the above equation, K_1 and τ_1 could be estimated from Figure 38 and 39 related to the geometry of the model and test section. K_1 is a constant parameter based on the airfoil configuration ($K_1 = 0.52$ for airfoil models spanning the height of the test-section), C is the empty test-section area, and V_m is the volume of the airfoil model. In the current study, the exact value of the airfoil model volume was obtained from CAD model, however, if such data is not available the model volume can be estimated using,

$$V_m = \frac{3}{4} tcb$$

Equation 30

The volume of 2D model and 3D model are 0.001089 m^3 and 0.00029 m^3. According to equation 8, the solid blockage of 2D and 3D model are 0.000914 and 0.000219. Overall the data can be said to be accurate and reliable for the course of this project.

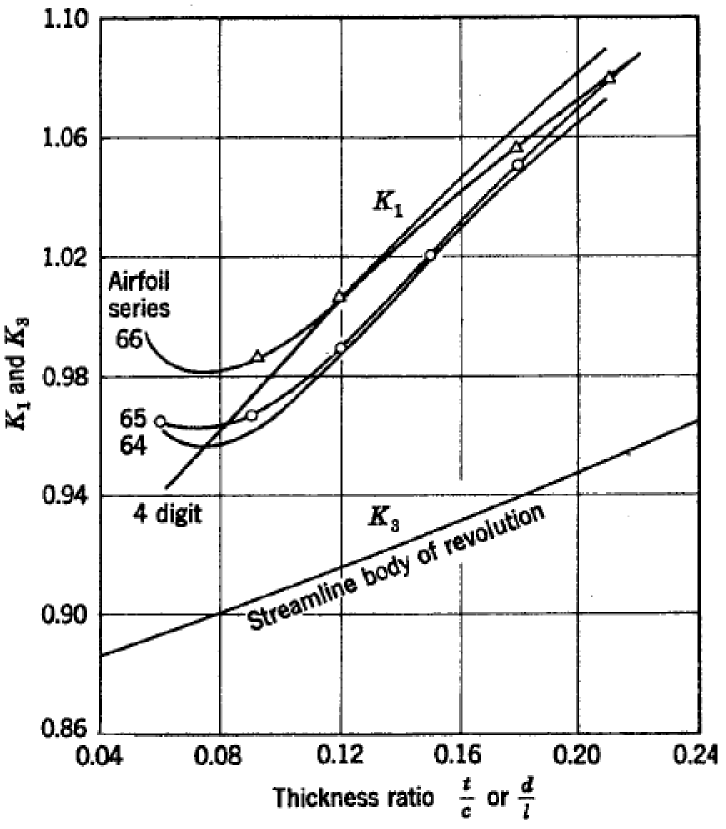

Figure 47. Values of K_1 and K_3 for a number of bodies (Pope, 1965)

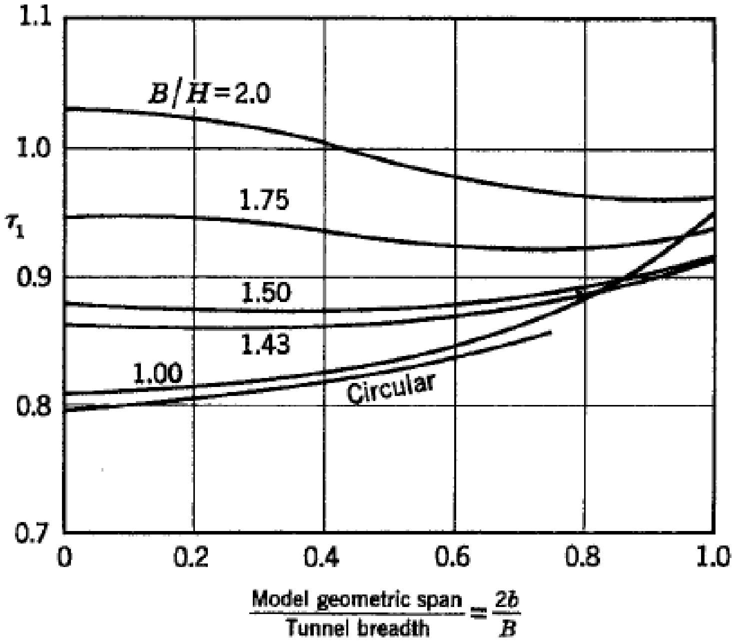

Figure 48. Values of τ_1 for a number of tunnel types. Use b/B = 0 for bodies of revolution (Pope, 1965)

Similar to the solid blockage effects, the wake blockage effects result in regions of local high velocities. In this instance, the velocity deficit associated with the wake of an airfoil results in an increase in velocity outside of the wake to ensure a constant mass flux across any given cross-section of the wind tunnel. Since the extent of velocity deficit in the wake is directly related to the profile drag of the airfoil, it can be empirically correlated to the profile drag. Thus, a wake blockage velocity increment factor, εwb, can be calculated using,

$$\varepsilon_{wb} = \frac{1}{2}\frac{c}{H}C_{d,u}$$

Equation 31

which can be used to determine the influence of the wake blockage effect. In the above equation, h is the height of the test-section and Cd,u is the uncorrected value of the airfoil drag coefficient obtained through wake survey methods as described in Section 2.4.2. The solid blockage correction factor and the wake blockage correction factor are added together (Eq. 2.35) to establish the net velocity increment, ε.

$$\varepsilon = \varepsilon_{sb} + \varepsilon_{wb}$$

Equation 32

Streamline curvature effects, which would otherwise be absent in an unbounded flow field, are introduced by the solid walls of the test section. The wind tunnel walls artificially impose an apparent camber of the airfoil, as streamlines cannot penetrate these solid boundaries. Therefore, the lift and the magnitude of the quarter-chord pitching moment are incrementally changed in comparison with the lift and moment values that would be obtained in an unbounded environment. An empirically derived variable σ, can be used to compensate for the streamline curvature effect. It is calculated using,

$$\sigma = \frac{\pi^2}{48}\left(\frac{c}{H}\right)^2$$

Equation 33

A set of empirically derived relations were used to calculate the correction factors in Eq. 19-23. The corrected airfoil angle of attack, lift coefficient, drag coefficient, quarter-chord pitching moment coefficient, and pressure coefficient, were corrected using Eqs. 24-28.

$$\alpha_{cor} = \alpha_u + \frac{57.3\sigma}{2\pi}\left(C_{L,u} + 4C_{M,u}\right)$$

Equation 34

$$C_{L,cor} = C_{L,u}(1 - \sigma - 2\varepsilon)$$

Equation 35

$$C_{D,cor} = C_{D,u}(1 - 3\varepsilon_{sb} - 2\varepsilon_{wb})$$

Equation 36

$$C_{M,cor} = C_{M,u}(1 - 2\varepsilon) + \frac{1}{4}\sigma C_{L,u}$$

Equation 37

$$C_{p.cor} = \frac{C_{p,u}}{(1 + \varepsilon)^2}$$

Equation 38

According to Eq. 29, solid blockage for the 2D wing model is

K_1	0.52	
H	1	m
W	1	m
t	0.0024	m
b	0.45	m
c	0.015	m
Solid blockage	**0.000914**	

and the solid blockage for the 3D wing model is 0.000219 since the volume of the 2D and 3D model respectly 0.001089 m^3 and 0.00029 m^3

5.7 The Uncertainty

The experimental results from this investigation were associated with certain uncertainties which are presented in this chapter. Analyzing the uncertainties of acquired measurements is important in assessing the significance of the scatter associated with experimental results over multiple trials37 and thus provide a more robust interpretation of the experimental results. As described by Kline and McClintock38 and Airy39, the uncertainty in a measurement is the “possible value that an error may have”. Two sources of error – bias and precision errors – that contribute to the uncertainties were evaluated in this study. Bias errors are typically associated with uncertainties in the measurement capabilities of the equipment or accuracy of the calibration. These errors are also referred to as “fixed” errors because they are accompanied with a consistent and repeatable offset. Precision errors, on the other hand, are classified as being “random”, since they behave randomly with zero mean. The sum of these two sources of error provided the best estimate of the measurement error.

The precision or uncertainty (UX) associated with a set of N observations of the variable (X) having a mean ($X(N)$) can be calculated using

$$\sqrt{\left(\frac{\partial q_\infty}{\partial(P_{ss}-P_{ts})}U_{(P_{ss}-P_{ts})}\right)^2}$$

Equation 39

where $S(N)$ is the standard deviation of the set of N observations used to calculate the mean value $X(N)$, and t is the Student’s t statistic determined by the desired confidence interval and the number of samples N. The variable (X) is assumed to follow a Gaussian distribution.

The reduced variable of an experiment (R) that is determined using several independently measured variables (xi) is represented by,

$$R = R(x_1, x_2, x_3, \dots\dots, x_n)$$

Equation 40

Since the separate measurements were acquired from different measurements, it is natural to assume that the uncertainties of each measured variable were independent from each other. Therefore, the “bias” or “fixed” uncertainty (UR) associated with the result is then calculated by taking the square root of the sum of the squares of the corresponding uncertainty components produced by each variable

$$U_R = \sqrt{\left(\frac{\partial R}{\partial x_1} U_{x_1}\right)^2 + \left(\frac{\partial R}{\partial x_2} U_{x_2}\right)^2 + \left(\frac{\partial R}{\partial x_3} U_{x_3}\right)^2 + \cdots + \left(\frac{\partial R}{\partial x_n} U_{x_n}\right)^2}$$

Equation 41

This method was used to calculate the "bias" uncertainties associated with the flow conditions, pressure and performance coefficients. A derivation of the equations used for these reduced variables was outlined in Section 5 and the detail will be described at Appendix D..

The value of uncertainty for each measurement show in the tables below.

Table 6. Uncertainty Values in This Measurements

Parameter	Reference Value	Absolute Uncertainties	Relative Uncertainties (%)
c	0.1583 mm	±0.005 mm	±0.0278
α	5 derajat	±0.02 derajat	±1.33
q_∞	120.5051 Pascal	±0.000771 Pa	±0.8026
P_{amb}	100458.4 Pascal	±0.008 Pa	±0.0556
T_{amb}	298.35 Kelvin	±1.8 Kelvin	±0.3404
ρ_{amb}	1.173662 kg/m3	$\pm 7.771\text{x}10^{-6}$	$\pm 7.771\text{x}10^{-6}$
μ_{amb}	$1.84 \text{ x } 10^{-4}$ Ns/m^2	$\pm 1.27\text{x}10^{-9}$	$\pm 1.270\text{x}10^{-9}$
U_∞	14.33 m/s	±0.01871	±0.1871
Re_c	100000	±5033	±0.5073
C_p	-2.8218	±0.056935	±2.0177
C_D	0.012603	±0.002393	±0.5212

6 Experiment Results and Discussion

6.1. Force Balance Test

Both two models with smooth and riblets surfaces was tested at Reynolds number 80000, giving 230 data points involving dynamic pressure, axial and normal to the planform forces, airspeed and incidence angle. Each point is the average of 1,000 measurements. After processing all the data, many graphs were created to observe the general trends of the flow performance for both smooth and riblets surfaces and to compare the two.

Figures 50) and 51) reveal the trends unrolled at Reynolds number 80000 for the bird wing model. First off, the graph in Figure 50) demonstrates that herringbone-type riblets can reduce the drag of the model in low incidence angle.

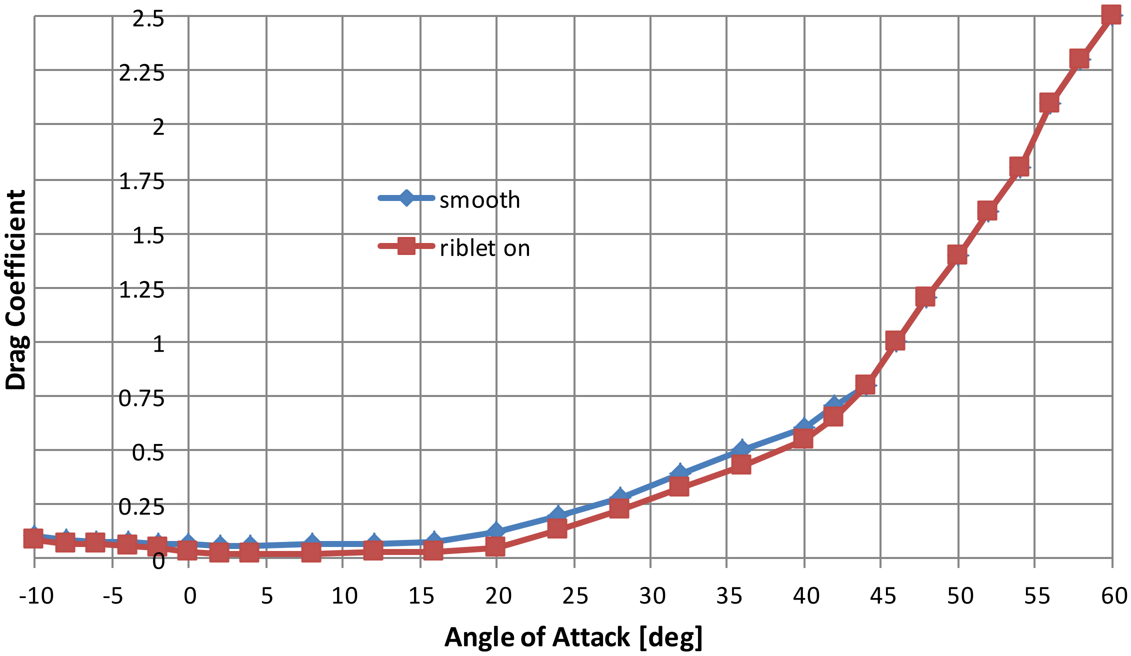

Figure 49 : Coefficient Drag of 3D Model with and Without Riblets

We can see that from incidence angle -10 degrees to 44 degrees, the drag reduce from 18% until 20%. Beyond 44 degrees the drag coefficient is getting closer to the smooth surface. At this point, the flow starts to separate from the surface of the model. The separation begins from the root part of the model and totally off the surface at the tip.

This mechanism shows clearly from the flow visualization of the smooth surface of the 3d model. However, the drag coefficient of the rough surface never more prominent than the smooth surface for this 3d model case.

The lift coefficient also shows some interesting phenomena between the smooth surface and riblets. The riblets significantly increase the lift coefficient of the model. The flow seems improved while passing over the riblets. However, a kink occurs on the curve at 12 degrees (Figure 51). This condition can discuss deeper after we see the result from the flow visualization and near wake measurement. The maximum increment of the lift coefficient of more than 56% occurs at incidence angle 8 degrees.

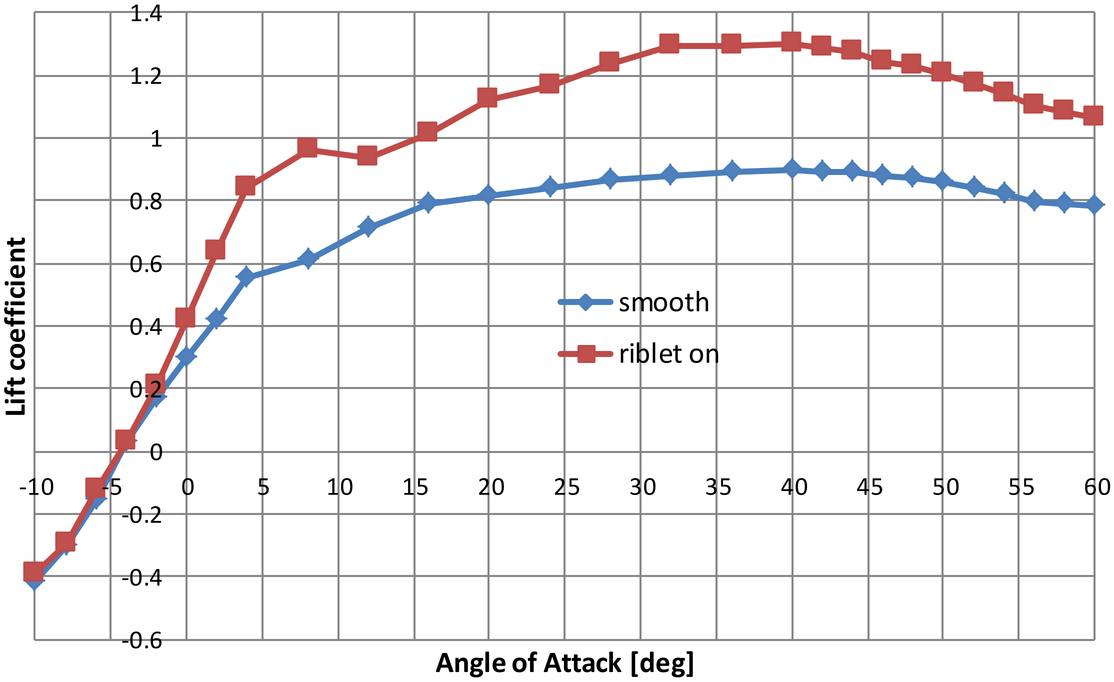

Figure 50 Lift Coefficient of the model with and without riblets

The unusual behaviour of the flow around the wing was captured in Figure 51). The stall angle of attack is seen to be at 8 degrees. However, the other peak at 40 degrees incidence angle is visible as well indicating the second stall angle. Conventional aircraft wing stalls only once due to their shape but the pigeon wing model at this low velocity seem to be stalling twice. It can be explained by the fact that the wing does not have a straight leading edge nor the trailing edge; furthermore, the surface of the wing is bumpy with local peaks and recesses making it stall at different locations at different incidence angles. It cannot be seen at a higher velocity because the flow detaches more rapidly.

The reduction in drag coefficient and the enhancement of the lift coefficient and also occurs in the 2D model. Figure 52 shows the effect of the riblet on drag and lift coefficient at each angle of attack. This value derived from the delta of each coefficient at each angle of attack normalized with the smooth condition value. Drag coefficient reduces 20% between 0 degree to 6 degrees. Outside of this region the drag coefficient of the riblet surface still more prominent than the smooth surface.

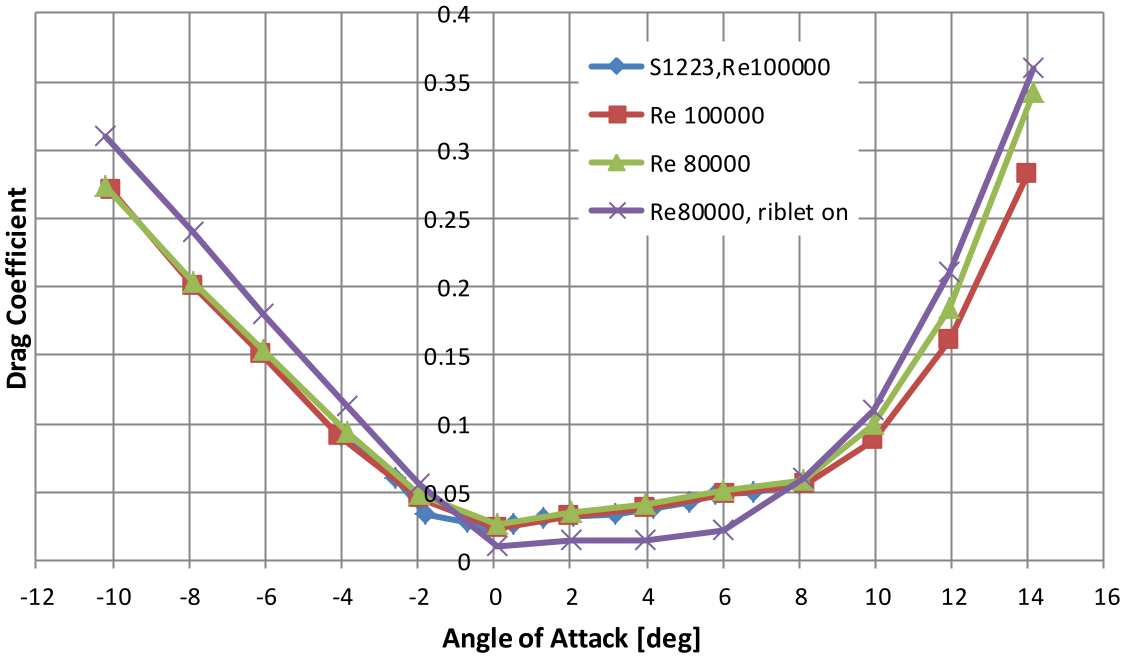

Figure 51. Coefficient Drag model 2d

Figure 50 shows that beyond 0 degrees the rough surface increases the lift coefficient. The maximum increment in lift coefficient of almost 20% at 8 degrees. Even if this value reduces after this point, however, the lift coefficient still much bigger than the value while the surface is smooth. Post-stall behaviour shows differences between smooth and riblet surface. The riblet could improve the post-stall condition even the enhancement value slightly reduce.

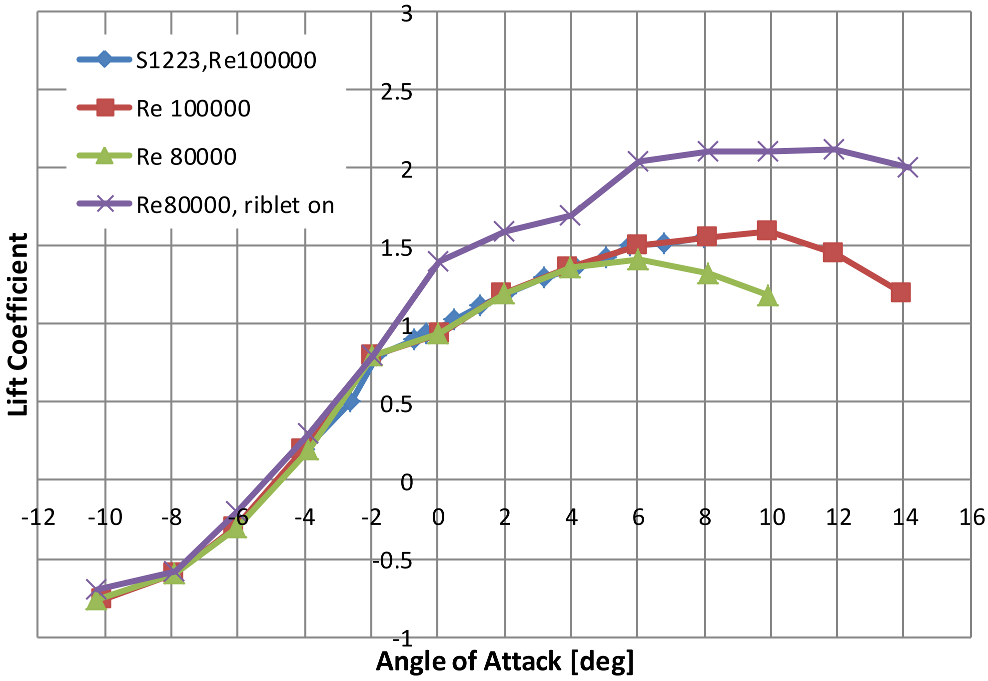

Figure 52. Coefficient Lift 2D Model

These results at some points agree with the theory of Nugroho et al. (2013) about herringbone-type riblets functioning as a drag reducing device by moderating the near-wall boundary layer might suggest that the same mechanism could also induce the lift by smoothening the flow over the riblets. The lift for this particular wing continues to increase after stepping out of the stalled trough and even tops the initial C_L seen just before the stall angle due to the shape of the model.

6.2 Flow Visualization

Figures from both models show the results from the primary oil flow test carried out at Reynolds number 80000 and three incidence angles. The incidence angles define from the results of force measurements. These data are taken to compare condition when the flow still attach to the surface, separation start and post stall condition.

Figure 51, 52 and 53 shows the mechanism of separation on the 3d model. Figure 51) shows the pattern of the flow on the 3d model when the incidence angle is 0 degree. The stream still attach to the model except for a small region close to the trailing edge of the root section.

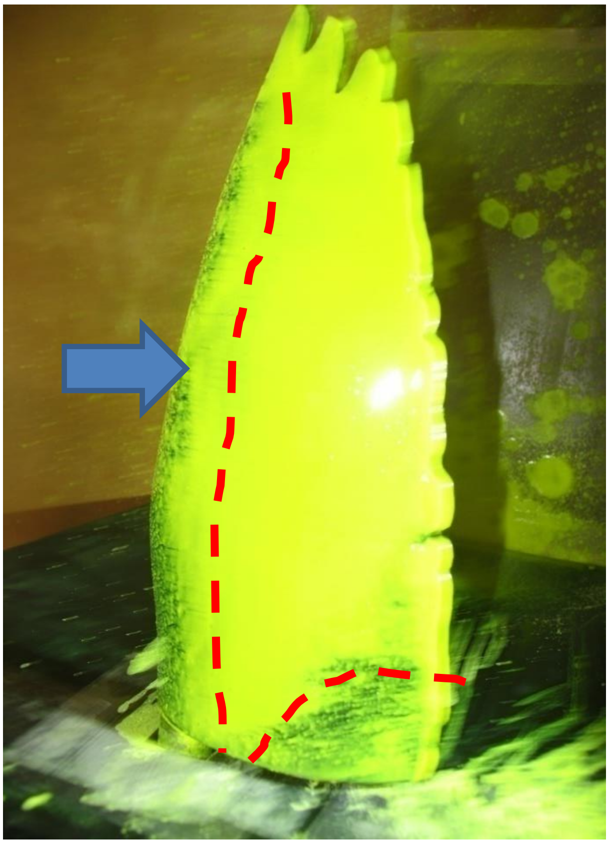

Figure 53 3d model at 0 degree incidence

While the incidence angle rise, this separation region start to invasion the 3d model start from the root section, at the root, the separation point toward to leading edge and to the tip (Figure 52).

At the post-stall condition we can found that the flow almost separate from the root section remind some area on the leading edge. However, the stream still attached from the leading edge until trailing edge at the region near the tip.

This mechanism natural to understands since the distribution of the thickness and chord from root to tip reduce in a unique pattern. The local incidence angle at the origin will be higher than on the tip.

Laminar separation bubble emerges at the centre of the model planform surface change the pattern of the flow around it. This laminar separation bubble occurs at the section where the thickness of the section quite thin compares to the root.

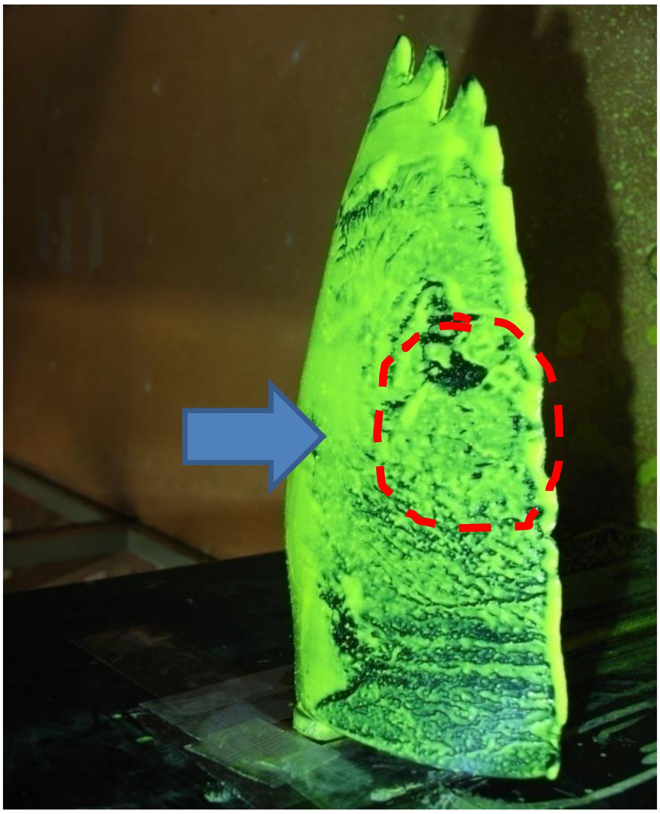

Figure 54 3d model at 14 degree incidence

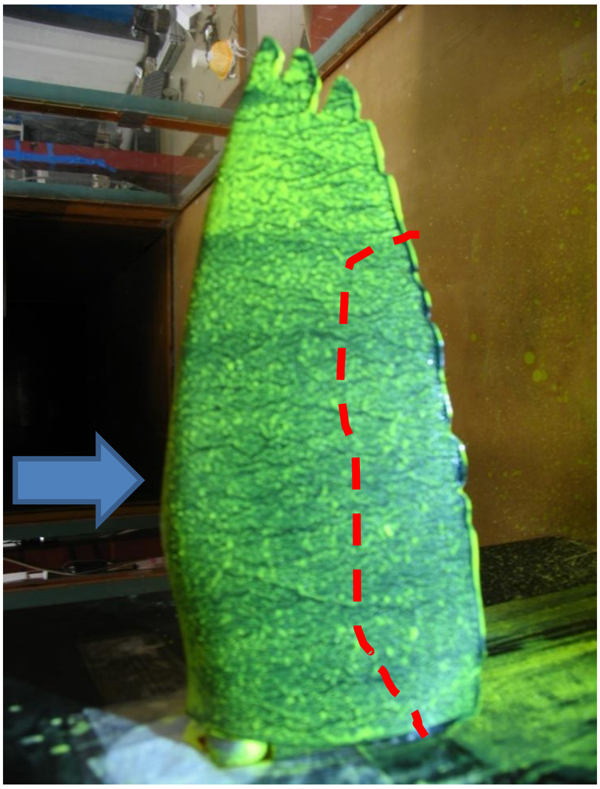

Figure 55 3d model at 36 degree incidence

Finally, the picture in Figure 53 shows the flow over the model at 9 degrees incidence angle, which, according to the C_L curve in Figured 48, labels the trough in the post-stall region. As both the picture and the graph suggest the flow is entirely separated; hence no visible distinctive features are present within the picture.

Figures below show the results from the 2d model. Those pictures will represent three conditions of the flow on the model; when the flow still attach to the surface, when separation start occurs and post stall condition according to the force measurement results and also from viscous computation with VLM method.

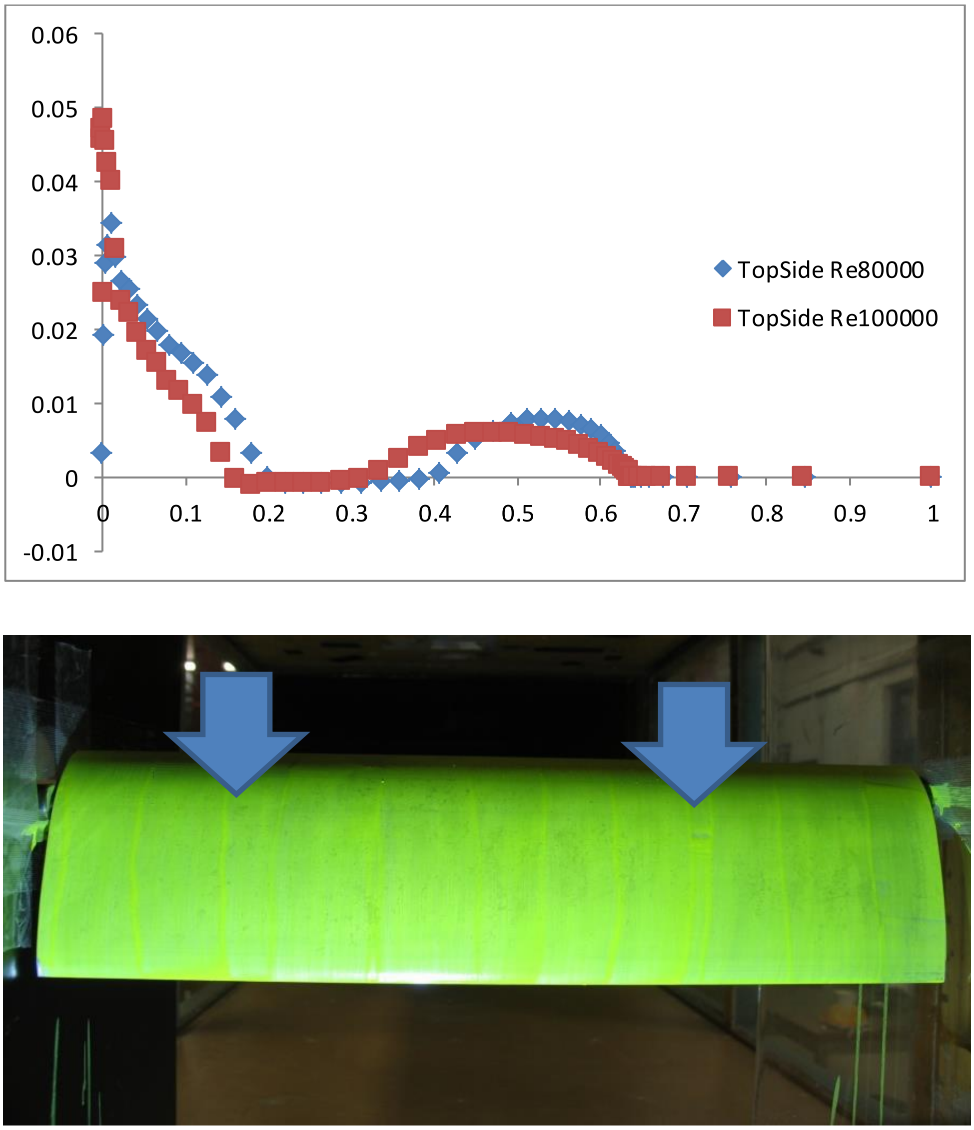

Figure 56. Upper Skin Friction at 0^{o} angle of attack and below is flow visualisasion result on 0 angle of attack

At zero degree angle of attack the skin friction goes zero from 20% until 30% of chord length which is also appear on the upper surface of the 2D model. The fluids attached again beyond 30% and fully separate after 63% (Fig. 56).

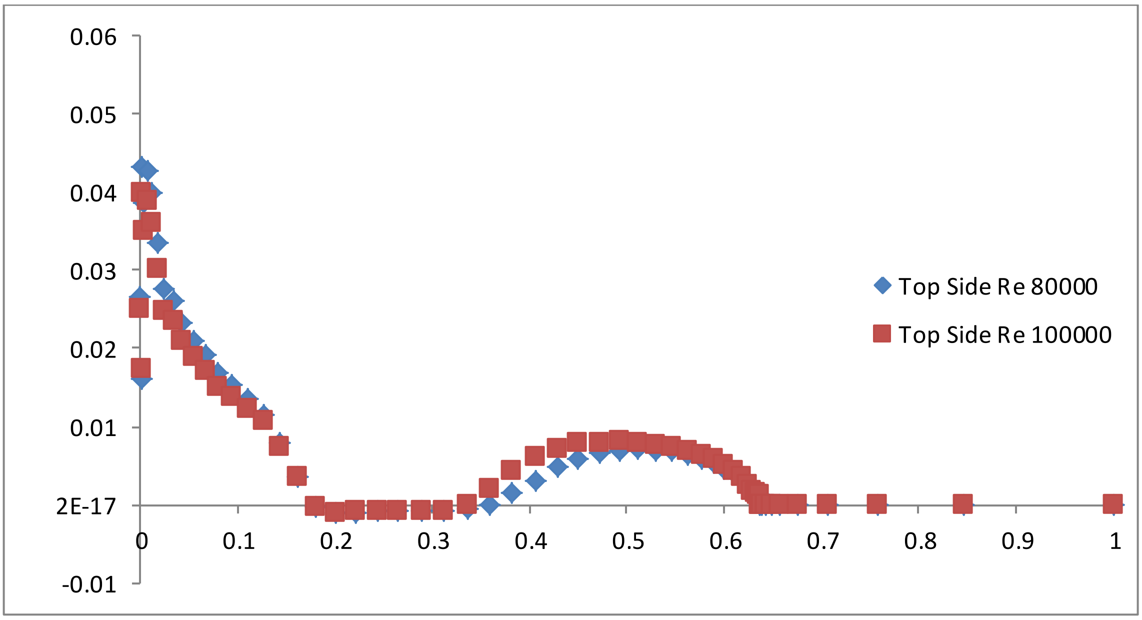

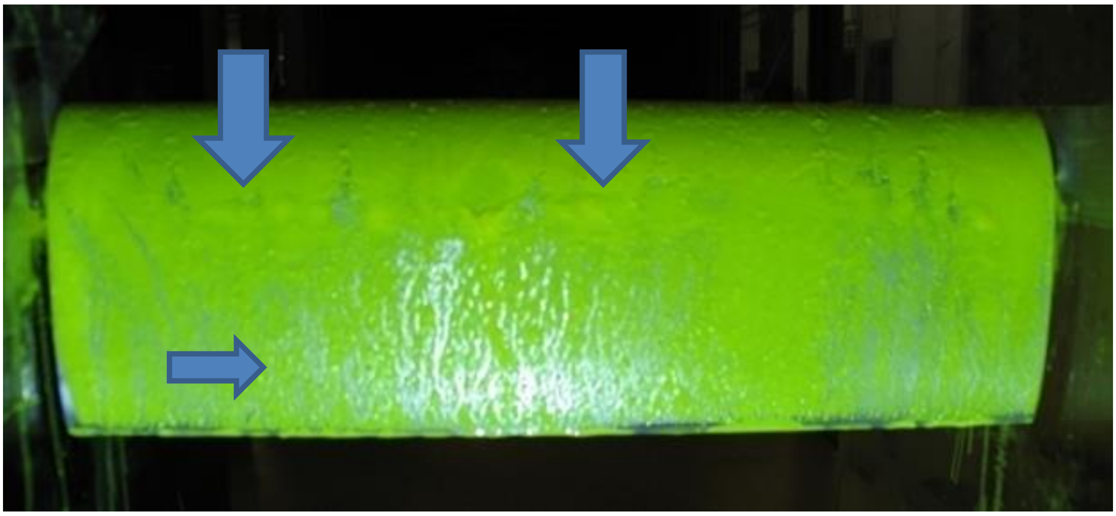

Figure 57. Upper is Skin Friction at 3^{o} angle of attaack and lower is the flow visualisation result at 3^{o} angle of attack

The skin friction pattern between 0 degree and 3 degree quite similar. However the strength of the skin friction at 0 degree is higher than at 3 degree. This could happen early since the Reynolds number low enough. Laminar flow starting from the leading edge easy to disturb with higher incidence angle since the kinetic energy not enough to climb the curvature shape of the aerofoil and also the surface roughness. Bubble separation occurs close to the maximum thickness of the model (Fig. 57).

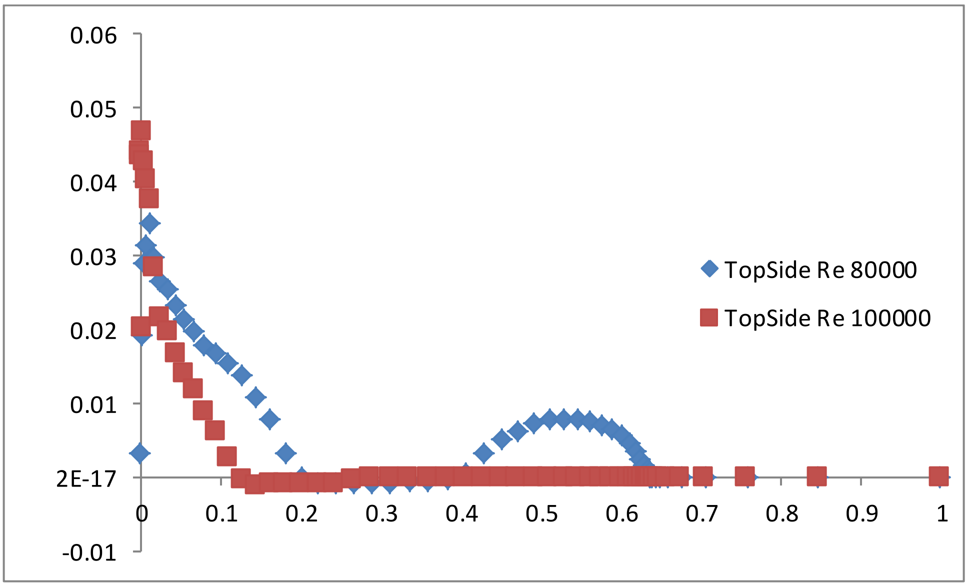

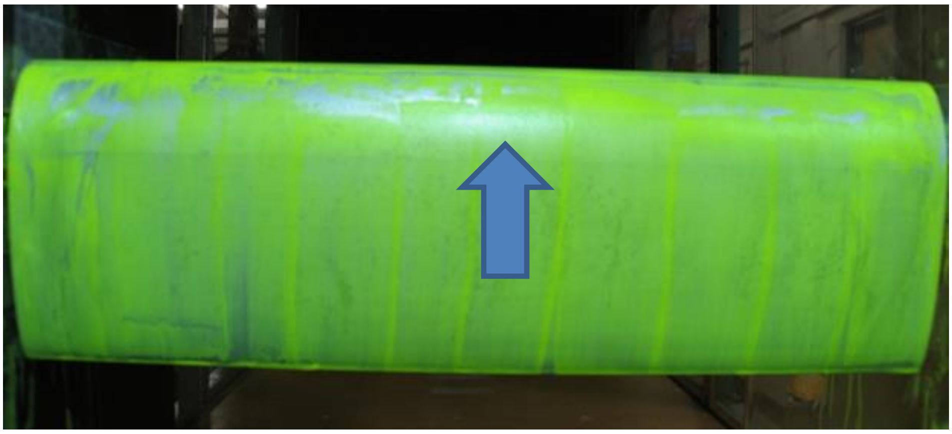

Figure 58. Upper is Skin Friction at 9^{o} angle of attaack and lower is the flow visualisation result at 9^{o} angle of attack

At figure 58 its appears that the flow already separate at early after 10% chord length since at 9^{o} post-stall condition already reach.

To summon, some bubble separation occurs close to the maximum thickness of the model. The distance between the leading edge to the point where the bubble separation start will be used to design the length of the riblets for the 2d model. At an incidence angle 9 degrees, the flow only attaches on a small region at the leading edge. We can see from figure 56 that the flow has utterly separate from the surface only left some remarks on the leading edge. The width of this remarks only 10 mm from the leading edge in the chordwise direction.

6.3 Pressure Measurement for 2D Model

The result from this experiment will shows drag profile and skin friction value of the model at three different angles of attack on three different points on the riblets surface; riblets shaft (P_1), the gap between riblets (P_3) and (P_2) middle area between shaft and gap.

These value plot on wake profile graphs which contains two key wake parameter; velocity defect and wake thickness. X-axis will represent the ratio of local mean velocity to free free stream velocity. While the test section is empty the distribution of the local mean velocity ration in the center usually homogenous to some extent. However, when a disturbance placed inside the distribution will be no longer homogenous. The minimum ratio of local mean velocity usually closed to the centerline of the disturbance. This value shows velocity defect caused by the model. Y-axis will display ratio of y-direction of the wake rake tube normalize to model mean chord length. A negative value represents the tube position below the chordwise of the model and the positive value position above the chordwise. Exactly on chordwise, the y value is zero. How far the disturbance changes the local velocity distribution along the y-axis will be representing the thickness of the wake produced by the disturbance. Drag profile could be derived from these graphs using the momentum balance analysis.

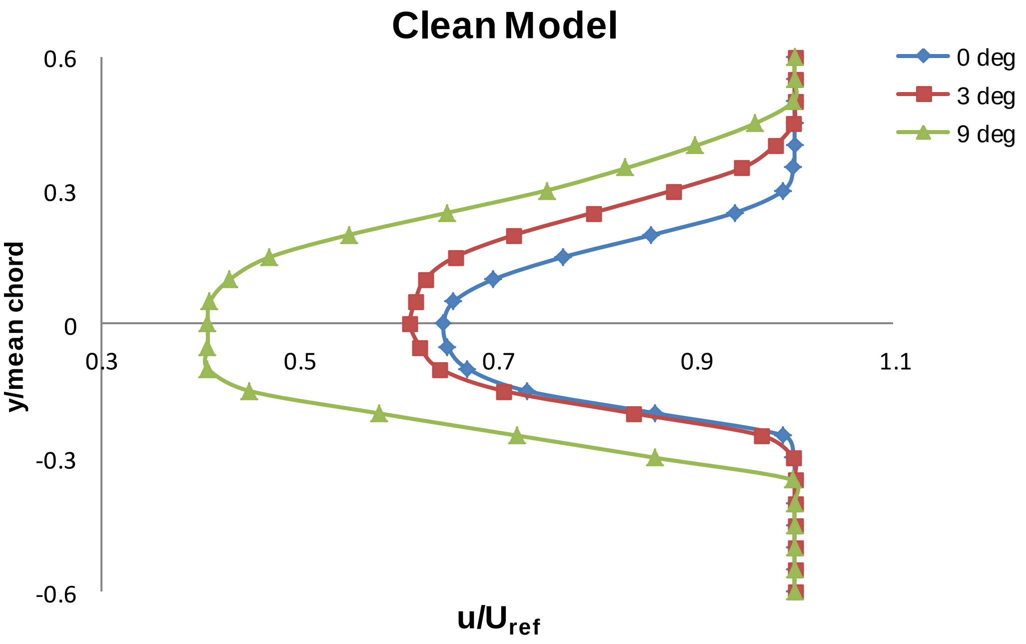

Figure 59. Mean Local Velocity Profile downstream 2D Model with clean surface

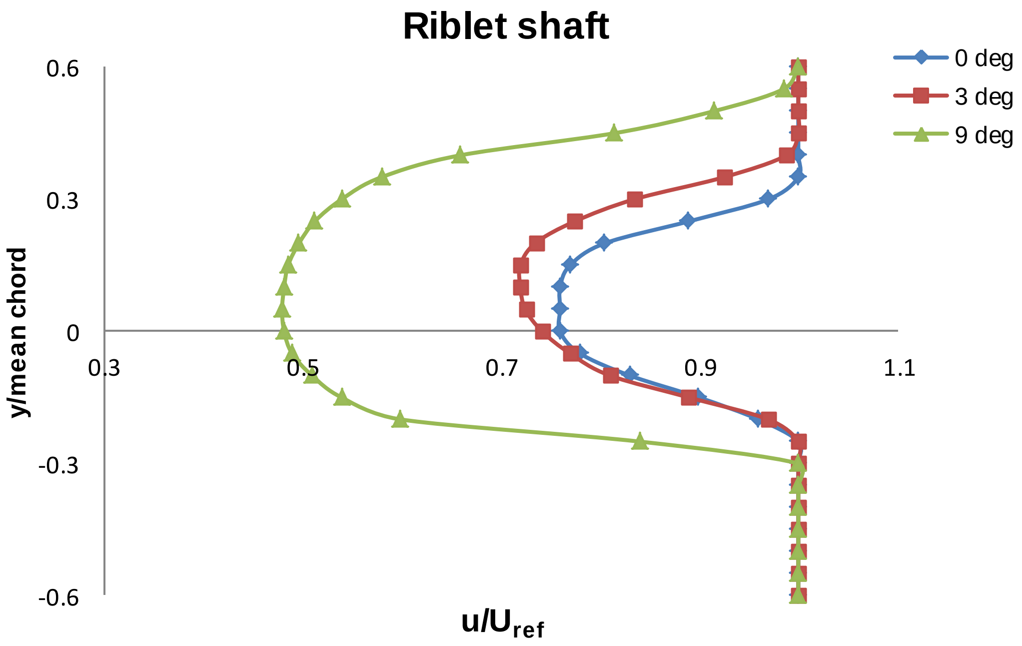

Figure 60. Mean Local Velocity Profile downstream Shaft of Riblet on The 2D Model

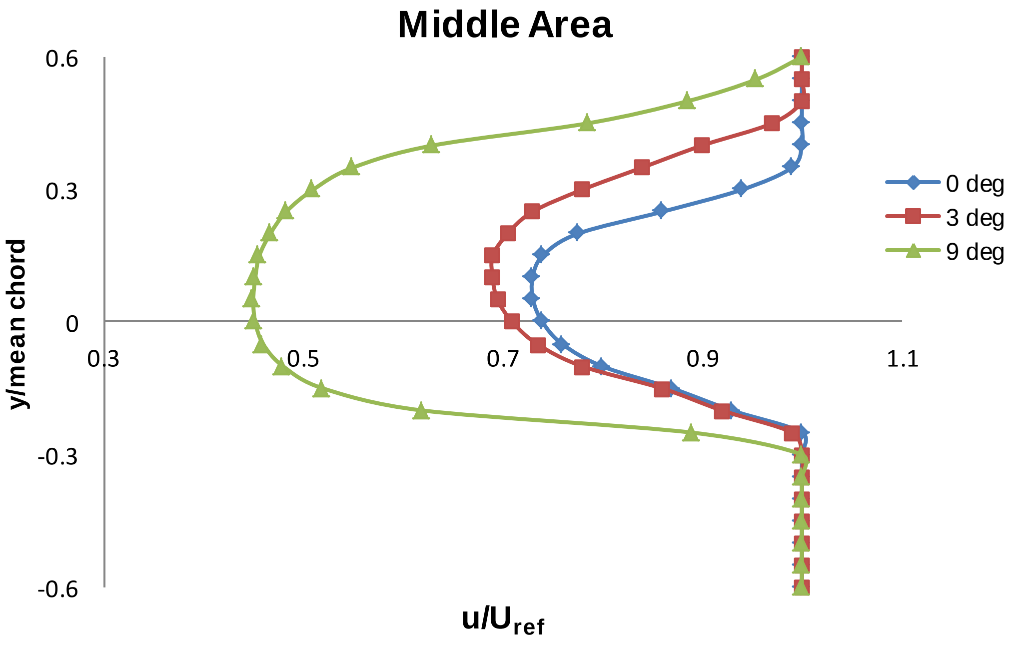

Figure 61. Mean Local Velocity Profile downstream Middle Area of Riblet on The 2D Model

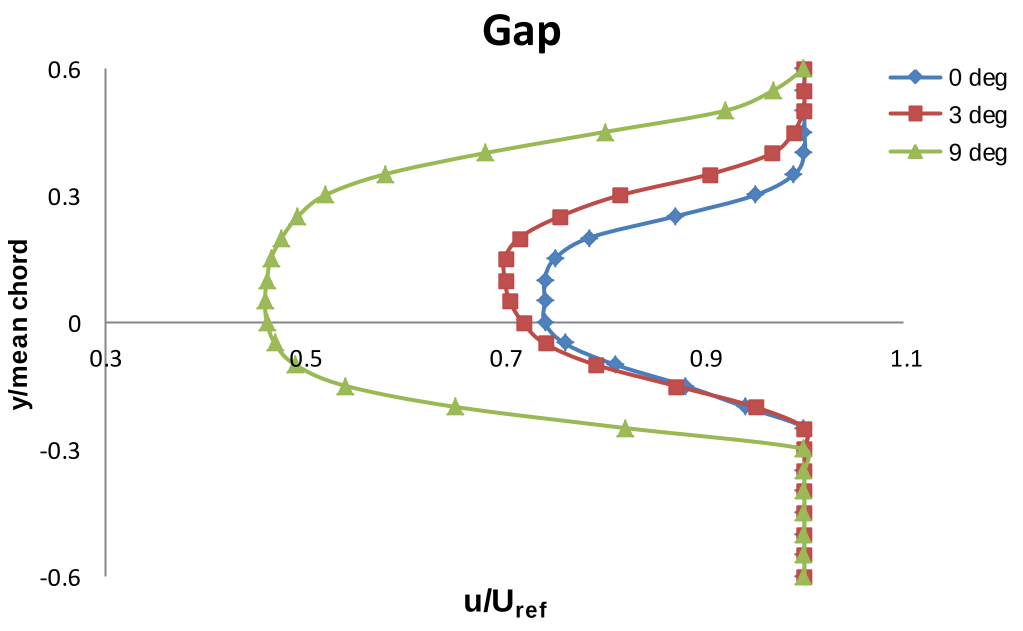

Figure 62. Mean Local Velocity Profile downstream Middle Area of Riblet on The 2D Model

Figure 57, 58, 59 and 60 show mean velocity profile downstream 2D model for clean model, divergent pattern (riblets shaft), middle area and gap at 0 degrees, 3 degrees and 9-degree angle of attack. Those curves show that the area will be wider when the angle of attack increase, since the drag from the force measurement also show incremental value. The minimum local mean velocity behind the clean model lower than the riblets model while the thickness of the wake behind the clean model thicker than riblets model. However, the area of the curves on the clean model wider than in the riblets model at a low incidence angle. These conditions agree with the force measurement result that drag reduction appears at a low incidence angle. The value the wake parameter and the drag could be found in Table in Appendix D.

The table shows that the minimum local mean velocity behind the riblets model not similar between 3 different positions along the riblets span, although they still lower compared with the clean model. The thickness of the wake also shows a different value. Some parameter related to the pressure measurement behind the riblets will be demonstrated in the spanwise direction of the riblets. The phenomenon capture from the data will be studied.

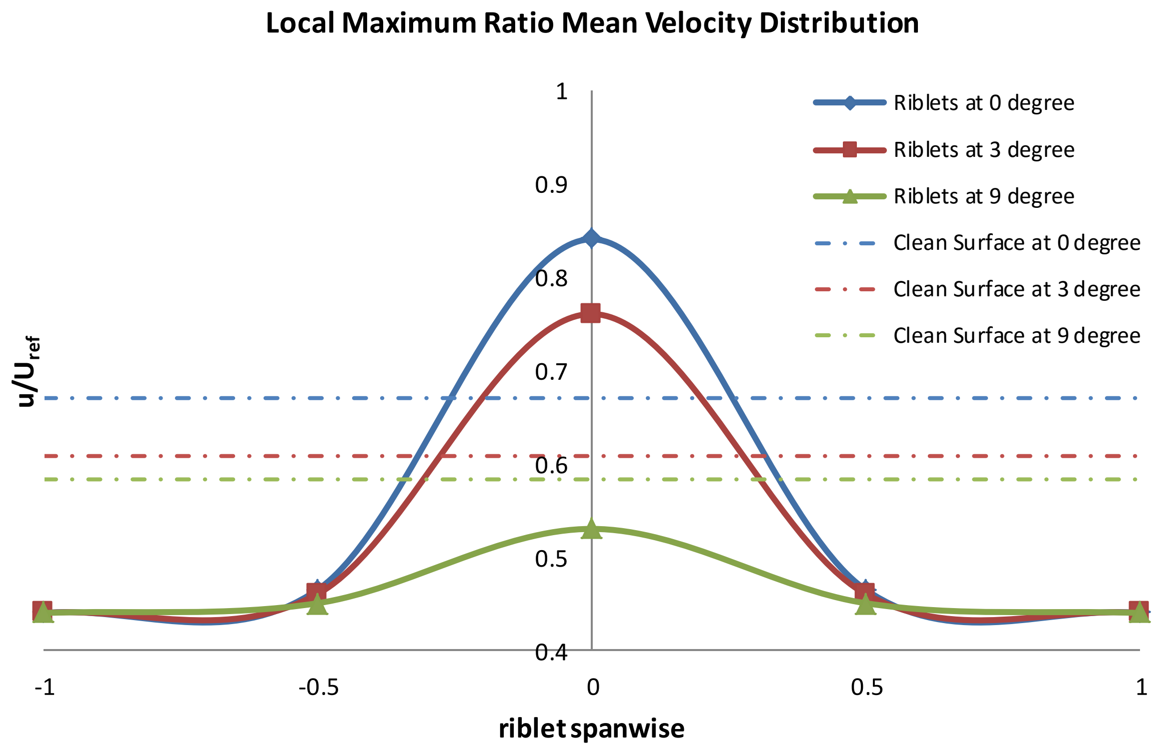

Figure 63. Distribution of Maximum Local Mean Streamwise Velocity along The Spanwise of Riblet

Figure 61 shows the distribution of local maximum mean streamwise velocity normalize with reference velocity along the spanwise of riblets. These value extract from velocity profile graphs for five points measurement at three different angle of attack.

The peak value occurs on the shaft of the riblets (divergent pattern) and sharply reduce until the middle area of the riblets and keep decrease slightly outward (convergent pattern). On the high-velocity region produce locally thinned boundary layer. Conversely, the boundary layer locally thickened above the low-velocity region. The surface on the convergent pattern tends to reduce the speed of the fluid near the wall since the riblets has small yaw angle to the flow direction. The fluid has to move away from the wall resulting thicker boundary layer. However, on the riblets shaft the fluid speed up since the line of the shaft has little disturbance and as a consequence of continuity.

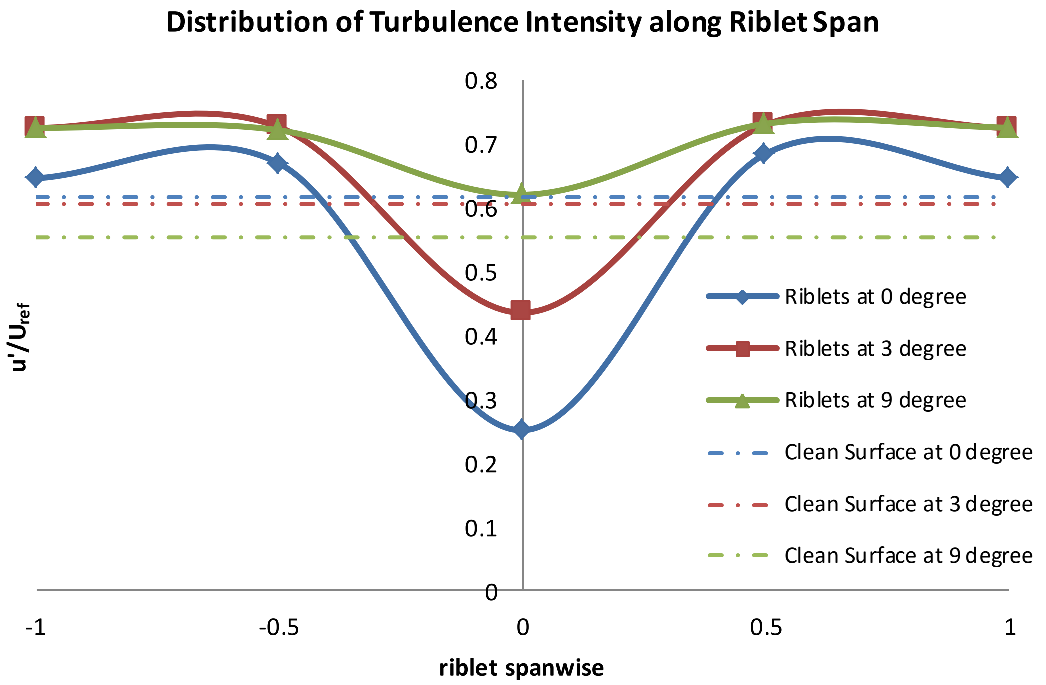

Figure 64. Distribution of Maximum Local Turbulence Intensity along The Spanwise of Riblet

Figure 62 show clearly distribution of local fluctuation streamwise velocity along the spanwise of the riblets. The turbulence intensity is calculated as the root-mean-squared variation of the total velocity u about the local mean at that particular location U (which is a function of y and z with the surface roughness installed).

$$u'(y,z) = \sqrt{\overline{[u(y,z,t) - U(y,z)]^2}}$$

Thus the local turbulence intensity in Figure 62 show the standard deviation of turbulent fluctuations about the local mean velocity shown in Figure 61.

Instead of increasing the local mean speed at the same time the turbulence intensity decrease on riblets shaft and vice versa the turbulence intensity increase on the lower mean velocity area. Such a situation would counsel that the joining portion of the riblets surface (where the flow ‘converges’ together) can end in a vertical flow of fluid far from the wall (forming the common- flow-up region of the counter-rotating vortex pair), whereas the oblique region will cause an area mean vertical rate part towards the wall which can type the common-flow-down portion of the counter-rotating vortex array.

The common-slowdown can tend to confine the turbulent fluctuations nearer to the surface (and thus cause reduced turbulent intensity across the bulk of the layer). Common-flow-up regions, on the opposite hand, can move the upper near-wall turbulent fluctuations any far from the surface, resulting in magnified turbulent intensity in these areas. Various vortex generator studies (for example Mehta and Bradshaw, 1988) have shown that high turbulent intensities occur in common-flow-up regions of the vortex induced flow field.

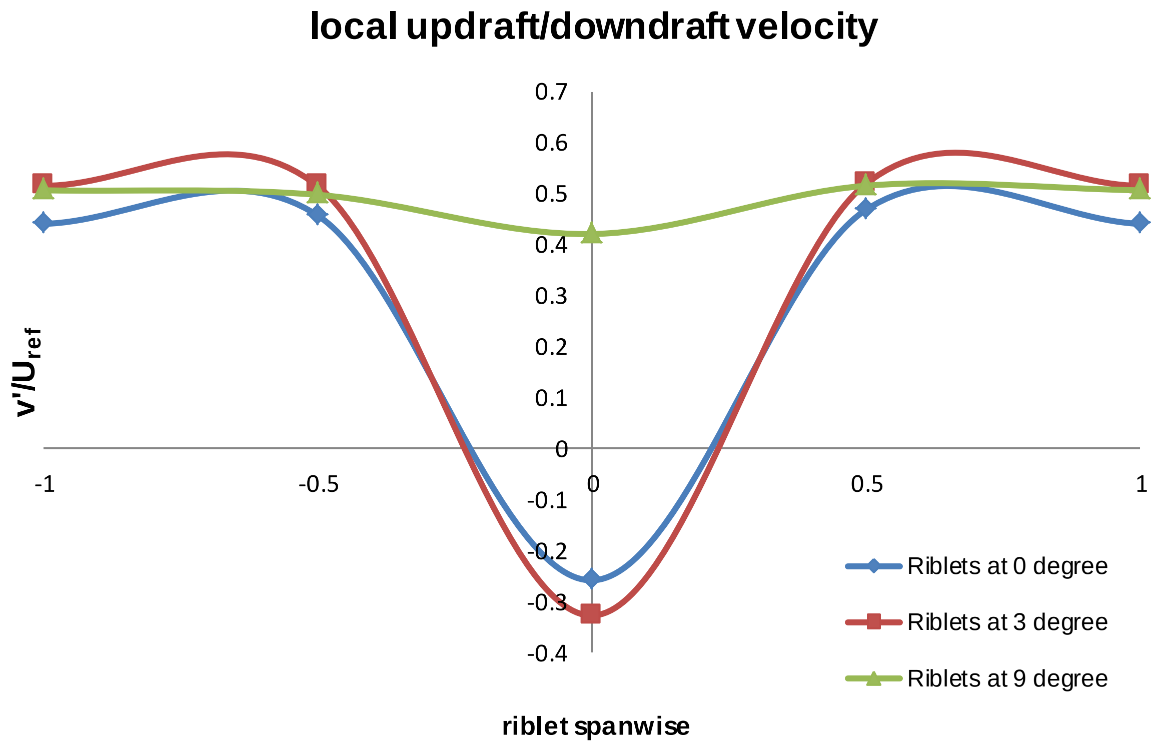

Figure 65. Distribution of Local Vertical Velocity along The Spanwise of Riblet

Figure 63 show distribution of vertical velocity on herringbone riblets span. Negative velocity (downdraft) occurs above the riblets shaft. The vector velocity become positive (updraft) close to the gap (convergent pattern). These data confirm that the counter rotating pair vortex emerge on herringbone riblets pattern. Its appear to be counter clockwise rotating secondary flow to the outside of the shaft. However, further measurement must be accomplished to assure whether the fluid reach the base of the groove or only sweep up the peaks of the riblets.

At low angle of attack, the downdraft value reduce while the angle of attack increase. Compared with the smooth model, the vertical velocity component of the riblets model has larger values and shows spanwise variation in the wake region. This indicates that the herringbone riblets pattern enhance the entrainment of inviscid flow into the wake behind the model for the case of drag reduction.

At high angle of attack (9 degree) for which the drag is higher on the riblets model than on the smooth model, however, the magnitude of the vertical velocity is a little reduced and shows an almost uniform distribution in the wake center region. However, the smooth model has larger vertical velocity values than the riblets model at the same flow speed.

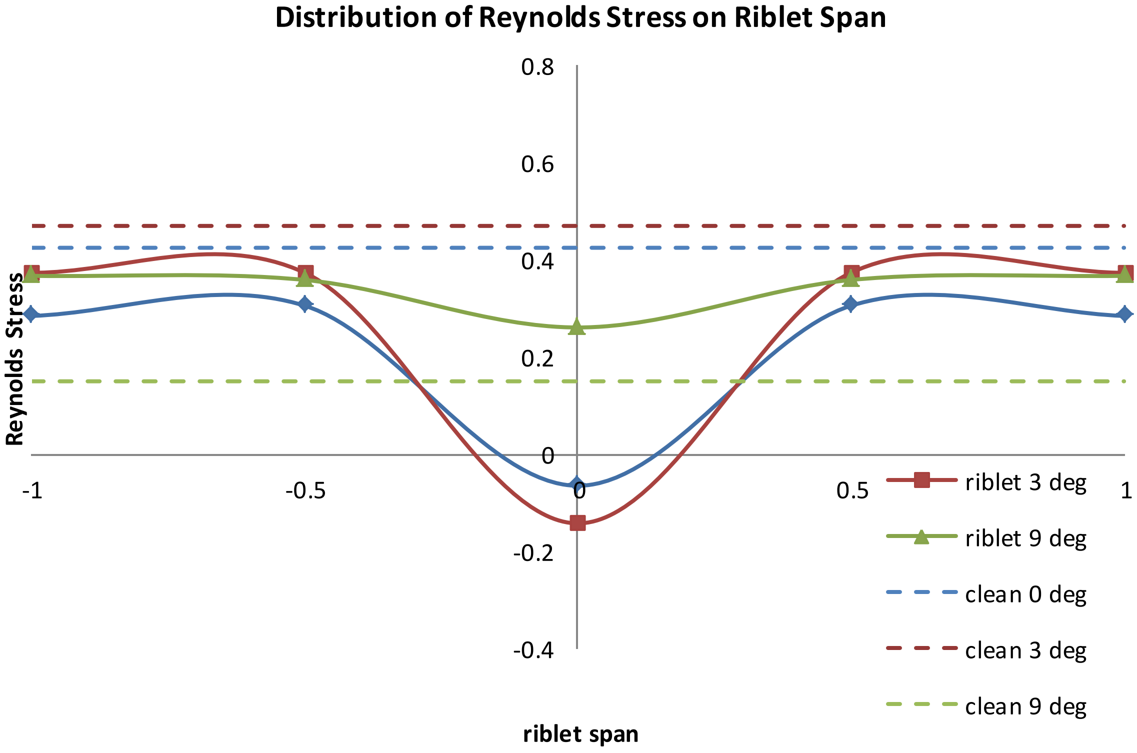

Figure 66. Distribution Local Reynolds Stress along spanwise of the riblet

Figure 64 shows that the lowest value of Reynolds stress occurs above riblets shaft and increase outward. At low angle of attack (0 degree and 3 degree) the reduction almost 0.4 while amplifying effect shows at high angle of attack around 0.1. This graph has similar trendline with distribution of local turbulence kinetic energy over span of the herringbone riblets.

The turbulence kinetic energy k for isotropic flows is evaluated using the following equation (Ciocan et al., 2000):

$$k = \frac{1}{2}\rho(\bar{u}^2 + \bar{v}^2 + \bar{w}^2) = \frac{3}{4}\rho(\bar{v}^2 + \bar{w}^2)$$

Due to the assumption of isotropic flow structure, the real turbulence kinetic energy may differ slightly from the present results in the regions of non-isotropic three-dimensional flow structure.

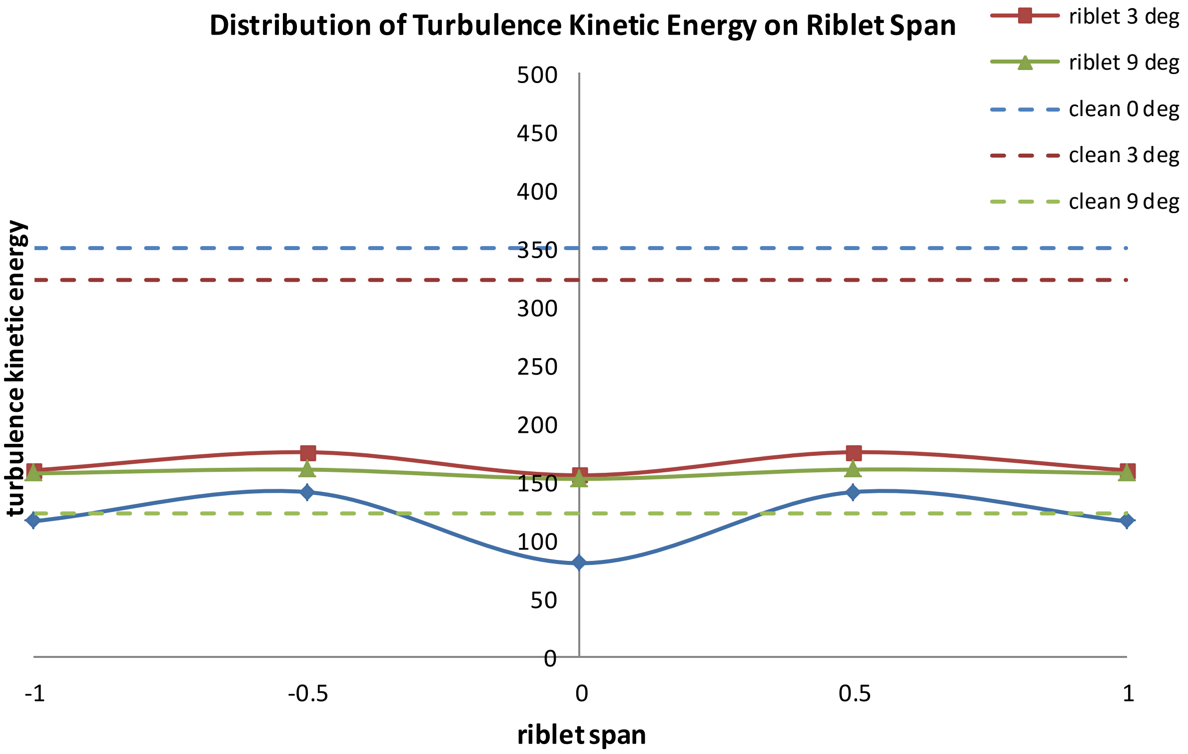

Figure 67. Distribution Local Turbulent Kinetic Energy along Spanwise of the Riblet

Figure 65 shows distribution local turbulent kinetic energy along spanwise of the riblets measured 60 per cent chord length downstream of the model. The high-intensity turbulent kinetic energy widely occupies in the central region behind the smooth surface model. However, compared with the smooth surface case, the equivalent high-intensity turbulent kinetic energy region is relatively reduced. This flow behavior may be attributed to the suppression of the formation of secondary vortices in the region just behind the herringbone riblets model; the secondary vortices seem to be broken into smaller eddies by the sharp peaks of the groove of yawed riblets. This is consistent with the observation that at this angle of attack the drag coefficient of the herringbone riblets model is lower than that of the smooth surface.

The growth of turbulence fluctuations in the region just behind the riblet, as a result of the higher angle of attack. This indicates that the riblets grooves do not suppress the formation of secondary vortices, but rather enhance flow separation from the model surface. In other words, for the case of drag reduction at the low angle of attack, the near wake is relatively little disturbed by riblets grooves and the high-intensity kinetic energy is reduced behind the model. On the other hand, at a higher angle of attack, the oncoming flow interacts actively with yawed grooves of micro-riblets, increasing the drag coefficient and turbulent kinetic energy. The interruption of the intercomponent transfer of turbulent kinetic energy is a mechanism for turbulence suppression and skin-friction reduction by spanwise wall oscillation.

7 Conclusions

The wind tunnel experiment confirmed that herringbone-type riblets have an effect on the flow around a wing model. The following findings were observed:

1. At Reynolds number 80000 herringbone-type riblets behave as a damper, eliminating the flow fluctuations seen on the smooth surface. However, this effect might will be different higher velocities;
2. The enhancement of lift coefficient almost 50% come from smoothering the boundary layer near the wall because of the riblets structure.
3. The drag reduction reach 20% in this experiment at incidence angle 0^o until 6^o. This reduction mechanism reveal from pressure measurement.
4. This small herringbone riblets could modify pressure distribution periodically over its span. Mean flow and turbulence intensity distribution over the span shows that the fluid speed up in the divergent valley during convergent pattern hindrance the movement of the fluid. As a consequence from continuity law the recirculating in the cross stream plane across the entire boundary layer create downwash motion on the diverging region and upwash motion above converging region. These counter-rotating flow above the riblets peak influence the momentum transport inside the riblets valley along the spanwise. This modified structure lead to rising the turbulence intensity, Reynolds stress and turbulence kinetic energy on convergent pattern while the lowest value of this parameter occurs above the divergent pattern. However, compared to the result from the smooth surface all these parameters still smaller except for high angle of attack condition. We can conclude that the herringbone riblets could suppression of turbulent momentum transport.
5. The data gain from this experiment shows similar trend with data from other low Reynolds number experiment.

8 Suggestions for Further Work

In addition to the work done throughout this project, which is overviewed in the Project Planning section as an Appendix E, some suggestions for future work are also outlined. The experience gained during the project gave a strong foundation within the field of interest. Consequently, understanding of the experimental process as well as the analysis of gathered results provided with some apparent limitations which can be assessed to achieve refined results. Hence, the suggestions for improving future research are listed below as follow:

Improving the design of the model and the riblets:

1. Constructing the bird wing model in a way to the flow over its surface would be more predictable, and the model could be delineated and replicated for future works. It can be done by employing straight leading/trailing edges, known or descriptive aerofoils and surface curvature in a span-wise direction. As alternative aerofoils from the NACA family can be employed.
2. Removing the aerodynamically deficient base of the model, representing a part of the pigeon body;
3. Using riblets foils of a descriptive geometry and with a sharp peak rather than the straight leading edge;

Improving experimental process:

1. If possible, doing CFD test on a model before manufacturing, to observe the predictable flow performance;
2. Doing pressure tap measurement before fitting the riblets to understand the flow over the wing better so the riblets were applied at more efficient locations;
3. Doing time dependent measurement to find out any change occurs on any parameter regarding to the strength of secondary flow related to geometry of the herringbone riblets.

Improving wind tunnel testing process:

1. Making sure the wind tunnel runs smoothly at all times by introducing more flow calibration tests, eliminating chances of random technical errors;

2. Waiting for a longer period of time in between data recordings, so the flow could settle and the chances of fluctuating data would be kept to a minimum;
3. Running more tests so the data would be more reliable;
4. Trying an even wider range of incidence angles to observe the general trends and then focusing on the region of interest; trying a wider range of flow velocities.
5. If the suggestions give a positive response then a more advanced type of spatial-3D herringbone riblets can be introduced for further testing. For comparison of the results, longitudinal riblets can be tested on the same model.

References

1. Bachmann, T.W. (2010). ‘Anatomical, Morphometrical and Biomechanical Studies of Barn Owls‘ and Pigeons‘ Wings‘. RWTH Aachen University.
2. Barlow, Jewel B., Rae, William H., Pope, Alan. *Low-Speed Wind Tunnel Testing*, John Wiley & Sons, Inc., New York 1999.
3. Bechert, D.W., Bruse, M., Hage, W., Van der Hoeven, J.G.T., Hoppe, G. (1997). ‘Experiments on drag-reducing surfaces and their optimization with an adjustable geometry’. Journal of Fluid Mechanics, 338(1), pp. 59-87.
4. Bechert, D.W., Bruse, M., Hage, W., Meyer, R. (2000). ‘Fluid Mechanics of Biological Surfaces and their Technological Application’. Naturwissenschaften, 87(1), pp. 157-171.
5. Benschop, H.O.G., and Breugem, W.-P. (2017). ‘Drag reduction by herringbone riblet texture in direct numerical simulations of turbulent channel flow’. Journal of Turbulence, 18:8, 717-759, DOI: 10.1080/14685248.2017.1319951.
6. Bhushan, B. (2009). ‘Biomimetics: lessons from nature – an overview’. Philosophical Transactions of the Royal Society A, 367(1), pp. 1466-1469.
7. Bhushan, B. and Bixler, G.D. (2013). ‘Fluid Drag Reduction with Shark-Skin Riblet Inspired Microstructured Surfaces’. Advanced Functional Materials, 23(1), pp. 4507-4528.
8. Ceballos, J. and Dillon, E. (2015). ‘Shark skin sleuthing’. Available at: https://saveourseas.com/update/shark-skin-sleuthing/ [Accessed 21Apr. 2018].
9. Chen, H., Rao, F., Shang, X., Zhang, D., Hagiwara, I. (2013). ‘Biomimetic Drag Reduction Study on Herringbone Riblets of Bird Feather’. Journal of Bionic Engineering, 10(1), pp. 341-349.
10. Chen, H., Rao, F., Shang, X., Zhang, D., Hagiwara, I. (2014). ‘Flow over bio-inspired 3D herringbone riblets’. Exp Fluids, 55:1698.
11. Choi, K.S., Yang, X., Clayton, B.R., Glover, E.J., Altar, M., Semenov, B.N., Kulik, V.M. (1997). ‘Turbulent drag reduction using compliant surfaces‘. Proceedings of the Royal Society A, 453(1), pp. 2229-2240.

12. Cousteix, J. (1992). ‘Basic Concepts on Boundary Layers. Special Course on Skin Friction Drag Reduction‘. AGARD-R-786(2), pp. 1-2.
13. Dean, B. and Bhushan, B. (2010). ‘Shark-skin surfaces for fluid-drag reduction in turbulent flow: A review‘. Philosophical Transactions of the Royal Society A, 368(1), pp. 4775-4806.
14. Gersten, K. and Schlichting, H. (1975) Boundary layer theory, 7th edn. McGraw-Hill, New York.
15. Guglielmo, James J., Selig, Michael S., *Spanwise Variation in Profile Drag for Airfoils at Low Reynolds Nubmers,* University of Illinois at Urbana-Champaign. AIAA Journal of Aircraft Vol. 33, No.4, July-August 1996.
16. Krause, Lloyd N. (1951). ‘Effect of Pressure Rake Design Parameter On Static Pressure Measurement for Rake used in Subsonic Free jet’, NACATN 2520, Washington, USA.
17. Lang, A., Habegger, M.L., Motta, P. (2012). ‘Shark Skin Drag Reduction‘. In: Encyclopedia of Nanotechnology. Tampa: Springer Netherlands, pp. 2394-2400.
18. Mueller, Aerodynamic Measurements at Low Reynolds Numbers", AIAA 82-0598, 1982
19. Muti Lin, J.C. and Pauley, L.L. (1996). ‘Low-Reynolds-Number Separation on an Airfoil‘. AIAA Journal, 34(8), pp. 1570-1577.
20. Nachtigall, W. (1998). ‘Starlings and starling models in wind tunnels‘. Journal of Avian Biology, 29(1), pp. 478-484.
21. Neumann, D., Dinkelacker, A. (1991). ‘Drag measurements on V-grooved surfaces on a body of revolution in axial flow‘. Applied Scientific Research, 48(1), pp. 105-114.
22. Nicholas E. Durston, , Xue Wan, Jian G. Liu and Shane P. Windsor, Avian surface reconstruction in free flight with application to flight stability analysis of a barn owl and peregrine falcon, Journal of Experimental Biology, 2019
23. Nugroho, B., Hutchins, N. and Monty, J.P. (2013). ‘Large-scale spanwise periodicity in a turbulent boundary layer induced by highly ordered and directional surface roughness‘. International Journal of Heat and Fluid Flow, 41(1), pp. 90-102.
24. Pennycuick, C.J. (1968). ‘A wind-tunnel study of gliding flight in the pigeon Columba Livia‘. J. Exp. Biol., 49(1), pp. 509-526.

25. Rothe, H.-J., and Nachtigall, W. (1986). ‘Pigeon flight in a wind tunnel. Aspects of wind tunnel design, training methods and flight behaviour of different pigeon races‘. Journal of Comparative Physiology B, 157(1), pp. 91-98.
26. Sareen, A., Deters, R.W., Henry, S.P., Selig, M.S. (2011). ‘Drag Reduction Using Riblet Film Applied to Airfoils for Wind Turbines‘. In: 49 th AIAA Aerospace Sciences Meeting. Orlando, United States of America, pp. 1-19.
27. Subaschandar, N., Kumar, R., Sundaram, S. (1999). ‘Drag Reduction Due to Riblets on a GAW(2) Airfoil‘. Journal of Aircraft, 36(5), pp. 890-892.
28. Tucker, A.V. and Parrot, C.G. (1970). ‘Aerodynamics of gliding flight in a falcon and other birds‘. The Journal of Experimental Biology, 52(1), pp. 345-367.
29. Traub, L. W. Effect of Rapid-Prototyped Airfoil Finish on Loading at Low Reynolds Numbers. Journal of Aircraft, 50(1):307–311, 2013.
30. Viswanath, P.R. (2002). ‘Aircraft viscous drag reduction using riblets‘. Progress in Aerospace Sciences, 38(1), pp. 571-600.
31. Walsh, M.J. (1983). ‘Riblets as a viscous drag reduction technique‘. AIAA Journal, 21(1), pp. 485-486.
32. White, F.M. (1991). Viscous Fluid Flow, 2nd edn. ed. New York: McGraw-Hill, p. 11.
33. Yaws, C L. Braker, W. (2001). Matheson Gas Data Book, 7th edn. McGraw-Hill Professional, New York, USA.

Appendix A. Camber and Thickness Parameters of a Real Pigeon Wing.

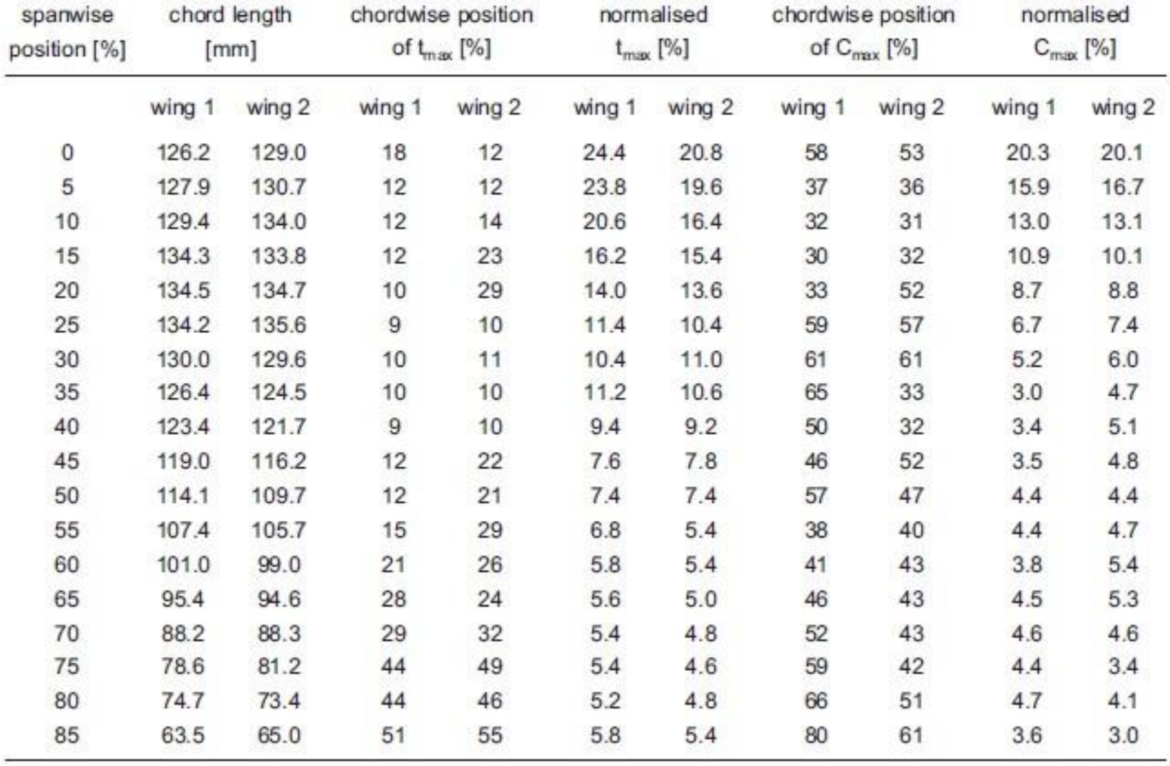

spanwise position [%]	chord length [mm]		chordwise position of t_{max} [%]		normalised t_{max} [%]		chordwise position of C_{max} [%]		normalised C_{max} [%]	
	wing 1	wing 2	wing 1	wing 2	wing 1	wing 2	wing 1	wing 2	wing 1	wing 2
0	126.2	129.0	18	12	24.4	20.8	58	53	20.3	20.1
5	127.9	130.7	12	12	23.8	19.6	37	36	15.9	16.7
10	129.4	134.0	12	14	20.6	16.4	32	31	13.0	13.1
15	134.3	133.8	12	23	16.2	15.4	30	32	10.9	10.1
20	134.5	134.7	10	29	14.0	13.6	33	52	8.7	8.8
25	134.2	135.6	9	10	11.4	10.4	59	57	6.7	7.4
30	130.0	129.6	10	11	10.4	11.0	61	61	5.2	6.0
35	126.4	124.5	10	10	11.2	10.6	65	33	3.0	4.7
40	123.4	121.7	9	10	9.4	9.2	50	32	3.4	5.1
45	119.0	116.2	12	22	7.6	7.8	46	52	3.5	4.8
50	114.1	109.7	12	21	7.4	7.4	57	47	4.4	4.4
55	107.4	105.7	15	29	6.8	5.4	38	40	4.4	4.7
60	101.0	99.0	21	26	5.8	5.4	41	43	3.8	5.4
65	95.4	94.6	28	24	5.6	5.0	46	43	4.5	5.3
70	88.2	88.3	29	32	5.4	4.8	52	43	4.6	4.6
75	78.6	81.2	44	49	5.4	4.6	59	42	4.4	3.4
80	74.7	73.4	44	46	5.2	4.8	66	51	4.7	4.1
85	63.5	65.0	51	55	5.8	5.4	80	61	3.6	3.0

Figure A- I. Positions and values of the maximum camber and the maximum thickness of two pigeon wings (Columba livia) normalised by the local chord length (Bachmann, 2010).

Base sketch of a pigeon wing model, corresponding to the data under 'wing 2' sections in the table above.

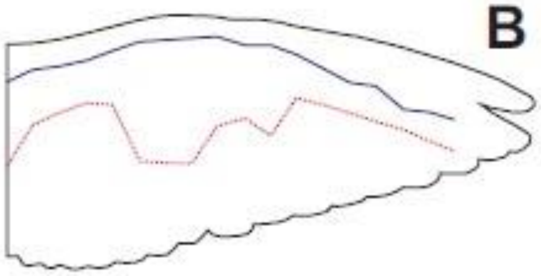

Figure A- II. Pigeon Wing Planform (Bachmann, 2010)

Appendix B. Seven hole probe Calibration Theory and Data Reduction

B.1. Definition and Convention

The hole numbering convention is the first that must be established. Figure B-1 shows a front view of a 7 hole probe. The probe stem is shown in the view, and the holes numbered relative to this orientation. The sign conventions of three angles are also defined in this view – pitch, yaw, and roll.

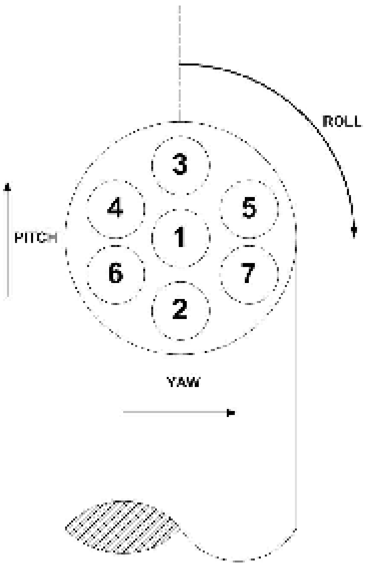

Figure B- 1. Probe Numbering and Angle Conventions

The flow angle relative to the probe tip can be defined using two coordinate systems. The pitch and yaw coordinate system defines two flow angles that are referenced to the probe's X and Y axis. The cone and roll coordinate system is a polar coordinate system. The cone angle is the total angle of attack to the probe axis, and the roll angle is a rotation angle that is referenced to a fixed probe axis. The definition of these angles, as well as the coordinate system that is assumed is shown schematically in Figure B-2 and the definitions of each angle are tabulated in Table B-1. Angles with a subscript T are tangent angles, which are measured between projections of the velocity vector.

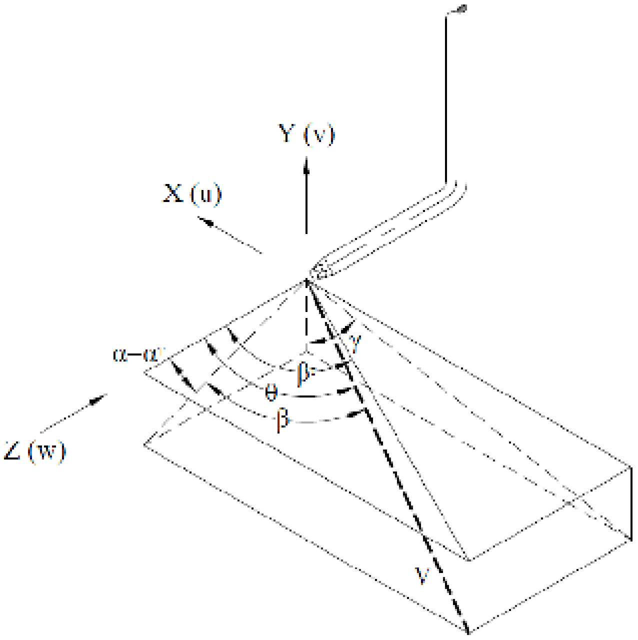

Figure B- 2. Flow Angle and Coordinate System Convention

Table B- 1. Flow Angle Conventions

Angle	Term	Rigime	Definition
α	Pitch	Low Angle	Angle between w and YZ projection of velocity
β	Yaw	Low Angle	Angle between velocity vector and YZ projection of velocity
θ	Cone	High Angle	Angle between w and the velocity vector
γ	Roll	High Angle	Angle between -v and X-Y projection of velocity

B.2. Governing Equations and Coefficients

A calibration data reduction is then employed the polynomial curve fit method of Gallington. The calibration data are represented as dimensionless pressure coefficients, and a least square approach is used to fit the flow properties to third order polynomial expansions of pressure coefficient.

At low flow angles, flow remains attached over the entire surface of the probe and the central port (n57) reads the highest pressure. Pressure information from all seven holes may be used to determine the flow conditions. At high flow angles, separated flow occurs on the leeward side of the probe and an off-center port (n51 – 6) will read the highest pressure. Only a subset of the seven pressures is then used to determine the flow conditions, based on the port reading the maximum pressure and those ports immediately adjacent to it. This distinction between low and high angles leads to a sectoring scheme being employed, based on which port (n51 – 7) reads the highest pressure.

In a low angle flow, the highest pressure was read in port 1. P_1 was therefore the approximate flow total pressure. In low angle flow, the flow was assumed to be attached over all of the peripheral pressure ports, so the approximate static pressure was therefore calculated as shown in Equation (B-1)

$$\bar{P} = \frac{1}{6}\sum_{i=2}^{7} P_i$$

Equation B-1

The directional pressure coefficients for the low angle regime are shown in Equation B-2, B-3 and B-4. The pressure differences were normalized by the approximate dynamic pressure of the flow.

$$C_a = \frac{P_3 - P_2}{P_1 - P},$$

Equation B-2

$$C_b = \frac{P_4 - P_7}{P_1 - P},$$

Equation B-3

$$C_c = \frac{P_6 - P_5}{P_1 - P}$$

Equation B-4

These coefficients were weighted according to their relative positions on the probe tip and used to generate a further pair of coefficients that are representative of the pitch and yaw. The calculation of the pitch and yaw coefficients is shown in Equations (B-5) and (B-6). The relative weighting of the terms in the pitch and yaw coefficients was based solely on the geometry of the probe tip.

$$C_\alpha = \frac{2C_a + C_b + C_c}{3}$$

Equation B-5

$$C_\beta = \frac{C_b + C_c}{\sqrt{3}}$$

Equation B-6

The formulation of the total and dynamic pressure coefficients are shown in Equations (B-7) and (B-8), respectively. Pt and Pq represent the flow's true total and dynamic pressure, respectively.

$$C_t = \frac{P_1 - P_t}{P_1 - \bar{P}}$$

Equation B-7

$$C_q = \frac{P_1 - \bar{P}}{P_q}$$

Equation B-8

In a high angle flow, the highest pressure was read in one of the peripheral ports, and this port was referred to as port n. Pn was therefore taken to be the approximate flow total pressure. As mentioned, there was a high probability in high angle flow that the downwind side of the probe would be measuring in separated flow, so only pressures from hole n, the two immediately adjacent peripheral ports, and the centre port were considered. The pressure in the two adjacent peripheral ports was termed P+ and P-. The approximate static pressure of the flow was therefore calculated using Equation (B-9).

$$\bar{P}_n = \frac{P_+ + P_-}{2}$$

Equation B-9

Directional coefficients in the high angle regime were defined based on the polar coordinate system. This was convenient because it allowed only a single pair of coefficients to be defined, and that pair of coefficients was applicable to all six of the peripheral ports. Formulating yaw and pitch coefficients for the peripheral holes would have involved using unique scalar weightings for the pressure difference terms at each port. The cone and roll coefficients are introduced in Equations (B-10) and (B-11). Again, the terms were normalized by the approximate dynamic pressure of the flow.

$$C_\theta = \frac{P_n - P_1}{P_n - \bar{P}_n}$$

Equation B-10

$$C_\gamma = \frac{P_- - P_+}{P_n - \bar{P}_n}$$

Equation B-11

The total and dynamic pressure coefficients were formulated in a way very similar to those in the low angle regime. The expressions are shown in Equations (B-12) and (B-13).

$$C_{tn} = \frac{P_n - P_t}{P_n - \bar{P}_n}$$

Equation B-12

$$C_{qn} = \frac{P_n - \bar{P}_n}{P_q}$$

Equation B-13

It should be reiterated that the equations of flow in the high angle regime are only valid if four ports were reading in attached flow.

The mathematics of the polynomial curve fit method are shown in Equations (B-14) and (B-15) with fourth order terms included. The extension of the method to higher or lower order polynomials is intuitive, and would be achieved simply by omitting or adding terms that are of the same form as those shown below.

$$X = \begin{bmatrix} K_1^x + K_2^x C_\alpha + K_3^x C_\beta + K_4^x C_\alpha^2 + K_5^x C_\alpha C_\beta + K_6^x C_\beta^2 \\ +K_7^x C_\alpha^2 + K_8^x C_\alpha C_\alpha + K_9^x C_\alpha C_\alpha + K_{10}^x C_\alpha^2 + K_{11}^x C_\alpha^2 \\ +K_{12}^x C_\alpha^3 \quad C_\beta + K_{13}^x C_\alpha^2 C_\beta^2 + K_{14}^x C_\alpha C_\beta^3 + K_{15}^x C_\beta^2 \end{bmatrix}$$

Equation B-14

$$X = \begin{bmatrix} K_{1,n}^x + K_{2,n}^x C_{\theta n} + K_{3,n}^x C_{\gamma n} + K_{4,n}^x C_{\theta n}^2 + K_{5,n}^x C_{\theta n} C_{\gamma n} + K_{6,n}^x C_{\gamma n}^2 \\ +K_{7,n}^x C_{\theta n}^2 + K_{8,n}^x C_{\theta n} C_{\gamma n} + K_{9,n}^x C_\alpha C_\alpha + K_{10,n}^x C_\alpha^2 + K_{11,n}^x C_\alpha^2 \\ +K_{12,n}^x C_\alpha C_\alpha + K_{13,n}^x C_\alpha C_\alpha + K_{14,n}^x C_\alpha C_\alpha + K_{15,n}^x C_\alpha^2 \end{bmatrix}$$

Equation B-15

Equations (B-14) and (B-15) show the exact expressions that are used to calculate a flow property, X, given the two angular coefficients and a set of probe-dependant calibration coefficients. X represents each of the dependent variables – two flow angles, and total and dynamic pressure coefficients. All four of these properties are calculated in the same way.

These complete expansions can also be expressed in matrix form. Only the matrix form of the low angle expression is shown, for brevity. Equation (B-16) shows that once the calibration coefficients are known, any number of points (m) can be converted to flow properties quickly and efficiently using simple matrix multiplication.

$$\begin{Bmatrix} X_1 \\ X_2 \\ X_3 \\ \vdots \\ X_m \end{Bmatrix} = \begin{bmatrix} 1 & C_{\alpha 1} & C_{\beta 1} & C_{\alpha 1}^2 & \cdots & C_{\beta 1}^4 \\ 1 & C_{\alpha 2} & C_{\beta 2} & C_{\alpha 2}^2 & \cdots & C_{\beta 2}^4 \\ 1 & C_{\alpha 3} & C_{\beta 3} & C_{\alpha 3}^2 & \cdots & C_{\beta 3}^4 \\ \vdots & \vdots & \vdots & \vdots & \cdots & \vdots \\ 1 & C_{\alpha m} & C_{\beta m} & C_{\alpha m}^2 & \cdots & C_{\beta 4}^4 \end{bmatrix} \begin{Bmatrix} K_1 \\ K_2 \\ K_3 \\ \vdots \\ K_{15} \end{Bmatrix}$$

Equation B-16

This matrix can be further simplified in its expression. The independent variable array is a function only of the angular pressure coefficients, and hence can be calculated directly from probe data. The dependent variable vector is known during calibration, but unknown when the probe is used to measure an arbitrary flow. Similarly, the calibration vector is unknown during calibration, but must be known when measuring an arbitrary flow. The matrix is expressed in a simplified form in Equation (B-17).

$$\{X\} = [TM]\{K\}$$

Equation B-17

From this expression, it is clear that relatively simple matrix algebra can be used to calculate the calibration vector, K, given that the flow properties are known during calibration. Conversely, it is clear that the only data required to calculate the flow properties in an arbitrary flow is the calibration vector. This leads to the main advantage of the polynomial surface method – once the expressions are formulated, the implementation time and computational expense to calibrate probes and solve arbitrary flows is quite low.

B.3. Data Verification

All the calibration results plots on some graphs below.

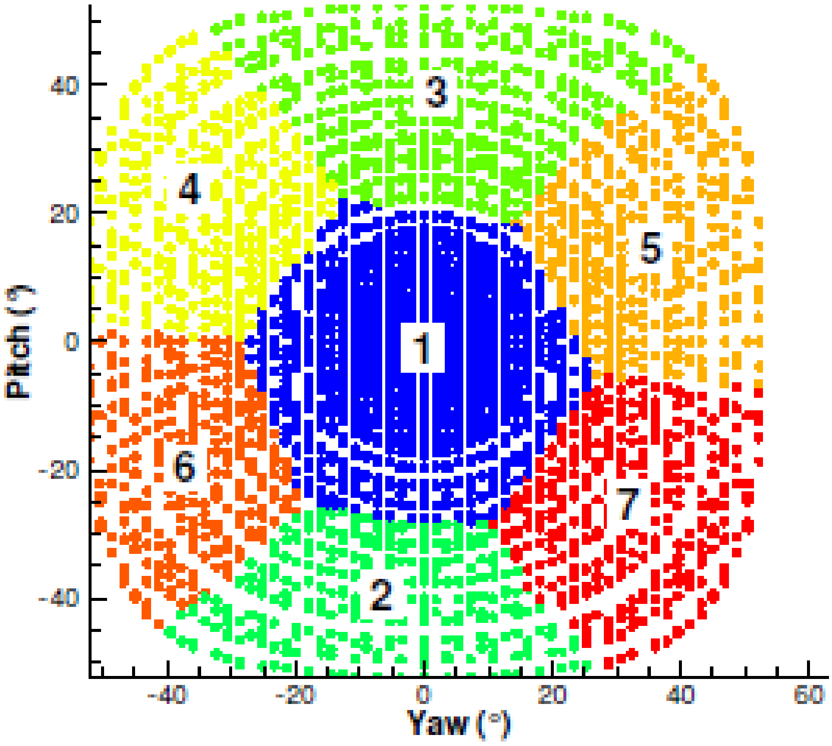

Figure B- 3. A plot for pitch and yaw for various velocity

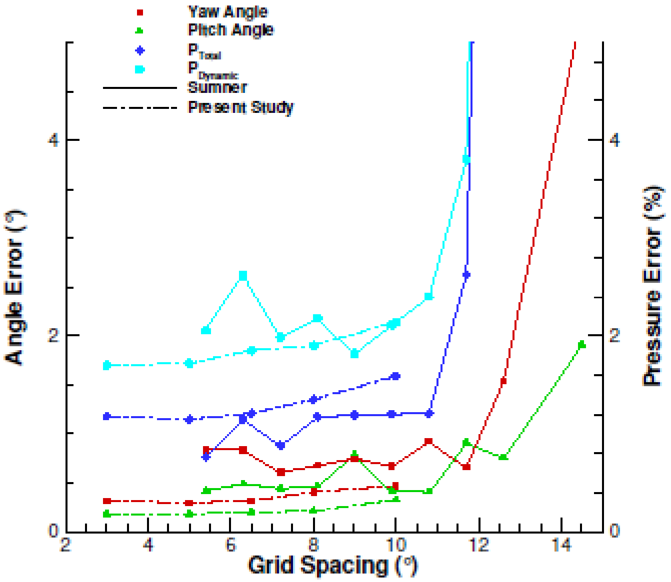

Figure B- 4 RMS Average Error for Low Sector

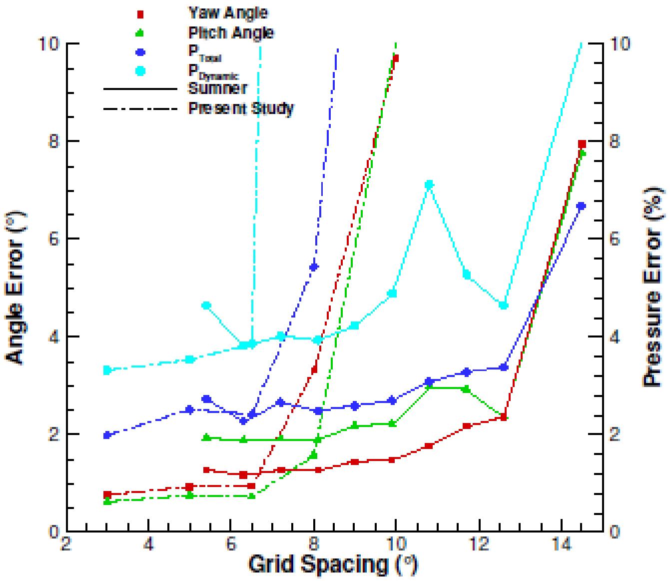

Figure B- 5 RMS Average Error for High Sector

Appendix C. Uncertainty in Performance Measurements

C.1. Uncertainty in Flow Conditions

The uncertainties in the flow conditions for the experiments in this study were calculated using the equations in this section. Uncertainty estimates for the free stream dynamic pressure, atmospheric density, dynamic viscosity, free stream velocity, and Reynolds number are presented in Table D.1.

The free stream dynamic pressure calculation involved the contraction ratio across the tunnel inlet. Since the contraction ratio was constant and the uncertainty in the area ratio was assumed to be very low, the uncertainty in the contraction ratio was assumed to be negligible. Therefore, the pressure difference was the only factor that contributed to the uncertainty of the free stream dynamic pressure. Using Eq. 41, the uncertainty in the dynamic pressure was calculated to be,

$$U_{q_\infty} = \sqrt{\left(\frac{\partial q_\infty}{\partial (P_{ss} - P_{ts})} U_{(P_{ss}-P_{ts})}\right)^2}$$

Equation D.1

The uncertainty in the measured pressure difference between the settling section and the test section was also assumed constant. Thus, Eq. D.1 can be rewritten as,

$$U_{q_\infty} = \frac{\partial q_\infty}{\partial (P_{ss} - P_{ts})} U_{(P_{ss}-P_{ts})} = \frac{1}{1 - \left(\frac{A_{ts}}{A_{ss}}\right)^2} U_{(P_{ss}-P_{ts})}$$

Equation D.2

The atmospheric density was calculated using the ideal gas law. Since, the gas constant of air, R, is a constant, the only contributing quantities to the uncertainty of ρ_{amb} were P_{amb} and T_{amb}. The uncertainty was calculated using

$$U_{\rho_{amb}} = \sqrt{\left(\frac{\partial \rho_{amb}}{\partial P_{amb}} U_{P_{amb}}\right)^2 + \left(\frac{\partial \rho_{amb}}{\partial T_{amb}} U_{T_{amb}}\right)^2}$$

Equation D.3

Where

$$\frac{\partial \rho_{amb}}{\partial P_{amb}} = \frac{1}{RT_{amb}}$$

Equation D.4

$$\frac{\partial \rho_{amb}}{\partial T_{amb}} = \frac{P_{amb}}{RT_{amb}{}^{2}}$$

Equation D.5

The dynamic viscosity was calculated using Sutherland's formula,

$$\mu_{amb} = \mu_0 \frac{T_0 + C}{T_{amb} + C}\left(\frac{T_{amb}}{T_0}\right)^{3/2}$$

Equation D.6

with known constants $\mu 0$ = 3.58404 × 10^{-7} lb-s/ft^2, $T0$ = 491.6 R, and C = 199.8 R. Therefore, the only contributing factor to the uncertainty of the dynamic viscosity was the ambient temperature. The uncertainty was calculated using,

$$U_{\mu_{amb}} = \sqrt{\left(\frac{\partial \mu_{amb}}{\partial T_{amb}} U_{T_{amb}}\right)^2}$$

Equation D.7

Since the free stream velocity can be expressed in terms of the dynamic pressure using,

$$U_\infty = \sqrt{\frac{2q_\infty}{\rho_{amb}}}$$

Equation D.8

$$U_{U_\infty} = \sqrt{\left(\frac{\partial U_\infty}{\partial q_\infty} U_{q_\infty}\right)^2 + \left(\frac{\partial U_\infty}{\partial \rho_{amb}} U_{\rho_{amb}}\right)^2}$$

Equation D.9

The uncertainty in the free stream velocity was calculated using the already calculated $U_{\rho\text{-amb}}$ and $U_{q\infty}$

$$\frac{\partial U_\infty}{\partial q_\infty} = \frac{1}{\sqrt{2q_\infty \rho_{amb}}}$$

Equation D.10

$$\frac{\partial U_\infty}{\partial \rho_{amb}} = \frac{-1}{\rho_{amb}} \frac{q_\infty}{\sqrt{2\rho_{amb}}}$$

Equation D.11

The uncertainty of the Reynolds number had contributions from the free stream velocity, dynamic viscosity, density, and chord length. The machining precision for the aluminum sections of the model was assumed to be 0.005 inches, based on standard precision of computer numerical control fabrication machines. Therefore, the uncertainty in the Reynolds number was determined using,

$$U_{\Re} = \sqrt{\left(\frac{\partial \Re e}{\partial U_\infty} U_{U_\infty}\right)^2 + \left(\frac{\partial \Re e}{\partial \rho_{amb}} U_{\rho_{amb}}\right)^2 + \left(\frac{\partial \Re e}{\partial \mu_{amb}} U_{\mu_{amb}}\right)^2 + \left(\frac{\partial \Re e}{\partial c} U_c\right)^2}$$

Equation D.12

Where

$$\frac{\partial \Re e}{\partial U_\infty} U_{U_\infty} = \frac{\rho_{amb} c}{\mu_{amb}}$$

Equation D.13

$$\frac{\partial \Re e}{\partial \rho_{amb}} = \frac{U_\infty c}{\mu_{amb}}$$

Equation D.14

$$\frac{\partial \Re e}{\partial \mu_{amb}} = \frac{-\rho_{amb} U_\infty c}{\mu^2{}_{amb}}$$

Equation D.15

$$\frac{\partial \Re e}{\partial c} = \frac{\rho_{amb} U_\infty}{\mu_{amb}}$$

Equation D.16

C.2. The Uncertainty in Pressure Measurement

Since the Cp results were obtained using measurements of the pressure difference (Ps,i – Pts) and the calculated dynamic pressure (Eq. 19), the uncertainty in the Cp could be estimated using,

$$U_{C_p} = \sqrt{\left(\frac{\partial C_p}{\partial\left(P_{s,i} - P_{ts}\right)} U_{(P_{s,i}-P_{ts})}\right)^2 + \left(\frac{\partial C_p}{\partial q_\infty} U_{q_\infty}\right)^2}$$

Equation D.17

$$\frac{\partial C_p}{\partial\left(P_{s,i} - P_{ts}\right)} = \frac{1}{q_\infty}$$

Equation D.18

$$\frac{\partial C_p}{\partial q_\infty} = -\frac{P_{s,i} - P_{ts}}{{q_\infty}^2}$$

Equation D.19

The drag coefficient of the airfoil was determined using the wake survey system. Therefore, the uncertainties associated with the pressure transducer specification, that was used to acquire the wake data, were examined. The pressure transducer uncertainty was provided by the manufacturer to be 0.10% of the full-scale range for the ±0.35 psid module. Using the uncertainties of these system measurements, the uncertainties of the wake survey results could be evaluated.

By combining Eq. 2.29 and Eq. 2.30, the expanded form of the drag coefficient expression becomes,

$$C_D = \frac{1}{q_\infty c} \sum_{i=1}^{n_{rake}-1} \left[\begin{array}{c} \sqrt{q^2{}_\infty - q_\infty\left(P_{0,\infty} - P_{0,w_i}\right)} + \sqrt{q^2{}_\infty - q_\infty\left(P_{0,\infty} - P_{0,w_{i+1}}\right)} \\ -2q_\infty + 2P_{0,\infty} - P_{0,w_i} - P_{0,w_{i+1}} \end{array} \right] (y_i - y_{i+1})$$

Equation D.20

Both $P0,_\infty$ and $P_{0,w}$ were referenced to atmospheric pressure. Therefore, the only contribution to the uncertainty in the drag coefficient was due to uncertainty in the measurements of the dynamic pressure, the airfoil chord, wake pressures and the free stream total pressure. Thus, the uncertainty in the drag coefficient can be expressed using,

$$U_{C_D} = \sqrt{\left(\frac{\partial C_D}{\partial q_\infty} U_{q_\infty}\right)^2 + \left(\frac{\partial C_D}{\partial c} U_c\right)^2 + \left(\frac{\partial C_D}{\partial P_{0,\infty}} U_{P_{0,\infty}}\right)^2 + \sum_{i=1}^{n_{rake}-1} \left(\frac{\partial C_D}{\partial P_{0,w}} U_{P_{0,w}}\right)^2}$$

Equation D.21

With

$$\frac{\partial C_D}{\partial q_\infty} = \frac{1}{q^2{}_\infty} \sum_{i=1}^{n_{rake}-1} \left[\begin{array}{c} \sqrt{q^2{}_\infty - q_\infty\left(P_{0,\infty} - P_{0,wi}\right)} + \sqrt{q^2{}_\infty - q_\infty\left(P_{0,\infty} - P_{0,wi+1}\right)} \\ -2q_\infty + 2P_{0.w} - P_{0,w_i} - P_{0,w_{i+1}} \end{array}\right] (y_i - y_{i+1}) + \frac{1}{q_\infty c} \sum_{i=1}^{n_{rake}-1} \left[\frac{2q_\infty - \left(P_{0,\infty} - P_{0,wi}\right)}{2\sqrt{q^2{}_\infty - q_\infty\left(P_{0,\infty} - P_{0,wi}\right)}} + \frac{2q_\infty - \left(P_{0,\infty} - P_{0,wi+1}\right)}{2\sqrt{q^2{}_\infty - q_\infty\left(P_{0,\infty} - P_{0,wi+1}\right)}} - 2\right] (y_i - y_{i+1})$$

Equation D.22

$$\frac{\partial C_D}{\partial c} = \frac{1}{q_\infty c^2} \sum_{i=1}^{n_{rake}-1} \left[\begin{array}{c} \sqrt{q^2{}_\infty - q_\infty\left(P_{0,\infty} - P_{0,wi}\right)} + \sqrt{q^2{}_\infty - q_\infty\left(P_{0,\infty} - P_{0,wi+1}\right)} \\ -2q_\infty + 2P_{0.w} - P_{0,w_i} - P_{0,w_{i+1}} \end{array}\right] (y_i - y_{i+1})$$

Equation D.23

$$\frac{\partial C_D}{\partial P_{0,\infty}} = \frac{1}{q_\infty c} \sum_{i=1}^{n_{rake}-1} \left(\begin{array}{c} 2 - \frac{q_\infty}{2\sqrt{q^2{}_\infty - q_\infty\left(P_{0,\infty} - P_{0,wi}\right)}} \\ \frac{-q_\infty}{2\sqrt{q^2{}_\infty - q_\infty\left(P_{0,\infty} - P_{0,wi+1}\right)}} \end{array}\right) (y_i - y_{i+1})$$

Equation D.24

$$\frac{\partial C_D}{\partial P_{0,wi}} = \frac{1}{q_\infty c}\left(\frac{q_\infty}{2\sqrt{q^2{}_\infty - q_\infty\left(P_{0,\infty} - P_{0,wi}\right)}} = 1\right)(y_i - y_{i+1})$$

Equation D.25

C.3. The Uncertainty in Aerodynamic Load

The aerodynamic coefficient of the 3D and also 2D wing was determined using force and moment measurement. Therefore, the uncertainties associated with the external balance specification that was used to measure the loads, were examined. The external balance uncertainty was provided by accomplish some load check for each x and y loading direction. Using the uncertainties of these system measurements, the uncertainties of the external balance results could be evaluated.

From equation 41 applied to force measurement using 6 components external balance the expression for C_D and C_L from equation 16 and 17 become

$$U_{C_L} = \sqrt{\left(\frac{\partial C_L}{\partial F_x} U_{F_x}\right)^2 + \left(\frac{\partial C_L}{\partial F_y} U_{F_y}\right)^2 + \left(\frac{\partial C_L}{\partial \alpha} U\alpha\right)^2 + \left(\frac{\partial C_L}{\partial q_\infty}\right)^2 + \left(\frac{\partial C_L}{\partial S}\right)^2}$$

Equation D.26

With

$$\frac{\partial C_L}{\partial F_x} U_{F_x} = \frac{1}{q_\infty S}\left(F_y cos\alpha - F_x sin\alpha\right)$$

$$\frac{\partial C_L}{\partial F_y} U_{F_y} = \frac{1}{q_\infty S}\left(F_y cos\alpha - F_x sin\alpha\right)$$

$$\frac{\partial C_L}{\partial \alpha} U\alpha = \frac{1}{q_\infty S}\left(F_y cos\alpha - F_x sin\alpha\right)$$

$$\frac{\partial C_L}{\partial q_\infty} = \frac{1}{q_\infty{}^2 S}\left(F_y cos\alpha - F_x sin\alpha\right)$$

$$\frac{\partial C_L}{\partial S} = \frac{1}{q_\infty S^2}\left(F_y cos\alpha - F_x sin\alpha\right)$$

Appendix D. Measurement Result from 2D Model With and Without Riblets

	U_{mean}	Width of Wake	I	V	DR
Riblet shaft	34.439	0.45	0.252	40.082	+19.70 %
Middle Line	19.067	0.65	0.684	40.082	- 9.12 %
Gap Line	18.040	0.60	0.646	40.082	- 7.13 %